

Department of Earth, Ocean and Ecological Sciences  
School of Environmental Sciences  
University of Liverpool



# **Investigating the postseismic deformation of strike-slip earthquakes on the Tibetan Plateau**

Thesis submitted in accordance with the requirements of the  
University of Liverpool for the degree of Doctor in Philosophy

By

Minxuan Feng

September 2018



# Abstract

InSAR is a useful technique to detect large-scale surface deformation from space. To place constraints on the rheological structure of the lithosphere in the Tibetan Plateau, two strike-slip earthquakes have been investigated. One is the Mw 7.6 Manyi earthquake, which occurred in the north-central Tibetan Plateau. The other is the Mw 6.5 Jiuzhaigou earthquake, which happened that on the eastern part of the Tibetan Plateau.

My InSAR data cover 12 years following the Manyi earthquake, much longer than previous researchers' dataset. I test three viscoelastic models (Maxwell, Standard linear solids, and Burgers body) and one afterslip model. The viscoelastic models cannot match the observed temporal-spatial deformation patterns. The distributions of deformation in the viscoelastic models extend into the far field and the residuals tend to increase, which are inconsistent with the data. The afterslip model has the lowest misfit and explains the temporal and spatial pattern of the observed deformation with decent result. A combined model that considers the effects of both afterslip and viscoelastic relaxation has also been tested. In this combined model, the viscoelastic relaxation that occurs with an elastic layer of thickness of 30 km over a half-space place, produce an estimate for viscosity of  $5 \times 10^{19}$  Pa s for this area. Therefore, either the afterslip model or the combined model can be used to explain the 12 years postseismic deformation of Manyi earthquake. The long time series of the Manyi earthquake enable us to distinguish between afterslip and viscoelastic relaxation.

The seismogenic fault of the Jiuzhaigou earthquake was previously unidentified and no surface rupture is found after the earthquake. I first determined the fault geometry and calculated coseismic slip model. The slip model indicates a left-lateral strike-slip pattern, which is consistent with focal mechanisms were determined by different agencies. There is no visible postseismic deformation signal of the fault, which means the surface deformation generated by fault creeping is smaller than the noise of our observation method over that period. Therefore, I try to find the lower bound of the viscosity for this area. My preferred minimum possible viscosity of the underlying half-space is  $\sim 6 \times 10^{17}$  Pa s.

Together with previous geodetic studies, the viscosities obtained from central Tibet show at least one order of magnitude difference with the viscosities obtained from the eastern Tibet. The heterogeneity indicates the rheology has a relatively large spatial change through the whole Plateau. The viscoelastic model always been proposed to explain long-term postseismic deformation and afterslip is used to explain the short-term deformation or localised deformation. Sometimes, the viscoelastic deformation signal is invisible in the moderate earthquakes as the stress is not large enough to generate observable deformation.



# Declaration

I, Minxuan, declare that the content presented in this thesis is all my own work. The thesis has not been submitted for any other degree or qualification.

Chapter 5 contains material from the publication:

Feng, M., Bie, L. & Rietbrock, A., 2018. Probing the rheology of continental faults: decade of post-seismic InSAR time-series following the 1997 Manyi (Tibet) earthquake, *Geophys. J. Int.*, 215, 600-613.

In this paper, Minxuan processed satellite data, conducted modelling, participated in discussion and prepared the paper, whilst all co-authors listed in this publication reviewed the manuscript and contributed to data interpretation.



# Acknowledgement

Both the China Scholarship Council (CSC) and the University of Liverpool fund my PhD study. I thank them for giving me the opportunity to study abroad. Besides them, there are so many people behind me to make the thesis possible.

Foremost, I would like to express my gratitude to my supervisors, Prof. Andreas Rietbrock and Dr Isabelle Ryder for their patience, motivation, knowledge, support and encouragement in my PhD study. Isabelle was my primary supervisor, and she guided me into the geodesy research field. I thank Andreas to overtake my supervision after Isabelle quit her job. Without their supervision, I could not overcome difficulties in my research and thesis writing.

Besides my supervisors, I am grateful to Lidong for his support in my research, particularly in the modelling and data analysis for the case study. He performs like another supervisor for me. Without his help, it will be difficult for me to publish the first paper before I graduate.

I will also thank PhD students and postdocs in the seismology and geodesy group, for helping me and encouraging me when I was at bottom of my PhD. Steve, Amaya, Lidong (again), Xiao, Sergio, James, Stephen, Isabella, Yu, you are the valuable friends to me. I will always remember the happy hours (e.g. afterschool BBQ, relax lunch) we have together. I must also thank my flatmate, Zitong Gong, and friend, Xiaoying Zhang for cheering me up and sharing happiness with me when I feel very depressed. I appreciate the great support and encouragement from my boyfriend and my parents during my studies at the University of Liverpool.





# Table of Contents

|   |             |
|---|-------------|
| <b>Abstract</b> .....   | <b>III</b>  |
| <b>Declaration</b> .....  | <b>V</b>    |
| <b>Acknowledgement</b> .....  | <b>VII</b>  |
| <b>Table of Contents</b> .....  | <b>IX</b>   |
| <b>List of Figures</b> .....  | <b>XIII</b> |
| <b>List of Tables</b> .....   | <b>XVII</b> |
| <b>Chapter 1</b> .....  | <b>1</b>    |
| <b>Introduction</b> .....   | <b>1</b>    |
| <b>1.1 Motivation</b> .....   | <b>1</b>    |
| <b>1.2 Rheology</b> .....   | <b>2</b>    |
| <b>1.3 Earthquake cycle</b> .....   | <b>4</b>    |
| 1.3.1 Previous studies of the earthquake cycle .....                            | 5           |
| 1.3.2 Possible mechanisms of postseismic deformation .....                      | 6           |
| 1.3.3 Time scale .....  | 8           |
| <b>1.4 Geodetic observations</b> .....  | <b>9</b>    |
| <b>1.5 Overview of thesis</b> .....   | <b>10</b>   |
| <b>Chapter 2</b> .....  | <b>13</b>   |
| <b>Geological background</b> .....  | <b>13</b>   |
| <b>2.1 Tectonic background</b> .....  | <b>13</b>   |
| <b>2.2 Rheological structure of the lithosphere</b> .....                       | <b>15</b>   |
| <b>2.3 Strike-slip fault and earthquakes</b> .....                              | <b>18</b>   |
| 2.3.1 Strike-slip fault in Tibet .....  | 19          |
| <b>2.4 Lessons from previous studies of these two earthquakes</b> .....         | <b>20</b>   |
| <b>Chapter 3</b> .....  | <b>23</b>   |
| <b>InSAR Data and Error mitigation</b> .....                                    | <b>23</b>   |
| <b>3.1 Overview of InSAR</b> .....  | <b>23</b>   |
| <b>3.2 Data processing packages</b> .....                                       | <b>25</b>   |
| <b>3.3 Error mitigation</b> .....   | <b>26</b>   |
| 3.3.1 Residual orbital error.....   | 26          |
| 3.3.2 Atmospheric error.....  | 27          |
| <b>3.4 Case study of each atmospheric method</b> .....                          | <b>29</b>   |
| 3.4.1 MERIS.....  | 29          |
| 3.4.2 ERA-Interim .....   | 31          |
| 3.4.3 An empirical relationship between interferometric phases and elevations.. | 33          |
| <b>Chapter 4</b> .....  | <b>35</b>   |
| <b>Geodetic Modelling</b> .....   | <b>35</b>   |

|  |            |
|--|------------|
| <b>4.1 Viscoelastic modelling</b> .....  | <b>35</b>  |
| 4.1.1 Viscoelastic computations .....  | 37         |
| 4.1.2 Use of the viscoelastic code in this thesis.....   | 40         |
| 4.1.3 Synthetic test of the viscoelastic models .....  | 42         |
| <b>4.2 Elastic modelling</b> .....   | <b>46</b>  |
| 4.2.1 Elastic computations.....  | 46         |
| 4.3 Distributed slip on the fault.....   | 49         |
| 4.3.1 Nonlinear process: determination of fault geometry.....  | 49         |
| 4.3.2 Linear process: invert for slip distribution.....  | 50         |
| <b>Chapter 5</b> .....   | <b>55</b>  |
| <b>Probing the rheology of continental faults: Decade of postseismic InSAR<br/>time series following the 1997 Manyi (Tibet) earthquake</b> ..... | <b>55</b>  |
| <b>Abstract</b> .....  | <b>55</b>  |
| <b>5.1. Introduction</b> .....   | <b>56</b>  |
| <b>5. 2. Data Processing and time series</b> .....   | <b>59</b>  |
| <b>5. 3. Modelling</b> .....   | <b>62</b>  |
| 5.3.1 Viscoelastic modelling.....  | 63         |
| 5.3.2 Afterslip modelling.....   | 66         |
| <b>5.4. Discussion</b> .....   | <b>68</b>  |
| 5.4.1 Limitations of viscoelastic modelling.....   | 68         |
| 5.4.2 Applicability of afterslip modelling.....  | 72         |
| 5.4.3 Combined afterslip and viscoelastic modelling .....  | 73         |
| 5.4.4 Rate of late postseismic deformation.....  | 75         |
| <b>5.5. Conclusion</b> .....   | <b>76</b>  |
| <b>Data</b> .....  | <b>77</b>  |
| <b>Appendix A: Time series construction</b> .....  | <b>77</b>  |
| <b>Appendix B. Model set-up</b> .....  | <b>79</b>  |
| <b>Acknowledgement</b> .....   | <b>82</b>  |
| <b>Chapter 6</b> .....   | <b>83</b>  |
| <b>Coseismic and postseismic activity associated with the 2017 Jiuzhaigou<br/>Earthquake</b> .....   | <b>83</b>  |
| <b>6.1 Introduction</b> .....  | <b>83</b>  |
| <b>6.2 Data processing</b> .....   | <b>86</b>  |
| 6.2.1 Interferograms .....   | 86         |
| 6.2.2 Correction of atmospheric and orbital error .....  | 87         |
| <b>6.3 Aftershocks</b> .....   | <b>90</b>  |
| <b>6.4 Coseismic slip inversion</b> .....  | <b>91</b>  |
| <b>6.5 Postseismic deformation</b> .....   | <b>97</b>  |
| 6.5.1 Time-series .....  | 97         |
| 6.5.2 Modelling .....  | 98         |
| <b>6.7 Discussion and Conclusions</b> .....  | <b>101</b> |
| <b>Chapter 7</b> .....   | <b>105</b> |

|   |            |
|---|------------|
| <b>Discussion .....</b>   | <b>105</b> |
| <b>7.1 Rheology estimates from various studies and their spatial-temporal characteristics .....</b> | <b>105</b> |
| 7.1.1 Summary of the various studies .....  | 105        |
| 7.1.2 spatial-temporal characteristics of the viscosities .....                                     | 111        |
| <b>7.2 Choosing mechanism(s) for postseismic deformation of strike-slip earthquakes .....</b>       | <b>112</b> |
| <b>Chapter 8 .....</b>  | <b>117</b> |
| <b>Conclusion and outlook .....</b>   | <b>117</b> |
| 8.1 Manyi earthquake .....  | 117        |
| 8.2 Jiuzhaigou earthquake .....   | 118        |
| 8.3 Outlook .....   | 119        |
| <b>Supplementary.....</b>   | <b>121</b> |
| <b>Tables and figure in Chapter 4: .....</b>  | <b>121</b> |
| <b>Figures in Chapter 5: .....</b>  | <b>123</b> |
| <b>Figures in Chapter 6: .....</b>  | <b>127</b> |
| <b>Bibliography .....</b>   | <b>129</b> |



# List of Figures

|  |    |
|--|----|
| Figure 1.1 Mechanical analogues for different rheologies.....  | 8  |
| Figure 2.1 Topographic map of the Tibetan Plateau and surrounding region with Quaternary-active faults and geological sutures from the compilation of Taylor and Yin (2009) .. | 14 |
| Figure 2.2 Distribution of focal mechanisms ( $M_w > 6$ ) across the Tibetan Plateau since 1976 from the GCMT catalogue.....   | 15 |
| Figure 2.3 Global distribution of $M_w > 6$ (1976-2017) all earthquakes from the Global Centroid Moment Tensor (GCMT) catalogue..  | 18 |
| Figure 2.4 Frequency-Depth plots for strike-slip faulting events in the world.....   | 19 |
| Figure 3.1 The wet and hydrostatic delay predicted by ERA-Interim model from 20031007 to 20041130.....   | 32 |
| Figure 3.2 Two interferograms with the same date in the different format (20031007 to 20041130)..  | 34 |
| Figure 4.1 Mechanical analogues for different viscoelastic model, consisting of different combinations of spring and dashpot.....  | 37 |
| Figure 4.2 The sketch structure of the fault used in the software testing.....   | 39 |
| Figure 4.3 Comparison of surface deformation from RELAX, PSGRN/PSCMP and VISCO1D.....  | 39 |
| Figure 4.4 Comparison of surface displacements in east and north directions along a profile perpendicular to the fault and passing through its centre. ....                    | 40 |
| Figure 4.5 Comparison of outputs from the different case of VISCO1D at one Maxwell time after a strike-slip event.....   | 41 |
| Figure 4.6 Surface vertical displacements from viscoelastic-gravitational relaxation or non-gravitational relaxation following a strike-slip event.....                        | 42 |
| Figure 4.7 Surface deformations predict by different elastic layer. $h$ means the thickness of the elastic layer..   | 43 |
| Figure 4.8 north-surface displacement predict by the viscoelastic models.....  | 45 |
| Figure 4.9 North-velocity at the surface from viscoelastic relaxation following a strike-slip event, normalized to the uniform coseismic slip on the fault. ....               | 46 |
| Figure 4.10 Surface deformation outputs were calculated using Okada's method and Wang et al.'s method, respectively. ....  | 49 |
| Figure 4.11 (a). The original input fault geometry to generate synthetic surface displacement. (b) Modelled slip distribution on the fault plane.....                          | 52 |

|  |    |
|--|----|
| Figure 4.12 The comparison between modelled LOS displacements and the synthetic LOS displacement .....   | 52 |
| Figure 4.13 Plot of the trade-off curve between slip roughness and data misfit in the synthetic test.....  | 53 |
| Figure 5.1 Tectonic map (top right) and location map (left).....   | 58 |
| Figure 5.2 (a). An example demonstrating mitigation of atmospheric noise. Panels from left to right show an original interferogram of the Manyi earthquake (19971202-19980804), estimated error, and corrected interferogram. .... | 61 |
| Figure 5.3 Post-seismic time-series and corresponding best fitting modelling results.  | 62 |
| Figure 5.4 Postseismic slip distributions from afterslip inversions. ....  | 67 |
| Figure 5.5 Mean displacements against time after the Manyi earthquake. ....  | 69 |
| Figure 5.6 Evolution of the mean displacements of patches A, B, C and D, after the Manyi earthquake.....   | 70 |
| Figure 5.7 Swath profile across the fault for each model from early to late time.....  | 71 |
| Figure 5.8 (a) Misfit as a function of viscosity. (b) Best fitting viscosity for each time interval deformation. ....  | 71 |
| Figure 5.9 The sketch map of combined mechanism model.....   | 74 |
| Figure 5.10 Profile across the InSAR LOS rate map. ....  | 76 |
| Figure A5.1 Roughness plotted against misfit for different smoothing factors in the time-series matrix.....  | 79 |
| Figure A5.2 Mean displacements predicted by different viscoelastic models with various rheological model parameters.....   | 80 |
| Figure 6.1 a. Sketch map of the Tibet Plateau. b. the tectonic setting of the Jiuzhaigou earthquake area.....  | 86 |
| Figure 6.2 Baseline versus time plots for the ascending track 128. ....  | 87 |
| Figure 6.3 Comparison between the two correction methods.....  | 89 |
| Figure 6.4 Comparison between different correction methods.....  | 90 |
| Figure 6.5 Reduction of standard deviation after correction of the interferograms. The percentage is equal (original data – corrected data)/original data.....   | 90 |
| Figure 6.6 Number of aftershocks as a function of time after the Jiuzhaigou earthquake. ....   | 91 |
| Figure 6.7 InSAR data of track 62 and corresponding elastic model. ....  | 93 |
| Figure 6.8 InSAR data of track 128 and corresponding elastic model. Left panels: wrapped and unwrapped coseismic interferogram of ascending track 128.. ....   | 93 |
| Figure 6.9 Fault parameter uncertainties distribution of the uniform slip InSAR model.....   | 94 |

|  |     |
|--|-----|
| Figure 6.10 Aftershocks of the Jiuzhaigou earthquake.....  | 94  |
| Figure 6.11 Trade-off curve between the misfit and model roughness. ....   | 95  |
| Figure 6.12 Slip distributions on the fault plane.....   | 96  |
| Figure 6.13 Uncertainty with the slip distributions.....   | 96  |
| Figure 6.14 Coseismic interferograms inverted from the coseismic slip and modelled surface displacement of the Jiuzhaigou earthquake (the positive range change indicating motions away from the satellite)..... | 97  |
| Figure 6.15 Postseismic deformation time-series.....   | 98  |
| Figure 6.16 An example of one forward viscoelastic calculation.....  | 100 |
| Figure 6.17 The signal-to-noise ratio of forwarding calculations with variable elastic layer thickness (h) and viscosity ( $\eta$ ). ....  | 101 |
| Figure 6.18 Simplified tectonic sketch map around the Jiuzhaigou earthquake area.....  | 102 |
| Figure 7.1 Location map of previous studies.....   | 106 |
| Figure 7.2 The circles with number represent the viscosities beneath the Tibet Plateau inferred by using postseismic geodetic data covering different time periods and for different earthquakes.....            | 112 |
| Figure S5.1 Residuals for each model from early to late time period (calculated as the model minus data).....  | 123 |
| Figure S5.2 Range change predicted by non-linear model at 11 <sup>th</sup> year after the earthquake.....  | 124 |
| Figure S5.3 The three patches afterslip model inversion results.....   | 124 |
| Figure S5.4 Trade off curve between residual viscosity of viscoelastic model and misfit of the combined model. ....  | 125 |
| Figure S6.1 Down-sampled interferogram data of the earthquake area using the quadtree decomposition algorithm.....   | 127 |
| Figure S6.2 Recovered surface deformation by adjacent smoothing factor value...  | 127 |
| Figure S6.3 Normalised roughens plotted against misfit for different smoothing factors.....  | 127 |
| Figure S6.4 Mean displacement with time for different smoothing factor.....  | 128 |
| Figure S6.5 The coherence figure of the Jiuzhaigou coseismic interferograms.....   | 128 |





# List of Tables

|   |     |
|---|-----|
| Table 1.1 Basic information of major SAR missions .....   | 10  |
| Table 1.2 Current studies for the Manyi earthquake.....   | 21  |
| Table 3.1 MERIS coverage in percentage.....   | 30  |
| Table 4.1 Material parameters of the earth models used in this section .....                          | 44  |
| Table 5.1. Details of Data Used in InSAR Time Series Analysis.....                                    | 59  |
| Table 5.2 Best-fitting viscosities and misfits for each model .....                                   | 65  |
| Table 6.1 Focal mechanism from different institutions .....   | 83  |
| Table 6.2 Details of the Data used in the following analysis.....                                     | 86  |
| Table 6.3 Fault parameter intervals and best-fit solution resulting from the nonlinear inversion..... | 92  |
| Table 6.4 Structure model for Jiuzhaigou earthquake .....   | 99  |
| Table 7.1 Rheology estimates from various studies.....  | 109 |
| Table 7.2 Mechanisms of postseismic deformation for larger strike-slip earthquakes                    | 113 |
| Table S4.1 The synthetic crust structure information used in the section 4.1.3. ....                  | 121 |
| Table S4.2 The crust structure information used in the layered elastic model. ....                    | 121 |



# Chapter 1

## Introduction

### 1.1 Motivation

How the continents deform is important because it will change the topography and impact climate and environment around the world. It has been the subject of a longstanding scientific debate, as a consistent conclusion has not yet been reached. In an active tectonic area, the kinematics and dynamics of continental deformation can help us to gain a clear idea about the driving force of the deformation of the upper crust and earthquake hazard assessments as well as the rheology. Two end-member approaches have been proposed to explain the kinematic behaviour of lithospheric deformation. One emphasises the discontinuous deformation between rigid plates that are bounded by lithospheric scale faults (e.g. McClusky *et al.*, 2000, Tapponnier *et al.*, 1982, Tapponnier *et al.*, 2001), known as the microplate model. In this model, the differential motions between discrete plates are derived from the high slip rate on a series of major boundary faults. (e.g. Avouac and Tapponnier, 1993, Replumaz and Tapponnier, 2003). The other model is the continuum model which regards continental deformation as a widely distributed phenomenon due to the viscous flow occurring in weak, ductile material at some depth within the lithosphere (England and Molnar, 1997, England and Mckenzie, 1982). In this theory, discrete slip in the brittle upper crust occurs on many faults with roughly comparable slip rates (e.g. Flesch *et al.*, 2001, Gan *et al.*, 2007). However, which approach better explains the reality remains a controversial issue. The insufficient understanding about the kinematics and dynamics of deformation limit the conception of the earthquake cycle as it explains the characteristics of observed deformation across faults.

To solve the dynamic debate, it is important to improve the knowledge of the rheological structure of the lithosphere. Efforts from a wide range of disciplines, e.g. seismology and geodesy, are continuously being made to improve the understanding of rheological properties and the structure of the lithosphere. However, as the tectonic settings vary from region to region, the lithosphere is inevitably complicated. Moreover, different researchers have different interpretations of the data even for the same region. For example, observations of postseismic displacement after an earthquake may be explained by both localised shear and viscous flow. The rheological structure of the lithosphere will affect forward calculations of stress evolution, which are important for earthquake hazard assessment (e.g. earthquake forecasting, stress triggering between earthquakes). Thus improvements in the understanding of the material rheology can help us better to characterise the earthquake cycle and associated deformation across active faults.

This thesis aims to place constraints on the rheological structure of the lithosphere using Interferometric Synthetic Aperture Radar (InSAR) satellite imaging. I will run computer simulations of elastic and viscoelastic processes to understand observations of surface deformation and constrain lithospheric rheology. Different postseismic mechanisms will be explored to explain temporal and spatial characteristics of aseismic deformation following strike-slip earthquakes. I will consider both, short-term and long-term observations covering a time span from a few months to decades after individual major earthquakes.

## **1.2 Rheology**

Rheology governs the deformation of rocks in response to forces in the Earth's interior (e.g. Bürgmann and Dresen, 2008). Improved understanding of the rheology of the Earth's lithosphere and faults is fundamental to studies of earthquake cycle and fault interaction.

Based on the study of fault systems around the world, a range of frictional properties is employed. For example, an earthquake is the result of velocity weakening behaviour, stable sliding or creep is due to velocity strengthening behaviour (e.g. Scholz, 1998, Simpson *et al.*, 2001). Based on laboratory rock mechanics experiments, several mathematical formulations of the rate and state variable friction laws are proposed (e.g. Byerlee, 1978, Dieterich, 1978), which can explain what happens during the earthquake cycle. The most commonly used friction law is expressed as (Scholz, 1998):

$$\tau = \left[ \mu_0 + a \ln \frac{v}{v_0} + b \ln \frac{v_0 \theta}{L} \right] \bar{\sigma} \quad (1.1)$$

where  $\tau$  is shear stress,  $\mu_0$  is the steady-state friction at reference slip rate ( $v_0$ ),  $v$  is slip velocity,  $\theta$  is the state variable that evolves with time,  $\bar{\sigma}$  is effective normal stress (equal to normal stress minus pore pressure).  $a$  and  $b$  are empirical constants which are derived from material properties of the frictional surface.  $L$  is the critical slip distance which is required for asperities to move past each other. If  $(a - b) < 0$ , the material tends to be unstable (velocity-weakening) and earthquakes can occur. If  $(a - b) > 0$ , the material tends to be stable (velocity-strengthening) and earthquakes do not occur. Therefore, earthquakes can be recognized resulting from stick-slip frictional instability (Brace and Byerlee, 1966). Rock mechanics experiments on granite (e.g. Blanpied *et al.*, 1991), the representative rock of the continental crust, suggest that  $(a - b)$  is negative at low temperatures and becomes positive for temperatures above 300 C. When the temperature increases with depth to a certain degree, atoms and dislocations in rocks become mobile, giving rise to creep and viscous flow.

The transition from shallow brittle to deep viscous behaviour is governed by rock rheology. The quantitative description of rheology requires constitutive equations that relate stress and strain rates (e.g. Bürgmann and Dresen, 2008). When the strain rate is proportional to stress rise to a power of  $n > 1$ , materials behaving in a non-Newtonian trend (e.g. power-law rheology) so that effective viscosity decreases when stress

increases. Materials whose rate of strain is linear proportional to the applied stress ( $n = 1$ ) have linear rheology, also known as a “Newtonian Fluid”. Laboratory experiments on rock mechanics suggest that the lower crust and upper mantle may creep in either a Newtonian rheology or non-Newtonian rheology.

Although the experimental evidence for nonlinear rheology can exist in the lower crust and upper mantle, the linear rheology is the most commonly utilized rheology as linear rheology is easier for mathematical calculation when solving geophysical problems. Linear models have explained numerous postseismic geodetic observations successfully (e.g. Biggs *et al.*, 2009, Ryder *et al.*, 2011). In this thesis, I mainly consider linear rheology, in which strain rate is linearly proportional to stress.

The viscosity of a fluid is a measurement of its ability to flow. High viscosity fluids deform more slowly than low viscosity fluids. Effective viscosity can be obtained by a scale ratio of stress to strain rate. In postseismic studies, viscosity can be inferred by matching temporal-spatial evolution of rheological model with geodetic observation. The increase of temperature with depth is probably one of the most important factors influencing crustal viscosity (e.g. Katagi *et al.*, 2008, Yamasaki and Houseman, 2012). Lateral variations of crustal viscosity in the in rheology are also plausible (e.g. Yamasaki *et al.*, 2014, Moore and Parsons, 2015). For example, the crustal viscosity could decrease with depth (an e-folding depth) for an assumed exponential dependence (Yamasaki and Houseman, 2012) from  $1.2 \times 10^{21}$  Pa s at 10 km depth to  $1.6 \times 10^{18}$  Pa s at the Moho (at 60 km).

### **1.3 Earthquake cycle**

Reid (1910) first proposed the earthquake cycle based on the elastic rebound theory to explain the displacement fields measured by triangulation surveys after the 1906 San Francisco earthquake. The kinematic behaviour of the San Andreas Fault before and after the 1906 San Francisco earthquake showed an opposite pattern. The elastic

rebound theory stated that earthquakes occurred as a result of an abrupt release of strain accumulated during the long interseismic period. In elastic rebound theory, the earthquake cycle is split into two distinct stages based on the kinematic behaviour of deformation observed. At the coseismic phase, stress exceeds the frictional resistance, resulting in an earthquake. At the interseismic phase, due to steady plate motion on either side of the fault, the strain is slowly building up.

However, in reality, the earthquake process is far more complicated than the description above because it does not account for preseismic and postseismic motion. Following coseismic rupture, transient deformation has been observed following several large earthquakes, which eventually decays back to the steady long-term loading rate. The postseismic deformation is due to a time-dependent relaxation of the stresses induced by coseismic rupture. The postseismic deformation may last from days to decades, depending on the relaxation mechanism(s). Preseismic phase describes the crustal deformation just prior to a large earthquake. However, the preseismic phase is elusive and inconsistent (Scholz, 2002). Given fragmentary observations and the anomalous nature of the preseismic phase, the discussion of the preseismic phase is beyond the scope of this thesis.

### **1.3.1 Previous studies of the earthquake cycle**

In order to determine a slip model that reveals earthquake rupture patterns, most studies of earthquake have focused on the coseismic phase. A rectangular fault plane is assumed to be buried in a homogeneous elastic half-space (e.g. Funning *et al.*, 2007). To better fit the geodetic observations, a multi-segment fault is more realistic, and/or a curved fault plane is adopted. For example, Reilinger *et al.* (2000) examined the coseismic deformation of the 1999 Izmit earthquake in Turkey by testing a slip model with five segments. The length and strike of the segments are determined based on InSAR and field mapping data.

The interseismic phase and early postseismic phases have also been widely studied. The interseismic slip rate of faults can be obtained from the long-term observation prior to the earthquake or later Quaternary activity. Although measuring the small deformation signal of interseismic deformation is difficult using InSAR, previous studies have shown that it is possible by using multiple interferograms (e.g. Wright *et al.*, 2001, Wright *et al.*, 2004).

In the postseismic phase, the crust and mantle are adapting to the deformation imposed by the earthquakes. The coseismic and the postseismic processes usually release a large portion of the strain accumulated during the interseismic interval. Sometimes postseismic deformation releases a comparable seismic moment or an even higher one than the main shock itself. For example, the geodetic moment produced by postseismic deformation was three times larger than the coseismic moment in the 2004  $M_w$ 6 Parkfield earthquake (Freed, 2007). Therefore, postseismic relaxation has been recognised as a very important component of the seismic cycle. Several mechanisms can be used to explain the postseismic deformation of one earthquake independently or in combination. Which mechanism is significantly involved in the observed postseismic deformation is still an open question. The temporal and spatial deformation changes provide essential information to test possible mechanisms. A detailed introduction of the possible mechanisms of the postseismic phase can be found in the next section.

### **1.3.2 Possible mechanisms of postseismic deformation**

Postseismic deformation is the crustal response to the redistribution of stresses caused by an earthquake. Postseismic surface motion was first noticed after the 1966  $M_w$  6.4 Parkfield earthquake (Smith and Wyss, 1968) and has also been documented following other large earthquakes, e.g. the 1992  $M_w$  7.3 Landers earthquake in southern California (Pollitz *et al.*, 2000, Shen *et al.*, 1994), the 2004  $M_w$  6.4 Parkfield earthquake (Barbot *et al.*, 2009).



Poroelastic rebound, afterslip on coseismic fault planes and viscoelastic relaxation are widely used to explain postseismic deformation (e.g. Freed, 2007, Peltzer *et al.*, 1998, Pollitz *et al.*, 2000). These mechanisms differ in both temporal and spatial scale. However, due to the complexity of physical processes and the limitations of geodetic observations, it can be challenging to isolate the contribution of the various mechanisms unequivocally (e.g. Ryder *et al.*, 2014). For an individual case, different mechanisms are often capable of producing the same observed surface displacements independently or in combination. For example, the postseismic deformation of the 1992 Landers earthquake have been interpreted in terms of a number of relaxation mechanisms, including fault afterslip (Shen *et al.*, 1994), poroelastic effects (Peltzer *et al.*, 1998), viscoelastic relaxation in the lower crust (Deng *et al.*, 1998) and upper mantle (Pollitz *et al.*, 2000), or a combination of poroelastic rebound and viscoelastic relaxation (Masterlark and Wang, 2002) etc.

The poroelastic rebound model has been applied to study crustal deformation associated with earthquakes such as the 1992 Lander strike-slip earthquake (Peltzer *et al.*, 1998) or the 2004 Sumatra subduction zone earthquake (Hughes *et al.*, 2010). In general, poroelastic rebound produces a small-wavelength signal within only a few kilometres of the coseismic rupture (Peltzer *et al.*, 1996, Peltzer *et al.*, 1998), and over a short time period (Freed *et al.*, 2006). Since the studies presented in this thesis cover a much larger area and more extended periods after the earthquakes, poroelastic rebound is unlikely to be a dominant effect.

Afterslip, where coseismic stress changes drive aseismic slip, (e.g. Marone *et al.*, 1991) produces transient ground movement following an earthquake. Afterslip often continues subsequent to the earthquake for a period of a year or more. Several authors have inferred afterslip as the dominant mechanism in their postseismic studies (e.g. Bürgmann *et al.*, 2002, Freed, 2007). Afterslip is expected either at the down-dip extension of the coseismic rupture (Tse and Rice, 1986) or shallow depth within

unconsolidated sedimentary cover (Marone *et al.*, 1991). The temporal evolution of afterslip can fit logarithmic function (e.g. Ryder *et al.*, 2007).

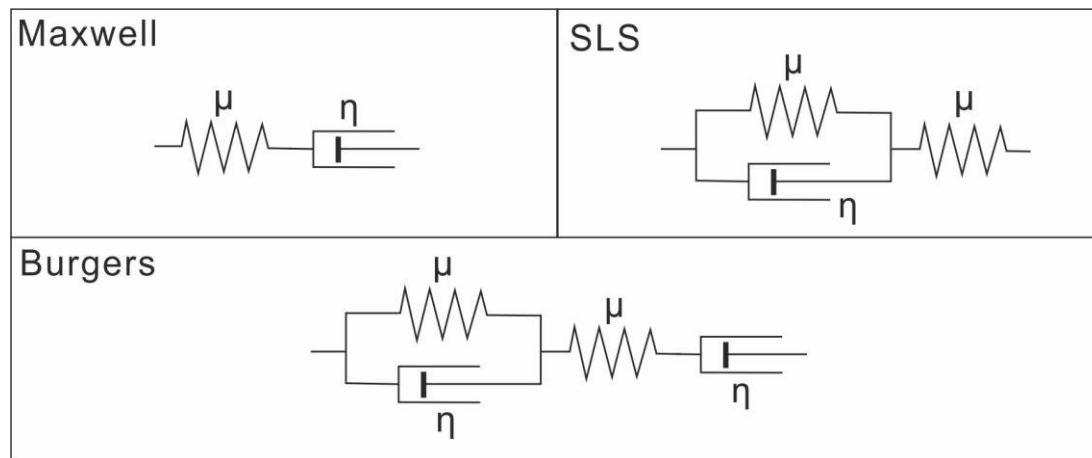


Figure 1.1 Mechanical analogues for different rheologies, consisting of different combinations of spring (elastic element) and dashpot (viscous element).  $\mu$  and  $\eta$  represent the shear modulus and viscosity of the elastic and viscous elements, respectively.

Viscoelastic relaxation arises from the inability of the weaker lower crust and/or upper mantle to sustain coseismic stress changes (Freed *et al.*, 2006). Therefore, the viscoelastic behaviour depends on the rheology of the research area. Different viscoelastic properties can be represented by various combinations of linear elastic and linear viscous elements (Figure 1.1). The Maxwell and Burgers body are the two viscoelastic relationships most commonly utilized to represent the lower crust and/or upper mantle underlying the elastic upper crustal lid (e.g. Pollitz *et al.*, 2000, Ryder *et al.*, 2014). Each model has a different strain–stress change relationship with various temporal decay rates. One can test different rheological models and find the best fitting model to describe the temporal and spatial evolution of the geodetic observations of postseismic deformation (e.g. Ryder *et al.*, 2007).

### 1.3.3 Time scale

Various mechanisms are likely to be occurring during a postseismic phase (Wright *et al.*, 2013). Over short time scales (months to years), much of the postseismic deformations support the notion that afterslip is the primary mechanism. For example,

afterslip is the only mechanism that can explain the first two years of postseismic deformation after the 2004 Parkfield earthquake (Freed, 2007). Long-term (years to decades) observations, however, imply that viscoelastic relaxation of the lower crust and mantle are the most significant processes. Ryder *et al.* (2014) presented an example that Maxwell relaxation can explain the long-term observation of the late postseismic deformation of two major earthquakes in 1951 and 1952 in Tibet. However, Ingleby and Wright (2017) analysis of major continental earthquakes found that the afterslip model could reproduce the overall temporal decay very well. The afterslip model has not often been tested for the decadal timescale in previous studies. Recent GPS and InSAR data suggest that afterslip on the central segment of the 1999 Izmit fault rupture is still taking place. Since the earthquake, the afterslip has lasted for 18 years (Cakir *et al.*, 2017). Thus, as the earthquake happened decades ago, we could perform a long-term postseismic analysis and test the possibility of afterslip mechanisms.

## **1.4 Geodetic observations**

As described above, the postseismic surface motion has been observed geodetically in the years to decades following a number of major earthquakes by geodetic techniques, e.g. GPS and InSAR. GPS provides high precision vector displacements at a high temporal sampling frequency. The main weakness of GPS is its sparse spatial coverage and expensive operating costs. For example, there are a few GPS stations in the central and western Tibet, where there are areas of high seismic activity. So much of the motion of this area is unconstrained. InSAR data has sub-centimetre precision and high spatial sampling. It does not require fieldwork so it efficiently compensates for the spatial coverage limitation in GPS data. However, the spatial decorrelation and atmospheric effects will influence the accuracy of the InSAR measurement (e.g. Zebker *et al.*, 1997, Zebker and Villasenor, 1992), which need to be mitigated during data processing. In this thesis, I only use InSAR data due to the lack of GPS data in my research area.

Table 1.1 Basic information of major SAR missions

| SAR mission  | Operating period | Band | Revisit time (days) | Imaging mode |
|--------------|------------------|------|---------------------|--------------|
| ERS-1        | 1991-2000        | C    | 35                  | Stripmap     |
| ERS-2        | 1995-2011        | C    | 35                  | Stripmap     |
| ENVISAT      | 2002-2012        | C    | 35                  | Multiple     |
| Radarsat-1   | 1995-2003        | C    | 24                  | Multiple     |
| Radarsat-2   | 2007-            | C    | 24                  | Multiple     |
| Sentinel-1A  | 2014-            | C    | 12                  | Multiple     |
| Sentinel-1B  | 2016-            | C    | 12                  | Multiple     |
| JERS-1       | 1992-1998        | L    | 44                  | Stripmap     |
| ALOS         | 2006-2011        | L    | 46                  | Multiple     |
| COSMO-SkyMed | 2007-            | X    | 16                  | Multiple     |
| TerraSAR-X   | 2007-            | X    | 11                  | Multiple     |

Note: Summarized from <https://www.itc.nl/Pub/sensordb/AllSatellites.aspx>, Different band has different wavelength( $\lambda$ ). X-band:  $\lambda = 3.1$  cm; C-band:  $\lambda = 5.6$  cm; L-band:  $\lambda = 23.6$  cm. Constellation of two satellites (A & B units), 12 days repeat cycle (1 satellite), 6 days for the constellation

Major SAR missions are listed in Table 1.1. Those deployed by the European Space Agency (ESA) have generated a wealth of observations. The data are free of charge and available to the public to download. It provides a unique opportunity to study crustal deformation and active processes. A large amount of new SAR instruments and satellite constellations have been launched during last 20 years, which have accelerated improvements of processing algorithms and measurement accuracies. The latest mission has much shorter revisit time than the early missions. In this thesis, I use the ERS and Envisat satellite for the Manyi earthquake, and use Sentinel data for the Jiuzhaigou earthquake.

## 1.5 Overview of thesis

In this thesis, I investigate the postseismic deformation of two strike-slip fault earthquakes in Tibet. The following chapters of thesis are structured as follows:

Chapter 2: A concise introduction to the geological background of the Tibetan Plateau. The entire Tibetan Plateau was mainly influenced by the Indian–Eurasian collision, which reactivated and modified the sutures and fault zone within the

Tibetan Plateau. The rheology of the Tibetan Plateau has continued to be a topic of debate for decades as both end-member models can explain part of the observations. The two earthquakes, the Manyi earthquake and the Jiuzhaigou earthquake, that happened within the central flat Tibetan Plateau provide us with opportunities to give the constraint on the rheology of central Tibet where there is lack of research.

Chapter 3: An overview of the major observational technique, Interferometric Synthetic Aperture Radar (InSAR). The development of InSAR processing packages is introduced. The techniques used in this thesis to mitigate tropospheric delay and their main applications in various research areas are also outlined. I show the effects of each mitigation method with the Manyi earthquake InSAR data. Among MERIS, ERA and empirical linear relationship between the noise and altitude, I use the last method to correct the atmospheric noise of the Manyi postseismic data.

Chapter 4: This chapter gives an introduction to how elastic and viscoelastic modelling serves as a way to understand the rheological structure of the continental lithosphere. The elastic and viscoelastic theory relevant to modelling the geodetic observations is discussed. The codes used in the case study are introduced. Detailed tests and comparisons of these codes are also shown in this chapter.

Chapters 5: I focus on the 1997 Manyi earthquake, which occurred in central Tibet. Many researchers have studied this earthquake, but most of their studies are primarily based on the 4 year dataset that were compiled by Ryder *et al.* (2007). I processed ~12 year's postseismic interferograms after the earthquake. We construct nearly two hundred of interferograms with tropospheric noise corrected. Time series is analysis to map surface deformation. I test three viscoelastic models (the Maxwell, Standard linear solids and Burger body) and afterslip. The best model to explain this long term postseismic is the afterslip, which is selected by the temporal spatial pattern and misfit. A combined model that considers the effects from both viscoelastic relaxation

and afterslip is also considered. With the 30 km elastic layer overlaying the viscoelastic half-space, we estimate a viscosity of  $5 \times 10^{19}$  Pa s for this research area.

Chapter 6: In this chapter, I am concerned with the 2017 Jiuzhaigou earthquake in Tibet. This earthquake happened on an unrecorded blind fault with no obvious surface rupture. The epicentre is located in an area where three tectonic faults interact. I use InSAR observations of the coseismic deformation to define the fault geometry and coseismic slip model. The Huya fault is the most likely fault to have caused the earthquake according to the focal mechanisms of historical earthquakes and the fault geometry. Postseismic surface motion following the 2017 Jiuzhaigou earthquake in Tibet is used to investigate mechanisms of postseismic stress relaxation. Modelling of the time series constructed from the interferograms places constraints on the rheology of the thick crust in this region. Although there is no obvious postseismic signal during the observation time span, we can place a lower bound of the viscosity of  $6 \times 10^{17}$  Pa s from eight months postseismic deformation for the east margin of the Tibet.

Chapter 7: The rheology in these two earthquakes and other large earthquakes in the Tibetan Plateau that were investigated previously are compared. Estimations of lithospheric rheology for different parts of the Tibetan Plateau are compared, with the aim of examining spatial and temporal differences in rheology. The explanations of different postseismic deformations at different timescale are also discussed.

Chapter 8: This chapter summarises the results from the case studies in Chapters 5 and 6. The limitations in this thesis are also pointed out. Suggestions for future work following this thesis are given at the end.

# Chapter 2

## Geological background

The Tibetan Plateau is the world's highest and largest plateau, with an average elevation exceeding 4500 metres and an area of 2500000 square kilometres. It is created by the collision of India with Eurasia during the past ~40 million years (Molnar and Tapponnier, 1975, Yin and Harrison, 2000). Tibetan Plateau is a seismically active area that experiences a number of earthquakes every year. In the last 30 years, there have been more than three dozen earthquakes with a magnitude > 6 within the area (USGS catalogue). These earthquakes have caused devastating loss of life and destruction. For example, about 69000 people lost their lives in the 2008 Wenchuan earthquake. In order to mitigate against such loss of life in the future and undertake future earthquake hazard assessment, we need to make a detailed study of the previous earthquakes to understand their characteristics. Most major earthquakes in the Tibetan Plateau occur in the collision zone between continental plates. The continental plate tectonic can give us information about the internal dynamic causes of earthquakes and help us to assess the cumulative effect that multiple earthquake cycles in actively deforming regions.

### 2.1 Tectonic background

Before the Cenozoic period (~50 Ma), the Tibetan Plateau was composed of a crustal accretion that included 6 plates that ran successively from north to south as indicated by the 5 suture zones within the Plateau (Zhang *et al.*, 2003 and reference therein). In the Cenozoic era, the entire Tibetan Plateau was predominantly influenced by the Indian–Eurasian collision, some of these sutures were reactivated and modified. After the collision, intracontinental convergence and deformation continued across Tibet. Thrusting and sinistral strike-slip faulting have been the dominant crustal deformation

processes that have occurred in Tibet (Tapponnier *et al.*, 2001). From south to north the major fault zones are: The Himalayan Main Thrust fault zone, the Karakorum-Jiali fault zone, the Xianshuihe fault zone, the Kunlun fault zone, the Altyn Tagh -Haiyuan fault zone, and the Red River fault zone. These active fault zones act to divide the whole Tibetan Plateau into different geological units. From north to south, the main active tectonic terranes are Qaidam, Bayan Har, Qiangtang and Lhasa terranes. There are also four suture zones, Anyimaqen- KunlunMuztagh suture zone, Jinsha River suture zone, Bangong-Nujiang suture zone and Indus-zangbo suture zone (Figure 2.1). Earthquakes in the Tibetan Plateau mostly occur along the boundaries of the various blocks (Figure 2.2). GPS measurements indicate that Tibet is currently undergoing eastward block motion and a clockwise rotation due to the ongoing collision (Royden *et al.*, 1997) that is occurring between the Indian and Eurasian plates (Figure 2.2). However, GPS observations are sparse in the central and western parts of the Plateau due to its possessing a remote, and hostile environment.

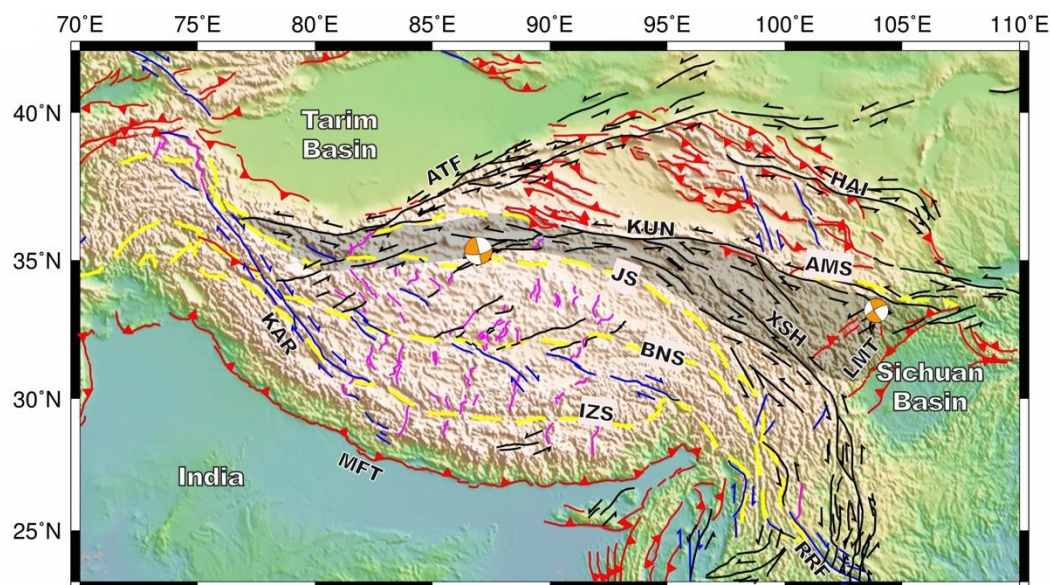


Figure 2.1 Topographic map of the Tibetan Plateau and surrounding region with Quaternary-active faults and geological sutures from the compilation of Taylor and Yin (2009). Dashed yellow lines are geological sutures, red lines are thrust faults, black lines are sinistral strike-slip faults, blue lines are dextral strike-slip faults and magenta lines are normal faults. Two orange focal mechanisms are the earthquakes presented in this thesis. The shadow block highlights the location of Bayan Har terrane. Name abbreviations for major features as follows: AMS, Anyimaqen-Kunlun-Muztagh suture zone; ATF, Altyn Tagh fault; BNS, Bangong-Nujiang Suture; IZS, Indus-Zangbo Suture; JS, Jinsha Suture;



KAR, Karakoram fault; KUN, Kunlun fault; LMT, Longmen Shan Thrust; MFT, Main Frontal Thrust; RRF, Red River fault; XSH, Xianshuihe fault.

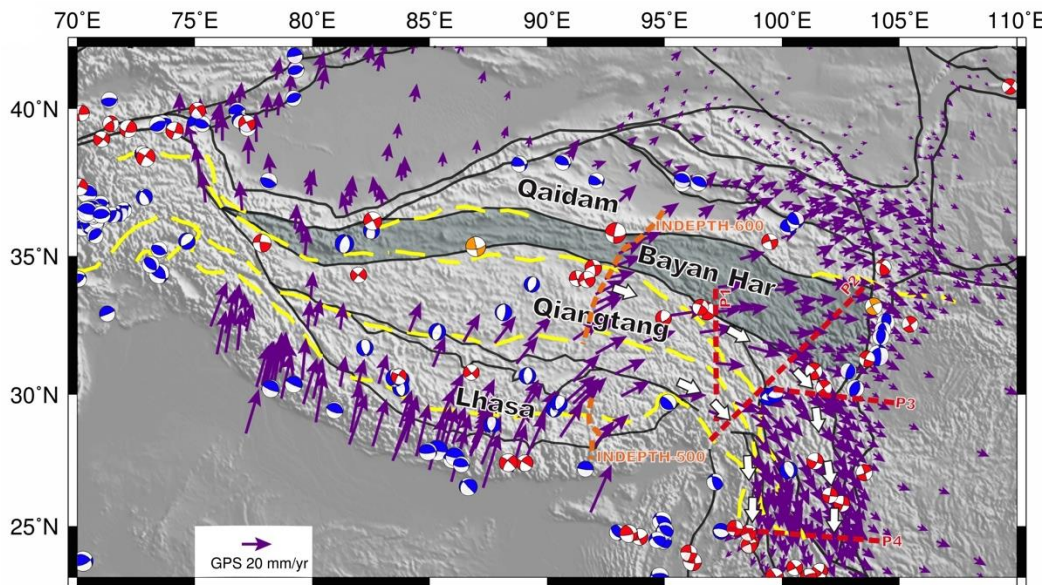


Figure 2.2 Distribution of focal mechanisms ( $M_w > 6$ ) across the Tibetan Plateau since 1976 from the GCMT catalogue. The two orange focal mechanisms are the earthquakes presented in this thesis. Red are strike-slip solutions (rake is within  $45^\circ$ ) and all other earthquakes are blue. Purple arrows are horizontal component GPS velocity vectors relative to stable Eurasia from Gan *et al.* (2007). Dashed orange lines show the location of INDEPTH profile. Dashed red lines (P1–P4) show the location of magnetotelluric data profile in Bai *et al.* (2010). The white arrows connect the regions of highest conductance and inferred location of flow channels (Bai *et al.*, 2010).

## 2.2 Rheological structure of the lithosphere

The tectonic evolution, geodynamics, and rheology of the Tibetan Plateau have been topics for academic debate over a number of decades. To give an explanation for the deformation kinematics and geodynamics of the Tibetan Plateau, two end-member models have been proposed, namely continuum model and block-like model. At one extreme, continental deformation is governed by broadly distributed and continuous viscous flows in the mantle and the crust of the entire Plateau (e.g. England and Mckenzie, 1982). The physical model treats the continental lithosphere as a sheet of material whose deformation is determined by the vertical averages of its mechanical properties (Walters *et al.*, 2017). It does not need to be channelized within the crust or lithosphere and may affect the entire outer shell. A further approach of the viscous sheet model is the channel flow model, which emphasizes that deformation is

dominated by a more rapid ductile flow in the middle and/or lower crust above a stronger upper mantle (Beaumont *et al.*, 2004, Clark and Royden, 2000, Royden *et al.*, 1997, Shen *et al.*, 2001) Channel flow refers to any flow in which a viscosity minimum at some depth strongly localizes horizontal material flow and partially or totally decouples flow at different depths. However, the vertical strength and strain profiles in Tibetan lithosphere cannot be directly measured by geodetic data. The viscoelastic relaxations derived by geodetic data are not sensitive to the upper mantle due to the great crustal thickness of the Tibet area. For example, Ryder *et al.* (2011,2007) and Wen *et al.* (2012) test earth models with separate viscosity at the lower crust and mantle for different earthquake postseismic deformation. The surface deformation predictions by these models have similar results with the conventional two-layer earth models in viscoelastic modelling. The opposite extreme is the block-like model, which actively deforming regions are comprised of interactions between rigid lithospheric plates with the localised deformation occurring along major strike-slip faults (e.g. Replumaz and Tapponnier, 2003, Tapponnier and Molnar, 1976). However, the two end-member scenarios are not mutually exclusive. Thatcher (2007) suggested that although the surface deformation is initially regarded as the rigid block motions, deformation at depth in the ductile part of the lithosphere would possibly be significantly more continuous than it is at the surface. In the past decades, the Tibetan Plateau has employed several GPS stations and expects to distinguish these two end-member models. However, Gaps in GPS data coverage (Figures 2.2) produce the largest model uncertainties. GPS displacement field can be interpreted equally well by either end-member model at both local and regional scales (Gan *et al.*, 2007).

An increasing number of arrays (e.g. PASSCAL, INDEPTH and Hi-CLIMB) have been deployed in the hinterland of the Tibetan Plateau. Such deployments provide additional opportunities to understand the structure and evolution of the Plateau. The crustal thickness is  $65 \pm 5$  km beneath the INDEPTH profile line in central Tibet (Zhao *et al.*, 2001). Owens and Zandt (1997) showed the presence of high

temperatures and the partial melting of the lower crust and upper mantle beneath the Qiangtang and Bayan Har terranes. However, magnetotelluric data from the INDEPTH project is not in agreement with the model proposed by Owens and Zandt (1997). The lowest resistivity (and by inference the highest melt fractions) was detected by the magnetotelluric data in the middle crust underneath the northern Qiangtang terrane but not beneath the Bayan Har terrane (Unsworth *et al.*, 2004, Wei *et al.*, 2001). A new magnetotelluric survey was carried out by Bai *et al.* (2010) in eastern Tibet (Figure 2.2). Two major zones of high conductivity in the middle to the lower crust (20-40 km) were detected. It is inferred that these are zones with aqueous fluid content where deformation takes place most rapidly (Figure 2.2). The conductor is confined above the resistive upper mantle (50 to 100 km depth). However, how much of the lithosphere is weak enough to flow and at what depth, is still not well understood. The evidence presently accumulated is highly localized along nearly linear magnetotelluric profiles. This motivates another question: how pervasive are the high conductivity material across Tibet?

At present, estimations of crustal viscosity account for the topography of the Tibetan Plateau vary over 5 orders of magnitude (e.g.  $< 10^{16}$  Pa s in Clark and Royden (2000),  $1 \times 10^{19}$  Pa s -  $2 \times 10^{21}$  Pa s in Hilley *et al.* (2005)). These estimations were obtained using different methods that deal with a range of time scales, from a few years of postseismic observation to the duration of the formation of the Plateau. It is necessary to determine an appropriate rheological model for understanding the geodynamics of the Tibetan Plateau. Observations of postseismic deformation can give us insights into lithospheric rheology because it illustrates the response of the Earth's interior to coseismic stress changes. Space geodetic techniques such as GPS and InSAR provide an opportunity to measure surface deformation accurately. Indeed, we can test different physical mechanisms to fit observations and place constraints on the rheological structure of the lithosphere. Integrating short and longer-term time scales

of postseismic observation might enable us to better understand the spatial and temporal pattern changes of rheology.

## 2.3 Strike-slip fault and earthquakes

Strike-slip faults are high angle dipping faults where the displacement vector is parallel to the fault strike. They are classified either as transcurrent faults that are confined to the crust or as transform faults that cut a lithosphere plate's boundaries (Sylvester, 1988). Strike-slip earthquakes occur on strike-slip faults. Paleoseismic investigations suggest that earthquakes occur less frequently on continental normal and reverse faults than on strike-slip faults (Sylvester, 1988). From the earthquake catalogue of the past half-century, we can see that strike-slip earthquakes are broadly distributed around the world (Figure 2.3) and that most strike-slip earthquakes happened at shallow upper crust depth (Figure 2.4). Strike-slip zones have benefitted from having the greatest number of comprehensive and highest quality observations. This therefore provides us with an opportunity to look into the structure and rheology of these areas using a wealth of geodetic data.

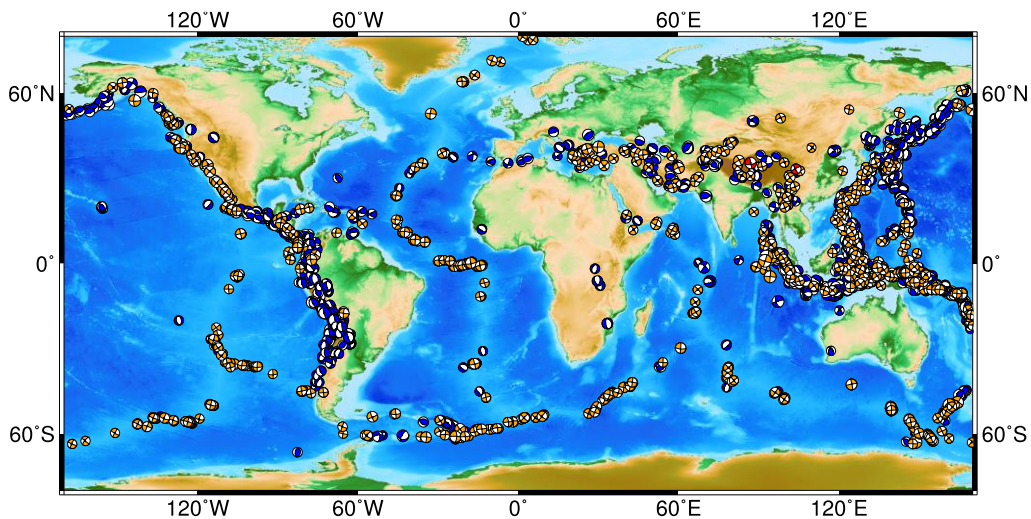


Figure 2.3 Global distribution of  $M_w > 6$  (1976-2017) all earthquakes from the Global Centroid Moment Tensor (GCMT) catalogue. Focal mechanisms for strike-slip earthquakes (rake is within  $20^\circ$ ) are shown in orange. The focal mechanisms for earthquakes studied in this thesis are emphasized in red.

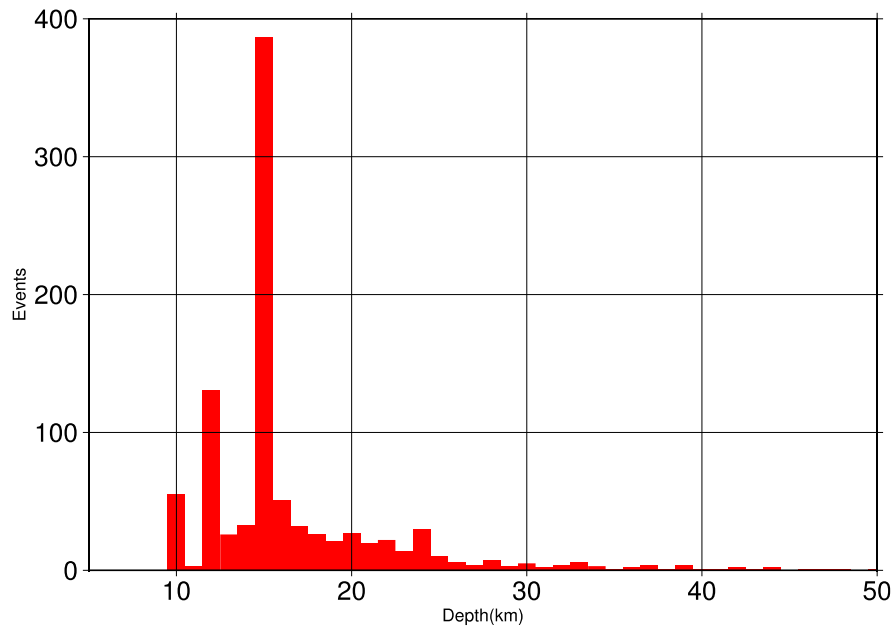


Figure 2.4 Frequency-Depth plots for strike-slip faulting events in the world (the orange dots in Figure 2.3). The depth of these earthquakes is concentrated at 15km.

### 2.3.1 Strike-slip faults in Tibet

The importance of strike-slip faults during Cenozoic tectonic deformation along with the evolution of the Tibetan Plateau have been emphasized by various researchers (e.g. Molnar and Tapponnier, 1975, Zheng *et al.*, 2013). Major strike-slip faults in Tibet include the left-lateral Kunlun, Xianshuihe, and Altyn Tagh faults, and the right-lateral Karakoram fault (Figure 2.1). The roles of strike-slip fault in Tibet correspond to the block-like model or continuum model in different researches. In block-like model, the strike-slip faults play important roles in accommodating relative movements among effectively rigid blocks in continental deformation (e.g. Replumaz and Tapponnier, 2003, Tapponnier *et al.*, 2001). There is limited tectonic deformation within rigid blocks. As a result, the differential motions among rigid blocks require rapid slip and large displacement along strike-slip boundary faults. For example, Tapponnier *et al.* (2001) use the high slip rate (~2-3cm/yr) of the left lateral strike-slip faults to explain the extrusion along Tibet's eastern side. In continuum model, strike-slip faults play a key role in transferring crustal materials and redistributing crustal thickness within the same geological area (e.g. England and Molnar, 1997, Royden *et al.*, 1997). For example, the slip rate of the Altyn Tagh Fault has a

significant decrease from west to east (e.g. Elliott *et al.*, 2008, Meyer *et al.*, 1996). This decrease in slip along the strike-slip fault requires the rock to deform in order to accommodate the convergence. The lateral transfer of material along the Altyn Tagh Fault manifests itself as crustal thickening in Qilian Shan and is merely a redistribution of crustal thickening (Zhang *et al.*, 2007).

Due to the high elevation of the central part of the Plateau (~4.5km), central Tibet is uninhabitable and difficult for people to deploy seismic equipment within. Both geological and geophysical studies pertaining to this part of the country are sparse when compared to other areas. Central Tibet has suffered several moderate to large earthquakes. The earthquakes documented on Bayan Har's boundaries include the 2001  $M_w$  7.8 Kokoxili earthquake, 2008  $M_w$  8.0 Wenchuan, and the 2010  $M_w$  7.1 Yushu earthquake.

The work presented in this thesis focuses on two strike-slip earthquakes that both occurred on the boundaries of the Bayan Har terrane. I first focus on the 8<sup>th</sup> November 1997 Manyi earthquake, which occurred upon the southern boundary of the Bayan Har terrane with a magnitude of 7.6. The second earthquake occurred on 8<sup>th</sup> August 2017 with a magnitude of 6.5, and is located on the eastern boundary of the Bayan Har terrane. Understanding the geodynamic background and the seismogenic mechanisms of these earthquakes can help us to understand the lithospheric structures of the central Tibetan Plateau better.

## **2.4 Lessons from previous studies of these two earthquakes**

Funning *et al.* (2007) examined in detail the coseismic deformation of the 1997  $M_w$  7.6 Manyi earthquake in central Tibet by testing several slip models with different fault configurations and complexities. Single fault uniform slip models, multiple fault uniform slip models and multiple faults with variable slip models have been tested to

fit the observed data. The preferred model has eleven segments with heterogeneous slip. For the Manyi earthquake, the postseismic deformation has been explained by various mechanisms, ranging from afterslip to viscoelastic relaxation and localized deformation in the lower crust (Table 2.1). These studies have all been based on 4 years of postseismic deformation measurements, and were compiled by Ryder *et al.* (2007). A more extended time span of post-seismic observation is required to investigate which mechanism is the most plausible.

Current studies of the 2017 Jiuzhaigou earthquake mainly concentrate on the coseismic phase. The earthquake happened on a buried fault that did not have obvious surface rupture. Shan *et al.* (2017) inverted coseismic slip on one rectangular fault segment, while in the coseismic slip model presented by Sun *et al.* (2018), two smaller rectangular faults were added to the southwest of the major rupture. Which geometry is better needs to be discussed. As the earthquake happened on a buried fault, the lithospheric rheology for this area is still unknown. A study of the postseismic deformation is also needed to place constraints on the rheology of the crust in this region.

Table 2.1 Current studies for the Manyi earthquake

| Stage        | Data coverage | Main feature                                  | Source                       |
|--------------|---------------|---|------------------------------|
| Interseismic | 1992-1997     | $3 \pm 2$ mm/yr prior the earthquake          | Bell <i>et al.</i> (2011)    |
| Coseismic    | 1997          | 11 segments fault                             | Funning <i>et al.</i> (2007) |
|              | 1997          | 7 segments fault                              | Wang <i>et al.</i> (2007)    |
|              | 1997          | Nonlinear elasticity of the crust             | Peltzer <i>et al.</i> (1999) |
| Postseismic  | 1997-2001     | Standard linear/afterslip                     | Ryder <i>et al.</i> (2007)   |
|              | 1997-2001     | Burgers                                       | Ryder <i>et al.</i> (2011)   |
|              | 1997-2001     | Depth-dependent Maxwell-type model            | Yamasaki and Houseman (2012) |
|              | 1997-2001     | Maxwell viscoelastic region with a shear zone | Hetland and Zhang (2014)     |





# Chapter 3

## InSAR Data and Error mitigation

InSAR can map topography and monitor millimetre-scale changes in surface deformation over spans of days to years. The researchers do not need to employ the equipment by themselves; they can easily obtain massive InSAR data at very low expense from different organizations. Therefore, InSAR has grown to be a broadly used deformation mapping technique in Earth science. Since InSAR was first used to quantify coseismic ground displacements that occurred during the 1992 Landers earthquake in California (Massonnet *et al.*, 1993), InSAR has made many contributions to seismological studies. In this chapter, I will first introduce InSAR theory and InSAR processing techniques through open-source software. I will then introduce some error mitigation techniques.

### 3.1 Overview of InSAR

InSAR is a radar-based technique, which can image sub-centimetre deformation of the Earth's surface. Near-Earth satellites carry the imaging Synthetic Aperture Radar (SAR). SAR has cloud-penetrating capabilities because it is a microwave imaging system. It has all-weather and day-night operational abilities. The radiation transmitted from the radar has to reach the scatters on the ground and then return to the radar to form the SAR image. Scatters at different distances from the radar will introduce different delays between transmission and reception of the radiation (Ferretti *et al.*, 2007).

A SAR satellite can look at the same area from slightly different look angles. This step can be completed either at different times by exploiting repeated orbits of the same satellite or simultaneously with two radars installed on the same platform. The former

is the case for the satellites used in my research (e.g. Sentinel, ERS and Envisat). For these satellites, time intervals are available between observations for a multiple of 35 days (12 days for Sentinel).

A SAR measurement is consisting of two parts of information, amplitude and phase. The phase component is a measure of the difference of two-way travel distance between the radar and ground targets (Ferretti *et al.*, 2007). When the satellites revisit the same place, the difference between these two phases will generate the Interferometric SAR configuration, which allows accurate measurements of the radiation travel path because it is coherent. Interferometric SAR can provide valuable information with large spatial coverage, fine resolution, and high measurement accuracy. InSAR technology can display its unique advantages in monitoring earthquake deformation and the earthquake faults' activities in extreme natural conditions. More details on SAR and interferometry can be found in a review written by Massonnet and Feigl (1998).

Satellite radar remote sensing has three typical wavelengths: X-band (wavelength  $\sim 3.1$  cm), C-band ( $\sim 5.6$  cm) and L-band ( $\sim 23.6$  cm). In my study, ERS, Envisat and Sentinel-1 satellites all use C-band wavelength.

$$\varphi_{int} = \varphi_{flat} + \varphi_{topo} + \varphi_{def} + \varphi_{err} \quad (3.1)$$

An interferogram is composed of contributions from topography  $\varphi_{topo}$ , deformation  $\varphi_{def}$ , effects of flat earth projection  $\varphi_{flat}$  and a sum of various errors  $\varphi_{err}$  (see Equation 3.1). NASA's Shuttle Radar Topography Mission (Farr *et al.*, 2007) produces a 90-m digital elevation model (DEM), which is used to remove the topographic contributions ( $\varphi_{topo}$ ).  $\varphi_{flat}$  can be simulated using precise orbit information. E.g. DORIS orbits (Doppler Orbitography and Radio-positioning Integrated by Satellite), which is a tracking system that can be used to determine the precise location of the Envisat satellites. After removing the contributions from orbit and topography, only surface deformation and variable error sources, like orbital

errors, atmospheric delay and inaccurate DEM, are left. Among these error sources, the atmospheric delay is one of the major error sources in the conventional InSAR measurements (e.g. Li *et al.*, 2006, Massonnet *et al.*, 1994, Rosen *et al.*, 1996).

## 3.2 Data processing packages

There are several open source InSAR programs freely accessible for producing interferograms, e.g. Generic Mapping Tools Synthetic Aperture Radar (GMTSAR), InSAR Scientific Computing Environment (ISCE) and Repeat Orbit Interferometry Package (ROI\_PAC). The workflow of processing interferometry is similar for all InSAR programs, but some specific features in each software makes them distinctive and attractive for different users. In this thesis, most interferograms are processed by ROI\_PAC, but in some cases, interferograms are also generated by ISCE.

ROI\_PAC (Rosen *et al.*, 2004) is a collection of FORTRAN and C programs bound together with Perl scripts to finish a repeat pass InSAR processing. This software was first developed at Caltech/JPL (Jet Propulsion Laboratory) during the 1990s with the last major update in August 2009. It can process ERS, Envisat, ALOS, and TerraSAR-X data. The original ROI\_PAC website (<http://roipac.org/>) cannot be opened anymore and the ROI\_PAC install package has not been available for the past two years as the developers' focus has moved to new software (e.g. ISCE).

The ISCE software (Rosen *et al.*, 2011) is the latest InSAR processing package, which builds from some of the FORTRAN and C programs in ROI\_PAC and the newest release version uses Python instead of Perl Scripts. This package will meet most geophysical users' needs in the future. It can handle all types of popular satellite data (e.g. ERS, Envisat, ALOS, TerraSAR-X, Radarsat-2, and Sentinel-1). The processing results from ISCE can be easily used in the Generic InSAR Analysis Toolbox (GAINT, Agram *et al.*, 2013), an open source software for time-series construction.

GMTSAR (Sandwell *et al.*, 2011) is a newly developed package based on the open source Generic Mapping Tool (GMT) package. Therefore, it is easy for users to plot processing results with the GMT software (Wessel and Smith, 1998). GMTSAR relies on accurate satellite orbit information in image registration. It can automatically generate interferograms without human interference. Having many built-in scripts makes GMTSAR attractive because they let users easily conduct a time series or stack InSAR data. It can handle almost all-popular satellite data type (e.g. ERS, Envisat, ALOS, TerraSAR-X, Radarsat-2, and Sentinel-1).

### **3.3 Error mitigation**

When radio signals travel through the atmosphere, they are strongly influenced by propagation delays with the main uncertainties due to water vapour in the atmosphere (Li *et al.*, 2006). In addition, the status of the atmosphere is rarely identical when two images are obtained at different times. Therefore, the difference in the two path delays between two SAR scenes will result in additional shifts in phase signals for both short and long-wavelength phase patterns (e.g. Li *et al.*, 2005), which we call atmospheric noise. Inaccurate baseline estimation will lead to residual orbital error, which will cause long-wavelength phase contributions to interferograms (Massonnet and Feigl, 1998). The errors can reach tens of centimetres, almost at the same level as tectonic signals or even larger (Zebker *et al.*, 1997).

#### **3.3.1 Residual orbital error**

The residual orbital error represents one or two fringes at most. The orbital error is modelled and removed as a linear plane or twisted plane in all correction methods. To minimize the effect of the residual orbital phase, we can calculate the approximation of orbital error as either of the following equations:

$$\varphi = ax + by + cxy + d \quad (3.2)$$

$$\varphi = ax + by + c \quad (3.3)$$

$x$  and  $y$  are range and azimuth coordinates, and  $a$ ,  $b$ ,  $c$  and  $d$  are constants for each interferogram that best fit the phase of the non-deformed area. This residual orbital plane will finally be removed from the whole interferogram. The estimation of the effect of residual orbit errors as a ramp is shown in Figure 3.2.

### 3.3.2 Atmospheric error

Atmospheric delay in interferograms is mainly caused by a different refractive index when radar signals travel through the atmosphere. The refractivity changes are mainly caused by the atmospheric pressure (i.e., hydrostatic or dry delay), temperature and water vapour content (i.e., wet delay). Atmospheric errors are generally composed of ionospheric and tropospheric errors. The ionospheric propagation delay is more significant for larger wavelengths, such as for P and L-band, and comparatively weak for the C-band data (Gray *et al.*, 2000). Because all the satellites used in our research (ERS, Envisat and Sentinel) provide C-band data, we only consider the tropospheric delay. There are several methods to correct tropospheric delay. The correction methods can be divided into two categories: one is based on the SAR dataset itself and the other is based on external models. Ding *et al.* (2008) give a detailed review of multiple techniques that do exist in mitigating errors. Here I briefly introduce each mitigation technique. In the next section I will introduce the methods (e.g. MERIS, ERA) that I used during my research.

Many correction methods are based on external dataset, such as ground meteorological data, GPS observations, and satellite data (e.g. MODIS and MERIS). GPS measurement can derive the accurate estimation of water vapour products that can be used to calibrate the atmospheric effects (Bevis *et al.*, 1992). The only limitation of applying GPS observations is that the spatial distribution of GPS station is general much sparser than that of InSAR data (Ding *et al.*, 2008). Based on the

ground meteorological measurements, various models have been proposed to calculate zenith wet delays (ZWD). The accuracy of the atmospheric delay is very low due to it being calculated from empirical tropospheric models. Moreover, the surface meteorological stations are not evenly and broadly distributed (Ding *et al.*, 2008). Some meteorological model data can also be used to reduce atmospheric effects on InSAR. For example, ERA-interim is a global atmospheric reanalysis that is continuously updated in real time (Berrisford *et al.*, 2011b). The spatial resolution of ERA-interim is  $\sim 80$  km, at a 6 h interval (Dee *et al.*, 2011). MERIS and MODIS correction methods are based on radiometer measurements from different satellites. With the developments of both the accuracy and the resolution of external data in recent years, these correction methods have attracted increasing attention.

Tropospheric errors can also be reduced empirically directly from the interferogram itself, e.g. stacking, pair-wise, a linear correlation between elevation and the interferometric phase. Stacking is the method of temporal averaging of  $N$  independent interferograms to reduce the variance of atmospheric error (Zebker *et al.*, 1997). The stacking method is only appropriate for areas with a linear deformation rate. This method is often used to calculate the interseismic slip rate (e.g. Biggs *et al.*, 2007, Wright *et al.*, 2001). The pair-wise logic method uses a pair-wise logic to discriminate atmospheric perturbations from other signatures (Massonnet and Feigl, 1995), but this method cannot give an exact measure of the atmospheric effects. Permanent scatter (PS) is a sparse pixel-by-pixel based evaluation (Ding *et al.*, 2008, Ferretti *et al.*, 2001). A larger number of SAR images (typically over 30 images) are required by PS technique in order to acquire reliable results. The number and the distribution of reliable permanent scatters in the specific deformation area will have effects on error calibration.

There are many open source packages that can estimate atmospheric corrections, such as TRAIN (Toolbox for Reducing Atmospheric InSAR Noise by Bekaert *et al.*, 2015a), PyAPS (Python based Atmospheric Phase Screen Estimation by Jolivet *et al.*,

2011), and GACOS (Generic Atmospheric Correction Online Service for InSAR by Yu et al., 2017).

## **3.4 Case study of each atmospheric method**

Here, I use the postseismic data of the Manyi earthquake to show the result of the MERIS, ERA-interim and empirically linear relationship between topography and the interferometric phase. For the MERIS and ERA-Interim correction, I used the TRAIN software package. For the empirical calculation, I have written a MATLAB script. The comparison between these methods is shown at the end of this section.

### **3.4.1 MERIS**

MERIS, the Medium Resolution Imaging Spectrometer, is primarily dedicated to ocean colour observations (Bourg and Delwart, 2006) for understanding the role of the oceans and ocean productivity in the climate system, but it also makes contributions to atmospheric and land surface related studies (Bezy *et al.*, 2000). The instrument scans the earth in fifteen spectral bands with a field of view of 68.5°. The global coverage of the Earth is taken within 3 days. Two of these fifteen spectral bands are in the near infrared, which allows measurement of Precipitable Water Vapour (PWV). MERIS and the Advanced Synthetic Aperture Radar (ASAR) are both on board the Envisat satellite. These two instruments work simultaneously during operation time of the satellite. Therefore, the MERIS water vapour product is possible to reduce most water vapour effects on ASAR measurements as two datasets are acquired at the same time. MERIS has two spatial resolutions, 300 m of Full-Resolution (FR) and 1.2 km of Reduced-Resolution (RR). I used the latter to simulate the atmospheric delay. It has also been called wet delay, due to spatio-temporal variations of both water vapour and temperature. The theoretical accuracy of the MERIS data is 1.7 mm under cloud free conditions over land (Bennartz and Fischer, 2001).

MERIS receives radiation reflected by reflected by land, water surfaces and clouds. When clouds are present, the PWV estimate is applicable in the region above the clouds with the highest altitude. To obtain the PWV between the land and the satellite, it is necessary for us to select MERIS data with low cloud cover, as they are very sensitive to the presence of clouds. We can only apply MERIS data to InSAR atmospheric correction under the low frequency of global cloud conditions (25%). This requirement potentially limits the number of interferograms that can be corrected using the MERIS data. PWV is converted to Line-of-sight (LOS) wet delay using the following equation:

$$\delta = \frac{2 \times \Pi \times PWV}{\cos \theta_{inc}} \quad (3.4)$$

$\theta_{inc}$  is the incidence angle of the radar.  $\Pi$  is a dimensionless constant proportionality that is related to the refractivity of moist air and depends on the mean atmospheric temperature (Bevis *et al.*, 1994, Bevis *et al.*, 1992). The value of  $\Pi$  is typically varied between 6.0 and 6.5.

The software package, TRAIN, is used to perform the MERIS correction. The value of  $\Pi$  is 6.4737, which is estimated from sounding data. Out of the 29 SAR acquisitions, only four images have a tropospheric delay estimated, twenty images did not meet the 75 percent threshold and five images did not have MERIS data (Table 3.1). Thus, the MERIS correction method is not suitable for the Manyi area.

Table 3.1 Envisat SAR Data Used in This Study and MERIS coverage in percentage

| Acq. No. | Date     | MERIS coverage (cloud free) |
|----------|----------|-----------------------------|
|          | yyyymmdd | %                           |
| 1        | 20031007 | 9.1                         |
| 2        | 20031111 | 9.1                         |
| 3        | 20031216 | 9.1                         |
| 4        | 20040608 | 1.6                         |
| 5        | 20040713 | 3.1                         |
| 6        | 20041130 | 29.4                        |
| 7        | 20050208 | no value                    |



|    |          |          |
|----|----------|----------|
| 8  | 20050802 | 29.4     |
| 9  | 20051220 | 83.2     |
| 10 | 20080129 | 56       |
| 11 | 20080304 | 56       |
| 12 | 20080408 | 56       |
| 13 | 20080513 | 40       |
| 14 | 20080722 | 40       |
| 15 | 20080930 | 51.1     |
| 16 | 20081104 | 51.1     |
| 17 | 20081209 | 51.1     |
| 18 | 20090217 | no value |
| 19 | 20090324 | 51.1     |
| 20 | 20090428 | no value |
| 21 | 20090602 | 31.1     |
| 22 | 20090707 | 20.5     |
| 23 | 20090811 | 82.7     |
| 24 | 20090915 | no value |
| 25 | 20091020 | 82.7     |
| 26 | 20091124 | 82.7     |
| 27 | 20100309 | 45.3     |
| 28 | 20100727 | 9.1      |
| 29 | 20100831 | no value |

### 3.4.2 ERA-Interim

As mentioned before, the MERIS correction provides only an estimate of the wet component of the troposphere. In addition to the wet component, the tropospheric stratified delay also includes a hydrostatic delay that is caused by the tropospheric pressure difference. Typically, the absolute hydrostatic delay is smaller, but depending on the region it can still be significant.

ERA-Interim is a global atmospheric reanalysis, continuously updated in real time since 1979 (Dee et al., 2011) by European Centre for Medium-Range Weather Forecasts (ECMWF). The ERA-Interim product provides atmospheric information at approximately 80 km spatial resolution on 60 vertical levels from the surface up to 0.1 hPa, four analyses per day, at 00, 06, 12 and 18 UTC (Berrisford *et al.*, 2011a). ERA-Interim outputs can provide both the wet and hydrostatic delay ( $\delta_{total} = \delta_{wet} +$

$\delta_{dry}$ ). The hydrostatic delay can be estimated as a function of ground pressure. An exponential decrease in pressure with height above sea level is assumed by the hydrostatic delay, with a scale height of 8.34 km (Ramon *et al.*, 2003). The equation can be written as follows:

$$\delta = \frac{2 \times k \times P_0 \times \exp(-h/8.34)}{\cos \theta_{inc}} \quad (3.5)$$

$k$  is the conversion factor between surface pressure and LOS hydrostatic delay, assumed to be 0.23 cm/hPa (Davis *et al.*, 1985).  $P_0$  is the atmospheric pressure at sea level and  $h$  is the surface height above sea level, which can be taken from the DEM data.

To employ the ERA-Interim method, we select the ERA-Interim output that is the closest to each SAR acquisition time and date. Zenith tropospheric hydrostatic and wet delays are computed for each of the SAR dates, and then calculate the interferometric phase delays. We calculate the tropospheric delay for one interferogram of Manyi area (Figure 3.1). We can see that hydrostatic delay is relatively smaller than wet delay. We implemented this predicted tropospheric delay to the corresponding interferogram. The final result is shown in Figure 3.2.

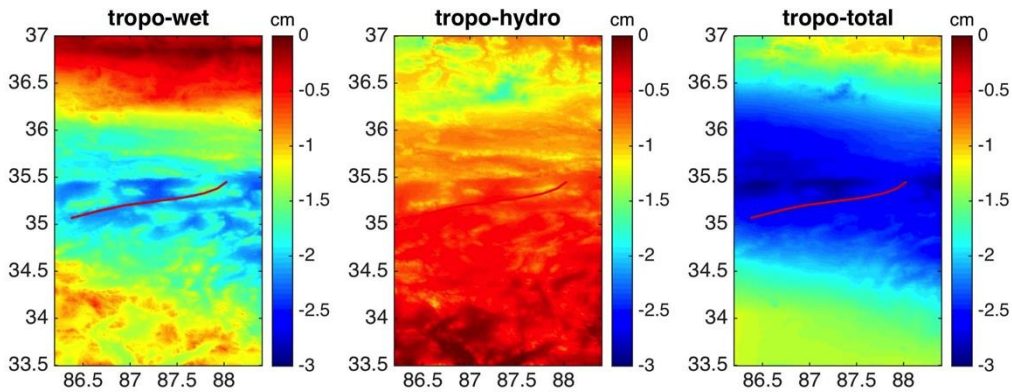


Figure 3.1 The wet and hydrostatic delay predicted by ERA-Interim model from 20031007 to 20041130. The red line indicates the Manyi fault.

The ERA-interim model also has some limitations in its applications. It provides estimations of water vapour every six hours, value change may exist between ERA-interim data and the SAR acquisition. Secondly, the ERA-interim model samples every  $\sim 80$  km. For a typical ASAR image with  $\sim 100$  km range width, only several sample points are available to interpolate water vapour for a simulated atmospheric delay.

### 3.4.3 An empirical relationship between interferometric phases and elevations

Stratified atmospheric delay can also be calculated empirically directly from the interferogram. It is assumed that there is a linear relationship between phase and elevation for each interferogram (Cavalié *et al.*, 2007). The estimation is based on the following equation from data in the non-deforming region:

$$\Delta\delta = k_{\Delta\delta}h + \Delta\delta_0 \quad (3.6)$$

$k_{\Delta\delta}$  is a constant correlation factor between the tropospheric phase and elevation.  $\Delta\delta_0$  just represents a constant variation for the whole interferogram and can be neglected. The tropospheric signal throughout the full interferogram is computed by  $k_{\Delta\delta}h$ . The tropospheric delays and the residual orbital error can always be jointly estimated for each interferogram as  $\varphi_{tropo} + \varphi_{orb} = ax + by + cxy + kh + d$  (Doin *et al.*, 2009). With the deformed area masked out, we can solve for parameters  $a$ ,  $b$ ,  $c$ ,  $d$ ,  $k$ , using a least square minimization. This method has been successfully applied in many previous studies, such as the Manyi earthquake (Feng *et al.*, 2018), and Damxung earthquake (Bie *et al.*, 2014).

Figure 3.2 shows the result from the ERA correction method and linear correction method, with the residual orbital error correction. For the Manyi earthquake area, it seems that the ERA model introduces more noise to the corrected interferogram due

to its lower resolution. The linear estimation can correct the InSAR data better than ERA correction for the Manyi data. MERIS is abandoned because the high frequency of cloud conditions in the Manyi area cannot meet the requirement. Therefore, we prefer to use the linear estimation method to correct all interferograms of the Manyi earthquake.

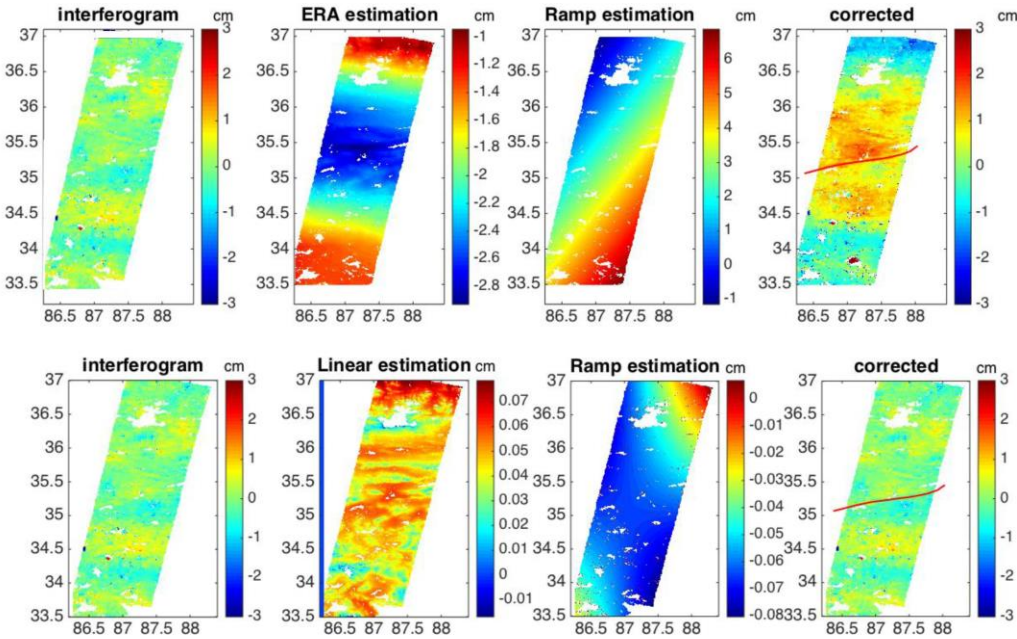


Figure 3.2 Two interferograms with the same date in the different format (20031007 to 20041130). The top one uses ERA correction method. The bottom one is using linear estimation to correct the data. The red line indicates the location of the Manyi fault.

# Chapter 4

## Geodetic Modelling

My thesis is mainly concerned with modelling deformation at the earth's surface. The modelling aims to interpret geodetic observations and to understand physical processes beneath the Earth surface. The viscoelastic model and afterslip model are the two basic mechanisms to explain the postseismic deformation. These two mechanisms will introduce different temporal-spatial deformation pattern. This chapter presents the basic elastic and viscoelastic theory. Outputs from different codes are compared for simple synthetic fault geometries.

### 4.1 Viscoelastic modelling

It is accepted that the outer part of the continental crust where earthquakes occur acts elastically, except for faults, which are subject to friction laws (Byerlee, 1978). However, the rheology of the material beneath this elastic layer is less certain.

Viscoelastic rheologies are of crucial concern throughout this thesis, as it is thought that material in the middle to lower crust and upper mantle may display viscoelastic behaviour. Deformation can be modelled, as a rheological system involves both elastic (at short timescales) and viscous behaviour (Bürgmann and Dresen, 2008). Various combinations of linear elastic elements and linear viscous elements can interpret the basic viscoelastic stress-strain relationship. The deformation of a viscous element is time-dependent, with the temporal characteristics depending on the viscosity  $\eta$ , of the viscous material. The most common rheologies are the Maxwell rheology and the Burgers rheology.

The Maxwell rheology consists of a spring and dashpot in series. Maxwell materials have an immediate elastic response due to an elastic spring, but ultimately the dashpot dominates behaving as linear Newtonian fluids with a steady-state strain rate. This is the simplest linear viscoelastic rheology. The constitutive relationship for deformation of a Maxwell rheology can be written as follows:

$$\dot{\varepsilon} = \frac{\dot{\sigma}}{\mu} + \frac{\sigma}{\eta} \quad (4.1)$$

where  $\eta$  and  $\mu$  are the viscosity and shear modulus of the dashpot and spring respectively,  $\sigma$  and  $\varepsilon$  are stress and strain respectively. The dot denotes time derivative. The Maxwell rheology relaxes exponentially with an initial stress  $\sigma_0$  in postseismic relaxation as:

$$\sigma = \sigma_0 e^{-\frac{\mu t}{\eta}} \quad (4.2)$$

Here, the Maxwell characteristic relaxation time  $\tau = \eta/\mu$ . At time  $t$ , the postseismic deformation can be adequately described by the exponential function (e.g. Savage et al. 2003) in form as  $A(1 - e^{-t/\tau_{exp}})$ .  $A$  and  $\tau_{exp}$  are constants. This exponential equation is often employed to approximate the geodetic time-series of postseismic deformation.

The mechanical analogue of Burgers body consists of a Maxwell fluid and a Kelvin solid assembled in series (Figure 4.1). The Kelvin solid accommodates the transient deformation during early stages of postseismic deformation, and the Maxwell fluid response for the following steady deformation. Therefore Burgers rheology has two relaxation times. The relaxation time of the transient Kelvin response  $\tau_2 = \eta_k/\mu_k$  is shorter than the steady-state relaxation time  $\tau_1 = \eta_m/\mu_m$ . The Kelvin shear modulus to the Maxwell shear modulus is about 1/3 or less in crustal materials, and the Kelvin viscosity is about half or even less than that of the Maxwell viscosity (e.g. Carter and Avelalle.Hg, 1970, Hetland and Hager, 2006).

Standard linear solid is another viscoelastic rheology known as the Kelvin solid in series with a spring. It is the extreme case of the Burger rheology when the viscosity of the Maxwell fluid element became infinite. A graphical representation of the different rheologies is shown in Figure 4.1.

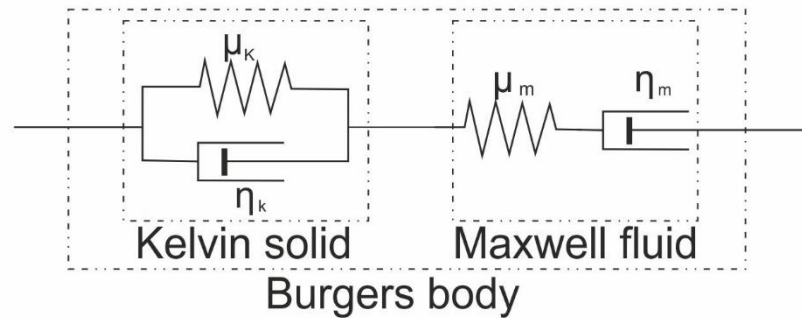


Figure 4.1 Mechanical analogues for different viscoelastic model, consisting of different combinations of spring and dashpot.  $\mu$  and  $\eta$  represent the shear modulus and viscosity of the elastic and viscous elements, respectively.

#### 4.1.1 Viscoelastic computations

As introduced in the last section, the viscoelastic relaxation is one of the major mechanisms to explain time dependent postseismic deformation. Three open source codes, RELAX (Barbot and Fialko, 2010), VISCO1D (Pollitz, 1997) and PSGRN/PSCMP (Wang *et al.*, 2006) are used in this thesis to model time-dependent postseismic viscoelastic deformation.

RELAX and PSGRN/PSCMP both use an elastic Green's function approach to calculate the time-dependent postseismic deformation of a layered elastic/viscoelastic half space; VISCO1D uses a spherical harmonic expansion of spheroidal and toroidal motion modes to calculate time-dependent postseismic deformation of a stratified viscoelastic Earth model at any depth (Pollitz, 1997). In all codes, the user defines the rheological structure and properties. VISCO1D and PSGRN/PSCMP can model various viscoelastic models e.g. the standard linear solids and Burgers body, while RELAX can model lateral rheological heterogeneities. VISCO1D can compute

displacements at individually specified coordinates, so this is useful for modelling at irregularly distributed observation points typical of geodetic datasets. In contrast, RELAX computes displacements on a regular grid, so it is better suited to experimental calculations of the type carried. PSGRN/PSCMP can model both regular and irregular observation points in either geophysical or local coordinate systems. Besides, the database of Green functions generated by PSGRN can be used repeatedly for calculating the postseismic deformation of different earthquakes.

To test and compare the codes, postseismic displacements from strike-slip faulting are considered. In the modelling, the Earth consists of an elastic lid of 15 km thickness overlying a Maxwell viscoelastic half-space. For the strike-slip faulting case, a uniform left-lateral slip of 1 m is designated with fault length (20 km) and width (10 km). The fault is aligned with the y-axis (Figure 4.2). Here, fault width means the downdip extension of the fault, measured from the upper trace of the fault to its bottom. Output surface displacements for comparisons from the three codes are computed for one relaxation time.

The spatial patterns of the outputs from different codes are consistent (Figure 4.3). Two profiles are drawn to show the differences. For the east and north component of displacements, the difference is about 6 percent of the maximum displacement (Figure 4.4). The difference between outputs from different software could be due to the slightly different input parameters. For example, we need to provide the seismic velocity model, density and viscosity etc. in the PSGRN/PSCMP, while in the RELAX we need to provide the relaxation time and elastic parameters.



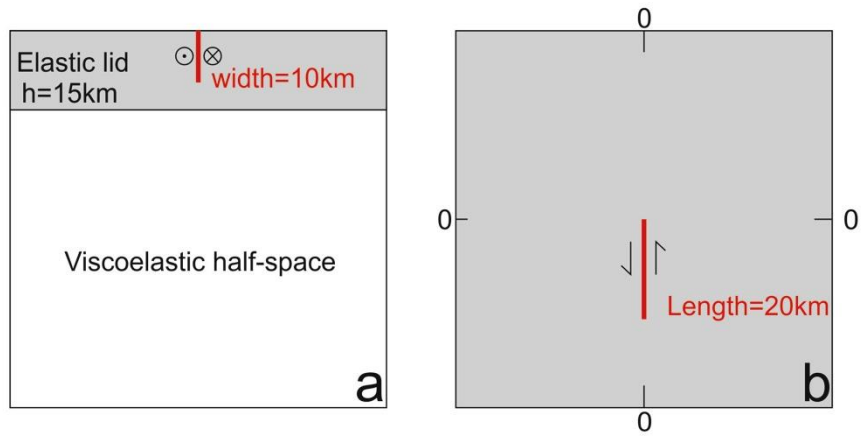


Figure 4.2 The sketch structure of the fault used in the software testing. (a). This is the side view. (b). This is the top view. The central point of the fault is at  $(0, -10)$  point.

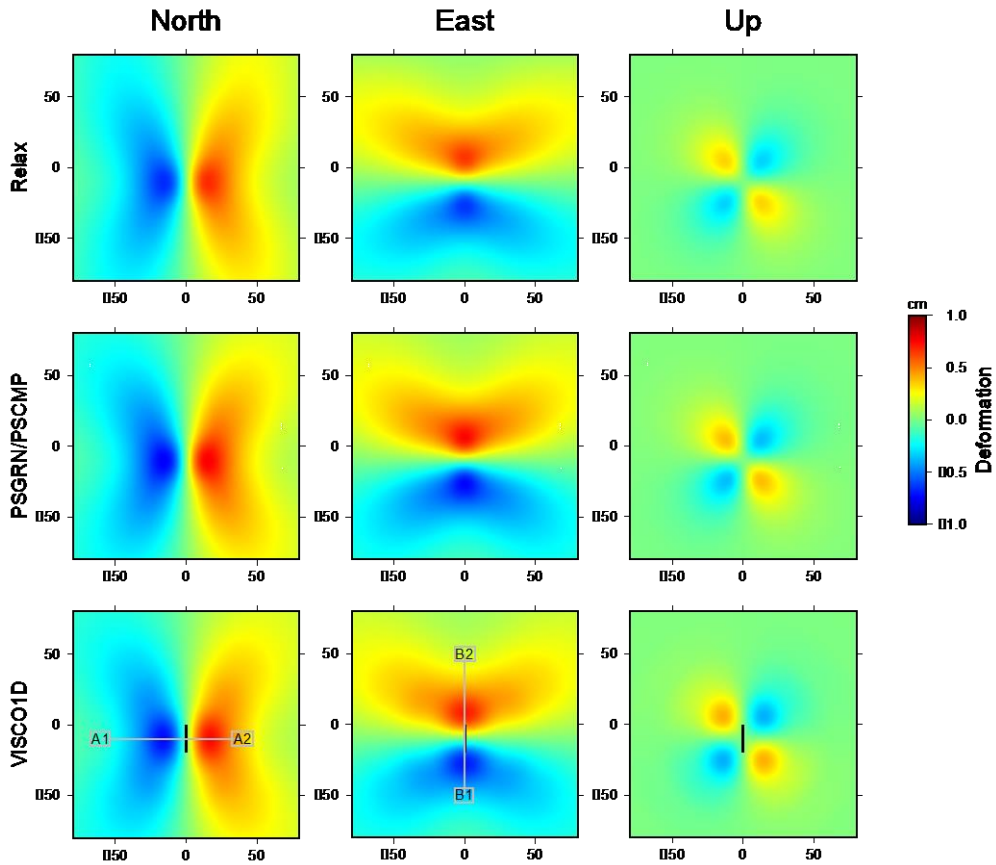


Figure 4.3 Comparison of surface deformation from RELAX, PSGRN/PSCMP and VISCO1D. Top panels show surface displacements in three directions calculated by RELAX, middle panels are outputs from PSGRN/PSCMP and bottom panels show outputs from VISCO1D. X and Y axes are in units of km. The black line shows the location of the fault. Please note that the centre of the fault is at  $(0, -10)$  point. AA and BB are the two profiles in the comparisons.

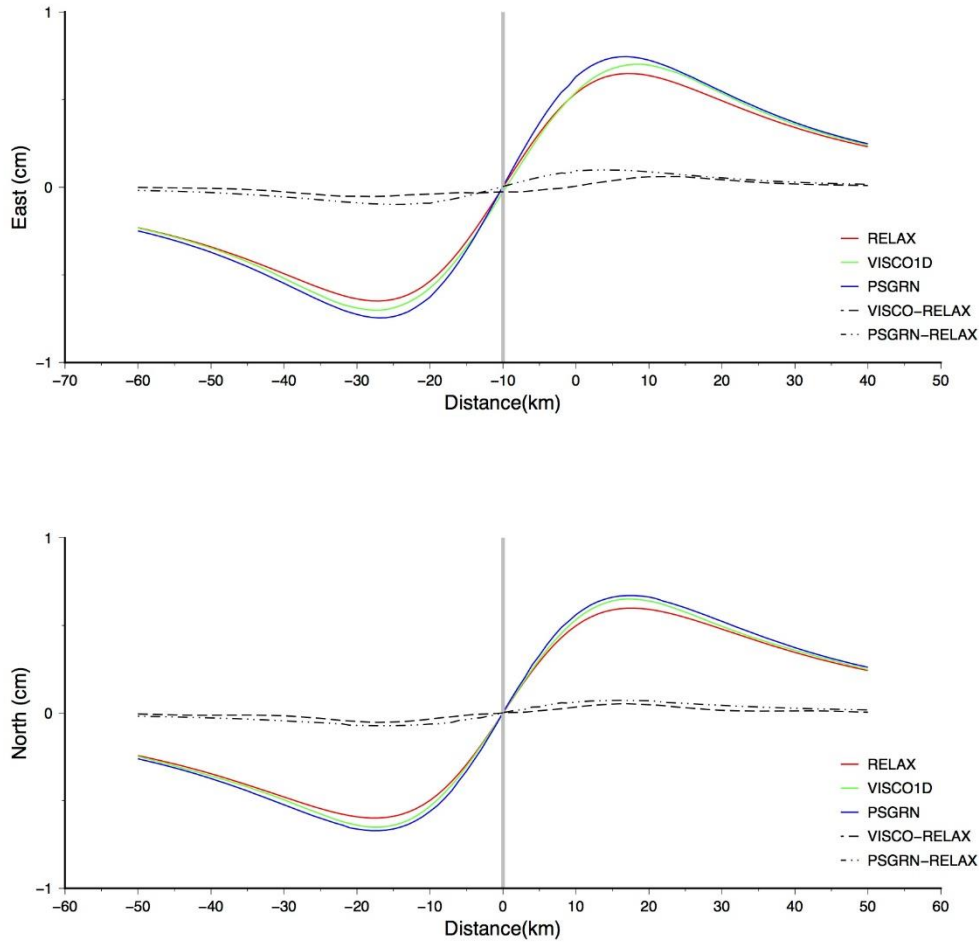


Figure 4.4 Comparison of surface displacements in east (top) and north (bottom) directions along a profile perpendicular to the fault and passing through its centre. Grey line marks the fault surface trace.

#### 4.1.2 Use of the viscoelastic code in this thesis

According to my research demand, I chose VISCO1D as the main modelling software for the Manyi earthquake and PSGRN/PSCMP for the Jiuzhaigou earthquake calculation.

Pollitz (1992, 1997) presented the general theory of VISCO1D. There are two sets of programs in VISCO1D. One is designed for non-gravitational viscoelastic response and the other is designed for gravitational viscoelastic response. Rundle (1981, 1982) discussed the justification of the neglect of perturbations in the gravitational potential for postseismic relaxation calculations on a layered half-space. A test of these two

different cases is taken to see the difference. The resulting surface postseismic displacement and corresponding profile at one relaxation time are shown in Figure 4.5 and Figure 4.6, respectively. The agreement is perfect and the difference is negligible. As the non-gravitational case runs considerably faster than the gravitational case, we only use the non-gravitational programs.

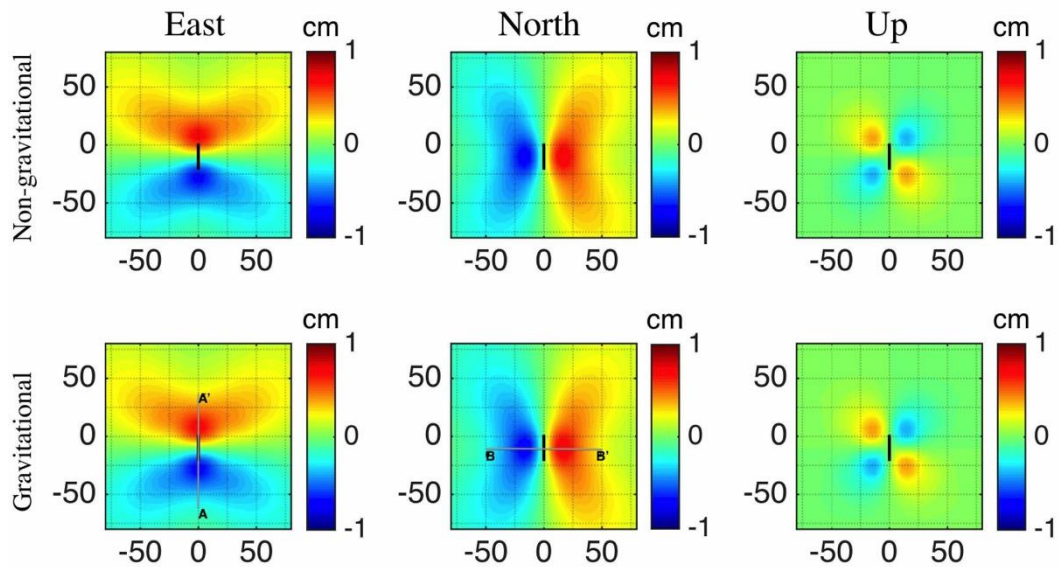


Figure 4.5 Comparison of outputs from the different case of VISCO1D at one Maxwell time after a strike-slip event. Top panels show displacements in three directions of non-gravitational case, bottom panels are outputs from the gravitational case. Note that the fault is the same as the previous section. X and Y axes are in units of km.

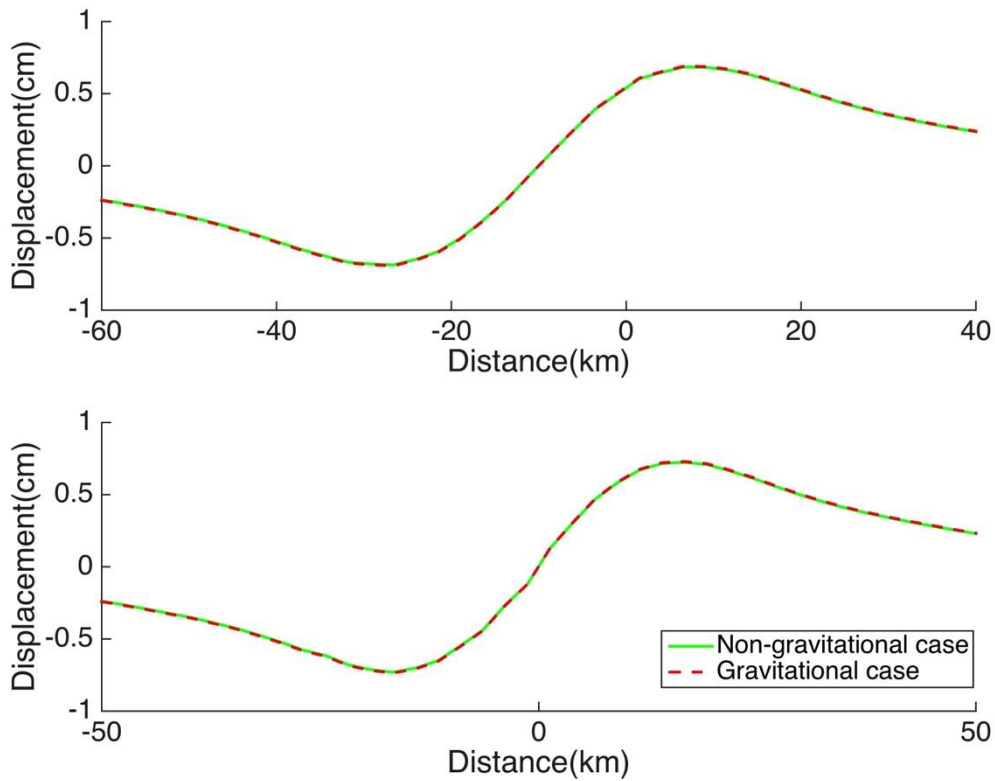


Figure 4.6 Surface vertical displacements from viscoelastic-gravitational relaxation (red curve) or non-gravitational relaxation (green curve) following a strike-slip event. The profiles' location are shown in the fig 4.5.

### 4.1.3 Synthetic test of the viscoelastic models

The Maxwell model (e.g. Ryder *et al.* 2014), the standard linear solid model (e.g. Ryder *et al.* 2007) and the bi-viscous Burgers body model (e.g. Pollitz 2005) are the most common used viscoelastic models to simulate viscoelastic relaxation. In this section, I use simple fault geometry to show the difference between each viscoelastic model of strike-slip faults that can account for postseismic deformation. PSGRN/PSCMP (Wang *et al.*, 2006) is adopted to do the synthetic viscoelastic relaxation test.

Firstly, we use the simple Maxwell model to test the influence of the thickness. The earth model is identical in all modelling except the thickness of the elastic layer. From the figure 4.7, we can see that the thicker of the elastic layer, the more disperse of the deformation. The elastic layer determines the spatial pattern and amplitude of

deformation. Therefore, to model a postseismic deformation, a thicker elastic layer always requires a smaller viscosity to fit the data.

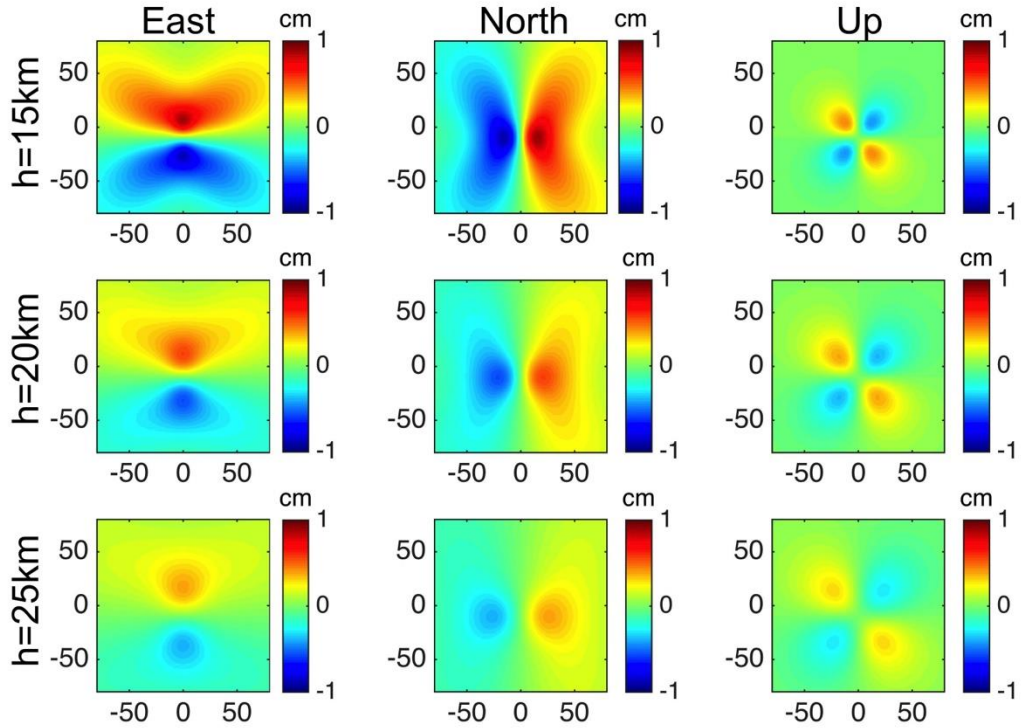


Figure 4.7 Surface deformations predict by different elastic layer.  $h$  means the thickness of the elastic layer. X and Y-axis in km.

To test different viscoelastic rheologies, an Earth model is used containing a 15 km thick elastic lid, in which the fault is embedded, above a viscoelastic half-space. The parameters of the synthetic earth model are given in supplementary Table S4.2. The fault geometry is shown in Figure 4.2. The parameters of each viscoelastic model are listed in table 4.1. The full surface displacements are displayed in Figure 4.8 and the profile velocities are shown in Figure 4.9. We can see that all viscoelastic modelling have a similar spatial pattern, the only difference is the magnitude of the deformation lobes. For the given elastic shear modulus  $\mu_m$ , the viscosity  $\eta_m$  controls the timing of the processes (Figure 4.8). In the standard linear solids model, for a given viscosity  $\eta_k$ , a weaker  $\mu_k$  leads to a larger relaxed displacement and longer relaxation time. In the Burgers body model, if the  $\eta_k$  is greater than  $\eta_m$ , the Maxwell and Burgers body model

will have similar surface deformation pattern. From the velocity profiles, the deformation gradient decays quickly at the near field, while there is a slower decay in the far field (Figure 4.9). Although the surface deformations are not entirely identical, some of the profiles almost overlap with each other (e.g. model 4 and 8). Therefore, when we compare the geodetic observation with the modelling result, we should pay attention on both spatial and temporal characteristic of the data.

Table 4.1 Material parameters of the earth models used in this section

| No. | Rheology               | $\eta_m$ (Pa s)    | $\eta_k$ (Pa s)    | $\alpha = \frac{\mu_k}{\mu_k + \mu_m}$ |
|-----|------------------------|--------------------|--------------------|--|
| 1   | Maxwell                | $5 \times 10^{18}$ | /                  | $1(\mu_k = \infty/\eta_k = \infty)$    |
| 2   | Maxwell                | $1 \times 10^{18}$ | /                  | $1(\mu_k = \infty/\eta_k = \infty)$    |
| 3   | Standard linear solids | /                  | $1 \times 10^{18}$ | $0.667(\mu_k = 2\mu_m)$                |
| 4   | Standard linear solids | /                  | $1 \times 10^{18}$ | $0.250(\mu_k = \frac{1}{3}\mu_m)$      |
| 5   | Standard linear solids | /                  | $5 \times 10^{18}$ | $0.250(\mu_k = \frac{1}{3}\mu_m)$      |
| 6   | Burgers body           | $5 \times 10^{18}$ | $1 \times 10^{18}$ | $0.667(\mu_k = 2\mu_m)$                |
| 7   | Burgers body           | $5 \times 10^{18}$ | $1 \times 10^{18}$ | $0.250(\mu_k = \frac{1}{3}\mu_m)$      |
| 8   | Burgers body           | $5 \times 10^{18}$ | $5 \times 10^{18}$ | $0.250(\mu_k = \frac{1}{3}\mu_m)$      |
| 9   | Burgers body           | $1 \times 10^{18}$ | $5 \times 10^{18}$ | $0.250(\mu_k = \frac{1}{3}\mu_m)$      |

Note:  $\eta_m$  represents steady state viscosity dashpot of the Maxwell body.  $\eta_k$  represents transient viscosity dashpot of the Kelvin body.

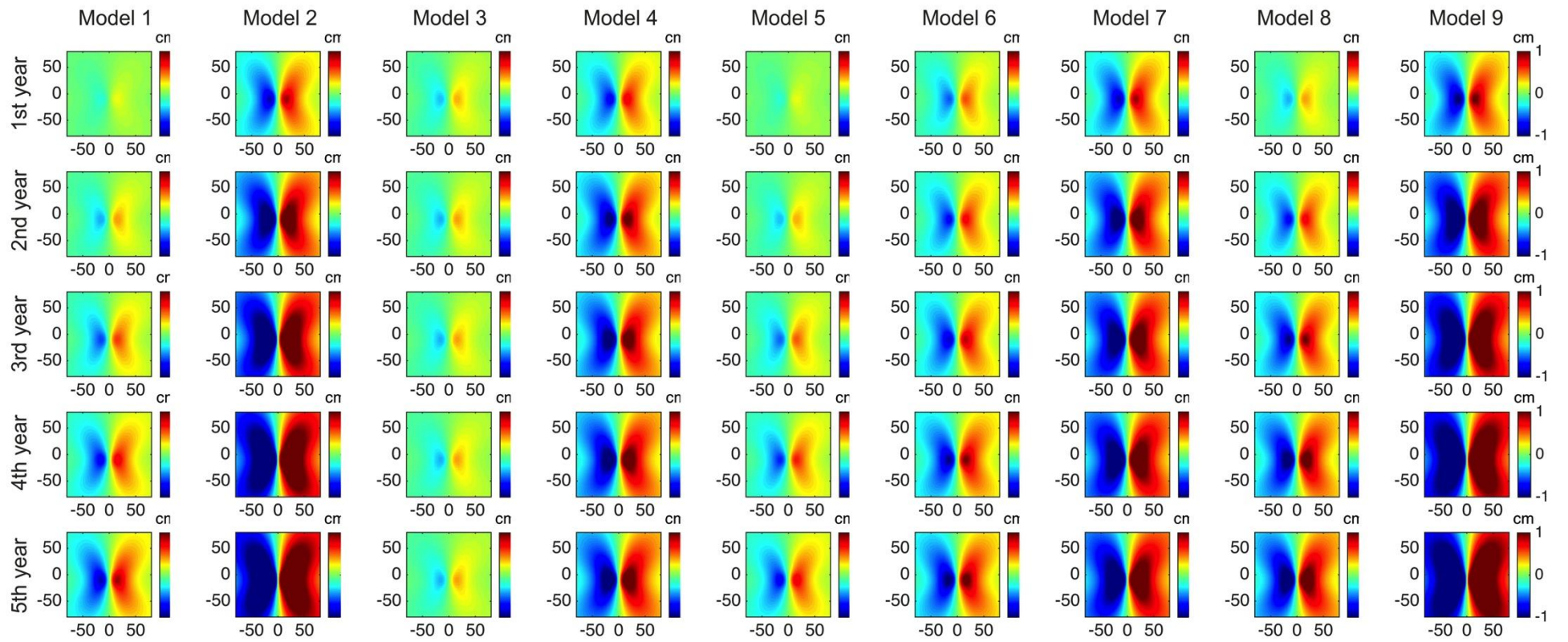


Figure 4.8 north-surface displacement predict by the viscoelastic models (table 4.1). X and Y-axis in km

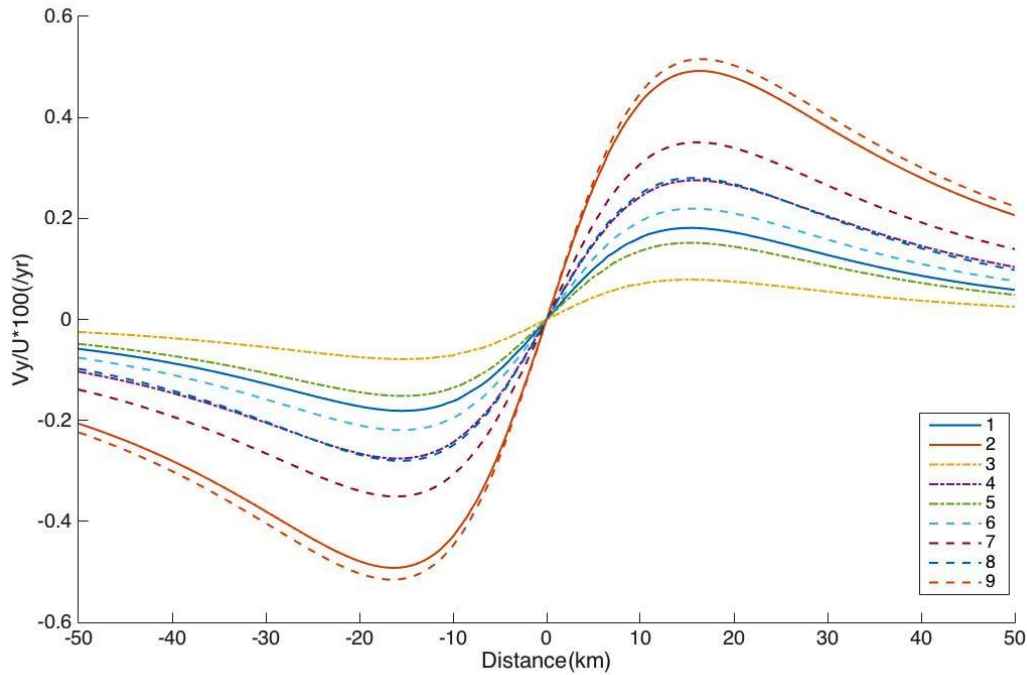


Figure 4.9 North-velocity at the surface from viscoelastic relaxation following a strike-slip event, normalized to the uniform coseismic slip on the fault. The serial numbers correspond to the model serial number in table 4.1.

## 4.2 Elastic modelling

Hooke's law is the most general form to express the relationship between stress and strain. An elastic medium deforms instantaneously when stress is applied, there is no time dependence. In practice, the Earth usually behaves elastically between faults in computations of coseismic deformation because on the seconds to minutes time scale of coseismic deformation, time-dependent effects, such as viscous flow, are negligible. Elastic dislocation theory allows modelling the surface displacement of an elastic medium due to slipping across a dislocation.

### 4.2.1 Elastic computations

#### 4.2.1.1 Elastic half-space

Okada (1985) gave an analytic solution for the surface displacement due to both shear and tensile dislocation on a finite rectangular fault embedded in uniform, isotropic



elastic half-space. Equivalent analytical expressions for internal displacement are further given by Okada (1992). Ground deformation produced by earthquakes or magmatic intrusion can easily be simulated by this elastic dislocation theory in the analytical form. To forward model the surface displacement, a set of nine parameters are required as input, including strike, dip, rake, the fault's upper and lower depth, the central coordinates of the fault's trace, fault length and slip. For complex fault systems, a collection of rectangular fault patches can be used to obtain a more detailed slip distribution model with variable slip (e.g. Jónsson *et al.*, 2002). The size of these rectangular patches may vary substantially in both strike and dip (e.g. Simons *et al.*, 2002). The Okada model is applied for the computation of displacements from a dislocation in a homogeneous elastic medium.

Okada wrote a FORTRAN code `dc3d.f` to compute internal displacements, strains and stresses due to slip on a rectangular fault in a uniform, isotropic elastic half-space. The elastic dislocation theory presented by Okada (1985, 1992) is the mathematical basis of this code. Okada (1985) lists equations to compute the surface displacements and then expands the expressions to calculate the internal deformation (Okada, 1992). Peter Cervelli converted the FORTRAN code to run in Matlab (`disloc3d`). I use a left-lateral strike-slip fault to test this Okada code. The fault geometry is 20 km long with 10km width and is aligned with the y-axis. The uniform slip is 1m, which is the same as the fault used in viscoelastic modelling. We can see that the surface displacement caused by the Okada model mainly concentrates in the near field of the fault (Figure 4.10).

#### 4.2.1.2 Layered elastic model

The Okada dislocation theory (Okada, 1985) has been successfully applied to predict crustal deformation in a uniform elastic half-space. However, in reality, the Earth is not homogenous and we need to consider the effects of vertical and lateral inhomogeneity, Earth curvature and obliquely layered media (e.g. Savage, 1998,

Wang, 1999, Zhu and Rivera, 2002). For deformation simulation of shallow events at relatively small area, the effect of spherical Earth can be neglected (Wang *et al.*, 2006). However, sometimes the considerable effects caused by crustal layering need to be taken into consideration. Wang *et al.* (2003) developed numerical codes called EDGRN/EDCMP to model deformation caused by an earthquake in a multi-layered crust. EDGRN/EDCMP is included in the PSGRN/PSCMP package. Theoretical details of the calculation details can be found in Wang *et al.* (2003). For a layered Earth model, the input parameters are P wave and S-wave velocity, layer thickness and density.

To examine the effects of a layered medium, we use a synthetic slip model to test the theoretical surface displacements. Four layers of crust information exist in the database of Crust1.0 (Laske *et al.*, 2013) for the Tibetan Plateau region that is used (Table S4.2 in supplementary). The synthetic fault geometry is 20 km long with 10 km width. The fault is aligned with the y-axis and has a 1m slip on the fault plane. This fault is the same as the one used in the elastic half-space test. Figure 4.10 shows that the surface deformations calculated with the layered elastic model have a good agreement with the elastic half-space Earth model. The difference in each direction is small ( $\sim 2\%$ ). Therefore, we use the elastic half-space model in afterslip inversion of the Manyi earthquake in Chapter 5.

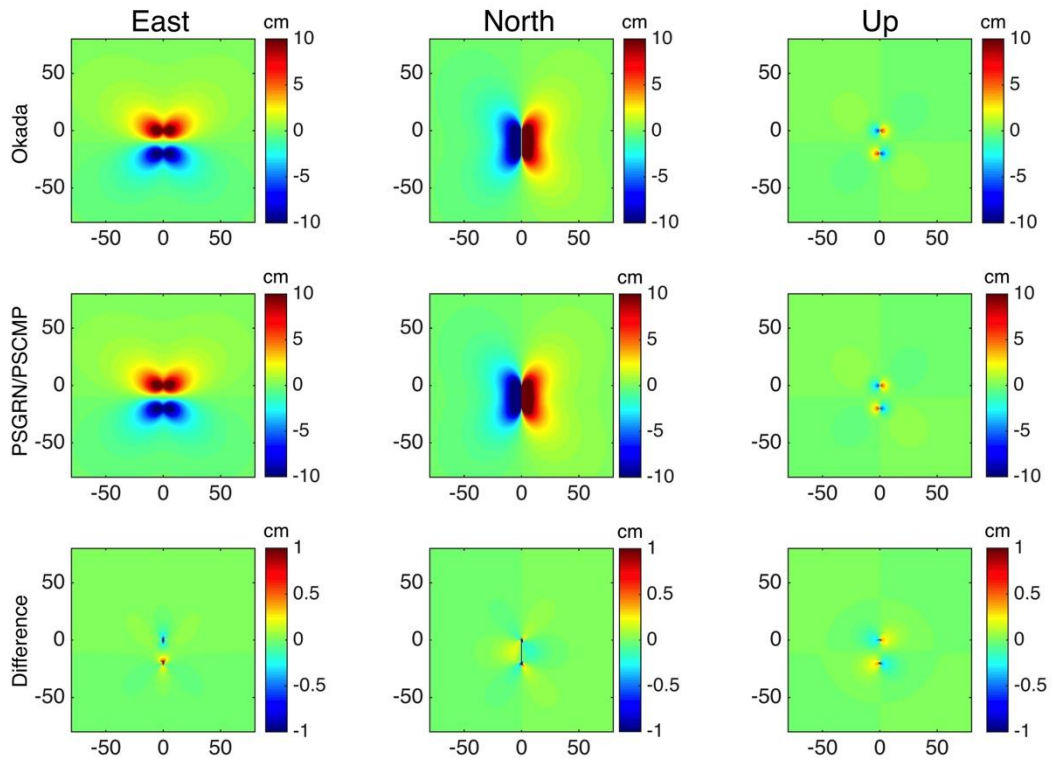


Figure 4.10 Surface deformation outputs were calculated using Okada's method and Wang et al.'s method, respectively. X and Y-axis in km. The colour scale of the third row is different with the other two rows.

### 4.3 Distributed slip on the fault

To obtain the slip distribution model from geodetic observations, two steps are usually implemented. The first step is to find a set of fault parameters that can best describe the observed data. The parameters include fault geometry, location and slip sense, which are non-linearly related to the surface displacement. The second step is to do a linear inversion to obtain the slip distribution model. For coseismic modelling, this usually includes both nonlinear and linear calculations. For afterslip inversion of postseismic modelling, the fault geometry is generally obtained from previous coseismic studies. Only the linear calculation is involved in this stage.

#### 4.3.1 Nonlinear process: determination of fault geometry

In this stage, the slip is always assumed to be uniform across the rectangular fault. Sets of parameters (including strike, dip, slip, rake, upper and lower depth of the fault, fault length and location) are randomly generated for the Okada model to calculate surface displacements. The optimal solution and error bounds are obtained based on multiple tests. Monte Carlo method, simulated annealing algorithm, Bayesian algorithm etc. are widely used to solve this nonlinear problem (e.g. Jónsson *et al.*, 2002, Wright *et al.*, 2003, Bagnardi and Hooper, 2018). In reality, the surface location parameters of the fault can be obtained from the geodetic observation. Therefore, the calculation process can be accelerated.

### 4.3.2 Linear process: invert for slip distribution

After the fault geometry has been resolved, determining the distributed slip on the fault plane is a linear calculation. For this step, the rectangular fault with certain fault geometry will be discretized into multiple small patches. Generally, the fault discretization is carried out with a uniform size (e.g. Funning *et al.*, 2007, Jónsson *et al.*, 2002). Sometimes the rectangular fault will be divided with depth-dependent variation (e.g. Fialko, 2004). A resolution test is usually required to examine the sensitivity of slip model. The Green's function matrix is calculated by the Okada model. The matrix describes surface displacement caused by unitary slip on each fault patch at each observation point. The primary linear matrix equation can be written as follows:

$$\mathbf{G}\mathbf{m} = \mathbf{d} \quad (4.3)$$

where  $\mathbf{G}$  is the Green's matrix that relates to the surface deformations to the model,  $\mathbf{m}$  is the slip solution and  $\mathbf{d}$  is the data displacement. To avoid oscillations in the fault slip, second-order Laplacian smoothing operator  $\nabla^2$  and smoothing factor  $\kappa^2$  are brought in to help us to select an appropriate smooth slip model (Jónsson *et al.*, 2002). The equation to be solved is:

$$\begin{bmatrix} \mathbf{G} \\ \kappa^2 \nabla^2 \end{bmatrix} [\mathbf{m}] = \begin{bmatrix} \mathbf{d} \\ \mathbf{0} \end{bmatrix} \quad (4.4)$$

The Green's functions ( $\mathbf{G}$ ) can be computed using the Matlab code `disloc3d` (Okada/Cervelli), `EDGRN/EDCMP` (Wang *et al.*, 2003), `SDM` (Wang *et al.*, 2013b), etc. Solving a linear least-squares equation derives final slip distribution ( $\mathbf{m}$ ). The Earth model considered in the above modelling procedures is homogeneous elastic half-space. For afterslip inversion, the fault geometry is always obtained from previous coseismic studies. During the inversion of the postseismic afterslip, the slip is allowed to occur on extended depth of the coseismic rupture. Chapter 5 gives a detailed description of this inversion step.

An example of synthetic LOS displacements, produced by elastic computations of the half-space (Figure 4.10), is used to show the linear process. The input data is synthesized by a simple strike-slip faulting parameters using classic elastic dislocation theory (Okada, 1985). The synthetic fault geometry is 20 km long with 10km width and has 1m slips on the fault plane (Figure 4.11a). LOS displacement is synthesized using incidence and azimuth angles of  $23^\circ$  and  $-166^\circ$  respectively (Figure 4.12b). The LOS displacement of Figure 4.12b is taken as the  $\mathbf{d}$  in equation 4.4. The smoothing factor  $\kappa^2$  is determined by the knee of the L-curve (Figure 4.13), which allows both parameters to be low.  $\mathbf{m}$  is the output of the distributed slip, which is shown in Figure 4.6. The predicted LOS displacement (Figure 4.12a) is produced by forward calculation of the distributed slip. This inverted output slip has a very similar distribution pattern to the input slip distribution. The misfit between the data and model is relatively small (Figure 4.12c).

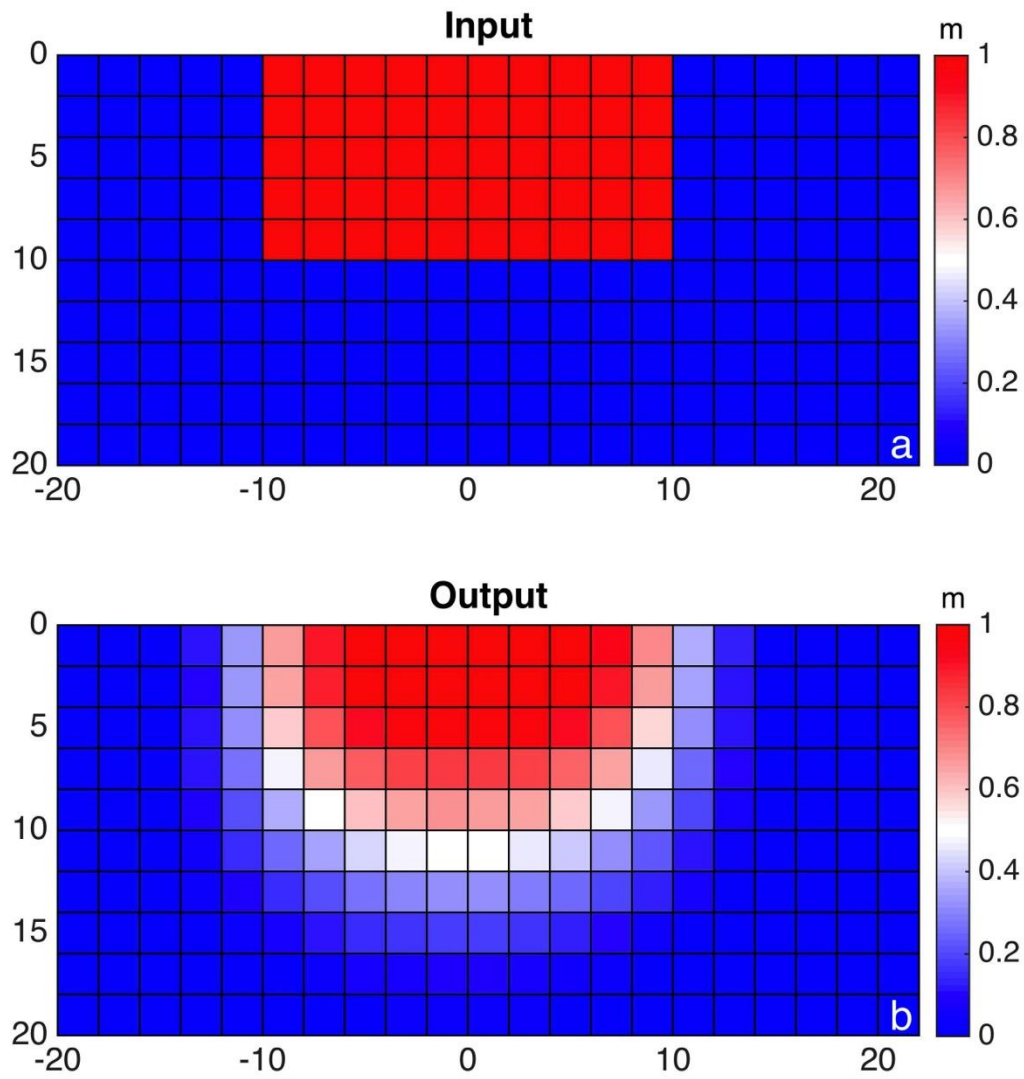


Figure 4.11 (a). The original input fault geometry to generate synthetic surface displacement. (b) Modelled slip distribution on the fault plane.

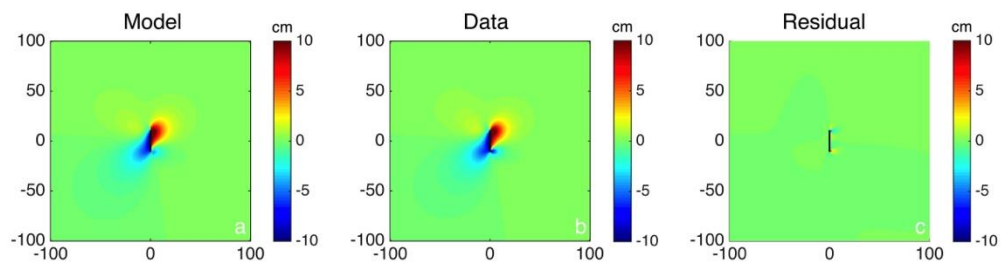


Figure 4.12 The comparison between modelled LOS displacements and the synthetic LOS displacement. X and Y-axis in km

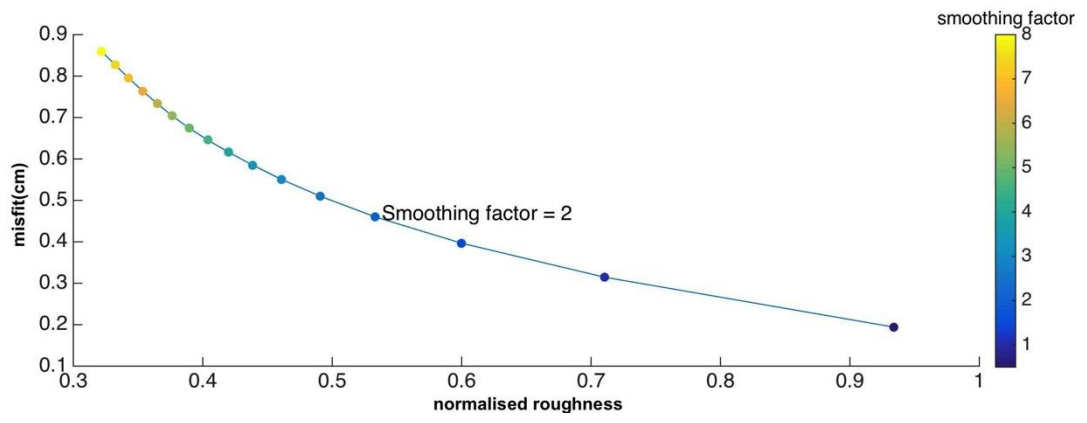


Figure 4.13 Plot of the trade-off curve between slip roughness and data misfit in the synthetic test.





# Chapter 5

## Probing the rheology of continental faults: Decade of postseismic InSAR time series following the 1997 Manyi (Tibet) earthquake

Minxuan Feng<sup>1\*</sup>, Lidong Bie<sup>1</sup>, Andreas Rietbrock<sup>1,2</sup>

<sup>1</sup> School of Environmental Sciences, University of Liverpool, Liverpool, UK, [fm98@liv.ac.uk](mailto:fm98@liv.ac.uk),  
[L.bie@liv.ac.uk](mailto:L.bie@liv.ac.uk)

<sup>2</sup> Geophysical Institute, Karlsruhe Institute of Technology, Karlsruhe, Germany

Geophysical Journal International, 2018, 215(1), 600–613, doi:10.1093/gji/ggy300

### Abstract

The physical processes driving postseismic deformation after large earthquakes are still debated. As in most cases relatively short observation time periods are being used, it is still challenging to distinguish between the different proposed mechanisms and therefore a longer observation time is needed. The 1997  $M_w$  7.6 Manyi, Tibet, earthquake has an excellent InSAR data archive available to study the postseismic deformation up to ~13 years after the earthquake. The coseismic and early postseismic phases of the Manyi earthquake were already investigated in detail by numerous studies with viscoelastic and afterslip models being used to explain the postseismic deformation. We use SAR data obtained from the ERS and Envisat satellites covering the central part of the Manyi fault from 1997 to 2010 to significantly extend the observation period. We test different viscoelastic (uniform

Maxwell, Standard linear solid and Burgers body rheology below an uppermost elastic layer) and afterslip models to assess the most suitable mechanism for postseismic deformation. While a Maxwell rheology (misfit=2.23cm) is not able to explain the observed long time series, the standard linear solid (misfit=2.07cm) and Burgers body models (misfit=2.16cm) with two relaxation times, cannot reproduce sufficiently the localized deformation patterns. The afterslip model (misfit=1.77cm) has the lowest misfit and explains well the temporal and spatial pattern of observed deformation. A combined mechanism model that considers the effects of both afterslip and viscoelastic relaxation is also a feasible process, where the viscoelastic relaxation can slightly improve the fit to the data especially at larger distances from the fault.

## 5.1. Introduction

Various mechanisms are employed to explain postseismic deformations following large earthquakes, including viscoelastic relaxation (e.g. Pollitz *et al.*, 2000), afterslip (e.g. Bürgmann *et al.*, 2002) and poroelastic relaxation (e.g. Jónsson *et al.*, 2003). On the time scale of several years, viscoelastic and afterslip mechanisms are believed to be dominant processes (Wright *et al.*, 2013). A range of rheological models is used to simulate viscoelastic relaxation, such as the Maxwell model (e.g. Ryder *et al.*, 2014), the standard linear solid model (e.g. Ryder *et al.*, 2007) and the bi-viscous Burgers body model (e.g. Pollitz, 2005). There currently exists no single mechanism that can explain all observed deformation after large earthquakes, and this must be evaluated on a case-by-case basis. Even for an individual event, different mechanisms are capable of producing observed surface displacements independently or in combination. For example, afterslip is the only mechanism to explain the 2004 Parkfield earthquake postseismic deformation (Freed, 2007) while afterslip needs to be combined with a viscoelastic model to explain 2001 Kokoxili earthquake (Wen *et al.*, 2012).

Previous studies have mostly focused on a short time span of postseismic deformation, depending on the geodetic observation capability. Only a small number of studies have explored decade-scale or longer post-seismic (e.g. Copley, 2014, Copley and Reynolds, 2014, Hussain *et al.*, 2016, Nishimura and Thatcher, 2003, Ryder *et al.*, 2014, Suito and Freymueller, 2009). It is widely accepted that postseismic motion decays over time, therefore longer observational periods of postseismic deformation can help to distinguish between possible mechanisms. A case study by Pollitz *et al.* (2000) on the Landers earthquake concluded that over 3 years (short time-scale) viscoelastic relaxation in the lower crust/upper mantle is the dominant postseismic process. Over longer time-scales, 7 years, however, a combination of poroelastic relaxation and localized shear deformation is more suitable to explain geodetic data after the Landers earthquake (Fialko, 2004). An alternative is the analysis of 1999 Hector Mine earthquake postseismic deformation by Pollitz (2015), where the influences of afterslip and viscoelastic relaxation at different time scales are discussed.

The  $M_w$  7.6 Manyi earthquake occurred on November 8, 1997, in north-central Tibet. This is a shallow strike slip event as expressed by the CMT solution from the Harvard catalogue (Dziewonski *et al.*, 1981, Ekström *et al.*, 2012). The epicenter is located close to Manyi fault (Figure 5.1), south of the Chaoyang Lake. Satellite geodesy maps clearly rupture of the Manyi earthquake at the surface, spanning a total length of about 170km (Funning *et al.*, 2007, Peltzer *et al.*, 1999). The Manyi fault is a sub-fracture of the Xianshuihe–Ganzi–Yushu fault (e.g. Qidong *et al.*, 2010) that lies on the boundary between Bayan Har terrane and Qiangtang terrane (Figure 5.1). It is located inside the Rola Kangri suture zone, which is the westward extension of Jinsha suture zone. The rate of interseismic slip of the Manyi fault is  $\sim 3\pm 2$  mm/yr, as determined Bell *et al.* (2011), using 5 years of interferograms before the Manyi event.

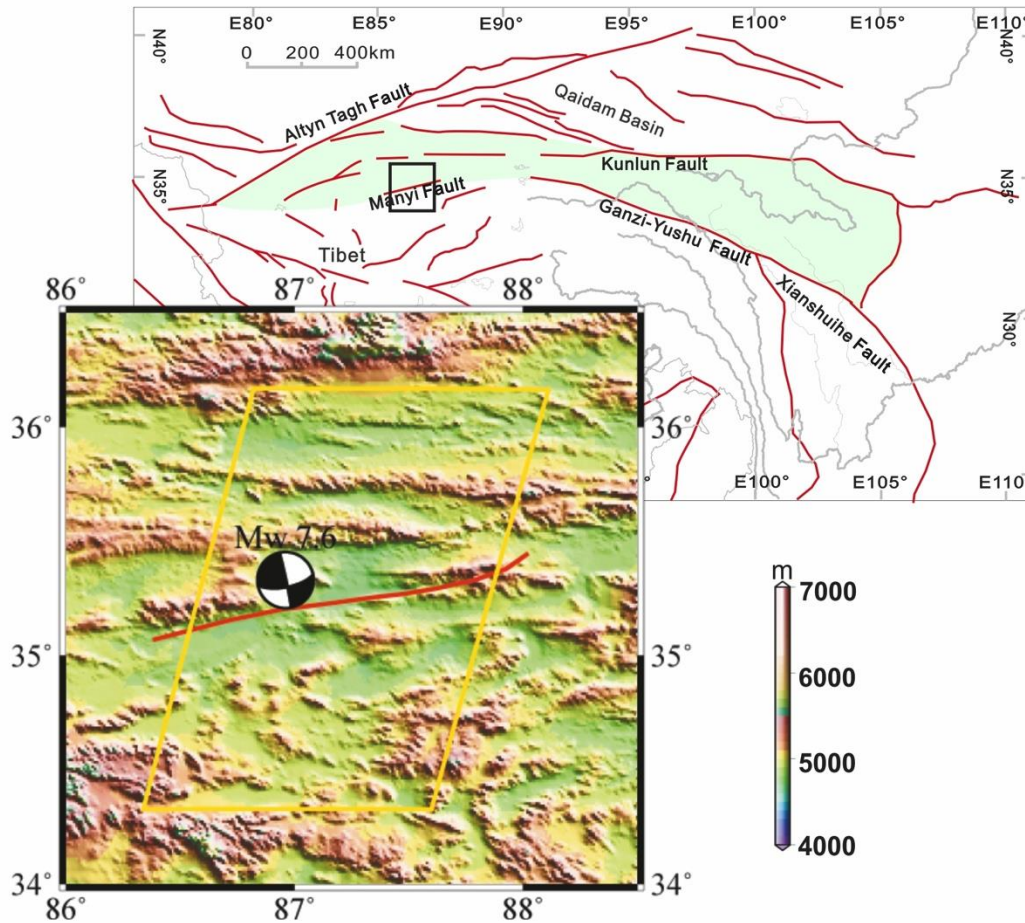


Figure 5.1 Tectonic map (top right) and location map (left). The green block represents the Bayan Har terrane. The Xianshuihe–Ganzi-Yushu fault is the southern boundary of Bayan Har terrane. Left map shows the location of Manyi fault and Manyi earthquake. The Manyi fault is shown in red. The focal mechanism and epicentral location are taken from the GCMT catalogue. The yellow box shows the area covered by SAR images (Track 305), which were used in this study.

Previous studies have documented the early postseismic phases of Manyi earthquake in detail. Ryder *et al.* (2007) found that standard linear solid model and afterslip model could both be used to describe the postseismic deformation. Ryder *et al.* (2011) also reanalyzed the Manyi post-seismic InSAR data using a Burgers body rheology. Yamasaki and Houseman (2012) proposed a complex Maxwell-type model with depth-dependent viscosity. Hetland and Zhang (2014) pointed out that a model composed of a lower Maxwell viscoelastic region with a shear zone beneath the fault could be an alternative mechanism of the postseismic deformation. All results (from all afore mentioned studies) were based on the same dataset, which was compiled by Ryder *et al.* (2007), containing only 4 years postseismic deformation measurements following the Manyi earthquake. A more extended time span of post-seismic

observation is required to investigate the dominant mechanisms at different time scales.

Satellite geodesy can provide us with a high-resolution description of the postseismic surface deformation over a time period of more than 12 years in the Manyi region. Low levels of human activity and vegetation coverage provide an ideal set of conditions for the application of InSAR in the Manyi area. Here, we compile a long timespan InSAR data set covering the central part of the Manyi fault from 1997 to 2010 to analyze time-dependent deformation. Ground deformations are compared with different rheological models to find the best fitting mechanism. We create rate maps, to estimate the deformation rate and then compare this with the interseismic strain accumulation rate (Bell *et al.*, 2011) to assess the current earthquake cycle phase.

## **5. 2. Data Processing and time series**

SAR data were obtained from ERS-2 and Envisat satellites, operating at C-band with a wavelength of 5.6 cm. The incidence angle of ERS and Envisat is about 23 degree. We analyse data over a period between 1997 and 2010 that covers almost the entire length of the Manyi fault (Figure 5.1). Details of the data processing for each satellite are given in Table 5.1. Data were processed using open source software ROI\_PAC developed by Caltech/JPL (Rosen *et al.*, 2004). One descending track (305) was used. Interferograms were formed by pairs of SAR data of which the baseline is smaller than 200m. Most interferograms are constructed by four frames (2871, 2889, 2907, 2925). Topographic effects were removed using a 3-arc-second posting (90 m) digital elevation model, provided by NASA's Shuttle Radar Topography Mission (Farr *et al.*, 2007) and interferograms were flattened before unwrapping.

Table 5.1. Details of Data Used in InSAR Time Series Analysis

| Track | Geometry   | Satellite | Date of First Acquisition<br>yyyymmdd | Date of Last Acquisition<br>yyyymmdd | Number of Dates |
|-------|------------|-----------|---------------------------------------|--------------------------------------|-----------------|
| 305   | Descending | ERS       | 19971202                              | 20011211                             | 7               |
| 305   | Descending | Envisat   | 20031007                              | 20100831                             | 29              |

To minimize the errors, topography-correlated tropospheric delays were removed by using a second-order polynomial representation with respect to elevation. This correction approach is based on an empirical linear relationship between the interferometric tropospheric delay and the topography estimated from data obtained from a non-deforming region (Cavalié *et al.*, 2007). The constant index is estimated from the non-deformed region and then used to calculate the tropospheric delay for the whole interferogram. Finally, the tropospheric delay is subtracted from the raw interferogram. The insufficient or incorrect orbital ramp also needs to be addressed. In theory, the postseismic deformation caused by any given earthquake should decay to zero if the location is sufficiently far from the fault. We masked out the deformation area and implemented the far-field deformation close to zero by quadratic corrections. This trend is further subtracted from the whole interferogram. Figure 5.2a shows the resultant interferogram after all corrections applied reducing the standard deviation from 0.36 to 0.32 cm. The relatively small reduction in standard deviation indicates that the atmospheric noise level of the Manyi area is low, which has been attributed to low vegetation coverage and Plateau subfrigid climate (Ryder *et al.*, 2007, Wright *et al.*, 2004).

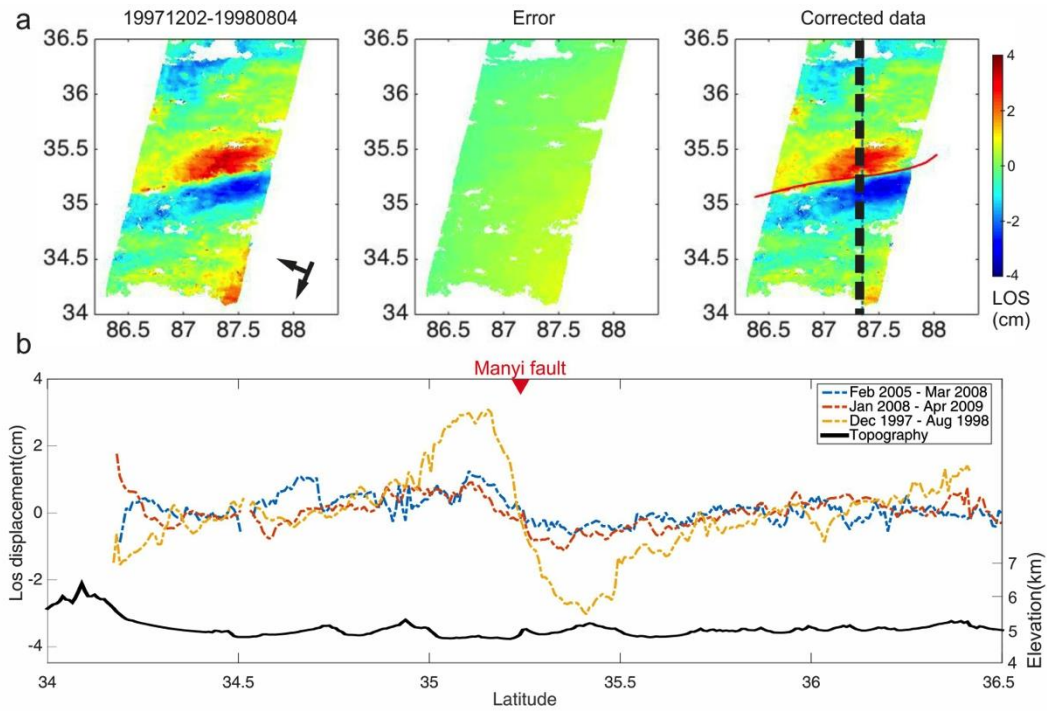


Figure 5.2 (a). An example demonstrating mitigation of atmospheric noise. Panels from left to right show an original interferogram of the Manyi earthquake (19971202-19980804), estimated error, and corrected interferogram. Arrows show the direction of the descending satellite track (SSW) and its corresponding look direction (WNW). Red line is the 11-segment coseismic fault trace as obtained from satellite imagery (Funning *et al.*, 2007). The black dash line indicates the profile location for both topography and interferograms in Figure 5.2b. (b). Profiles of several interferograms, along with the topography (separated onto two scales for clarity). The red triangle shows the location of Manyi fault.

As can be seen in Figure 5.2a, the northern lobes show a positive range change, indicating motions away from the satellite. The southern lobes show the opposite, a negative range change. The distinctive boundary change between these two lobes is consistent with the fault trace. Figure 5.2b shows a cross-section of the topography and the observed postseismic deformation of the Manyi area along a  $0.3^\circ$ -wide swath centred on the profile line for different time steps from early to late. In these profiles, the maximum displacement is at about 10km away from the fault (Figure 5.2b). The LOS amplitude is  $\sim 3$ cm during 1997 to 1998 and decreases to  $\sim 1$ cm during 2005 to 2008. Finally, the LOS amplitude reduces to  $\sim 0.5$ cm during 2008 to 2009. A decreasing rate of deformation is observed. Displacements are still measurable even 10 years after the event. The surface deformations are mainly distributed in close proximity to the fault, indicating a localized deformation pattern.

The InSAR time series is constructed utilizing the Small Baseline Subset algorithm (Berardino *et al.*, 2002) and least squares inversion (Schmidt and Bürgmann, 2003). All images were down-sampled by a factor of 10. Details of the calculation process may be found in Appendix A. Figure 5.3 shows the time series for track 305. A clear and steep displacement gradient across the fault trace is observed and deformation is increasing over time. Moreover, the postseismic deformation seems to have a localized pattern, as the deformations mainly concentrate at a distance of  $\sim 50$  km from the fault.

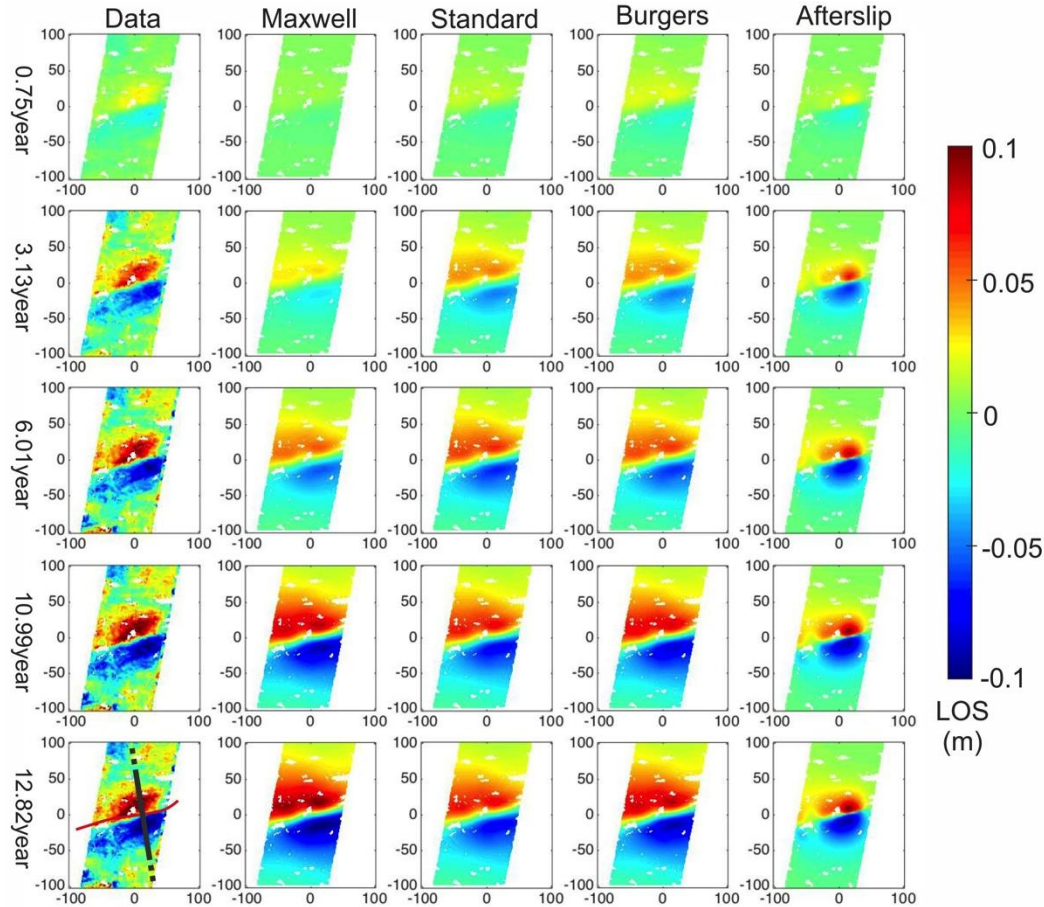


Figure 5.3 Post-seismic time-series and corresponding best fitting modelling results. Here, only 5 dates are presented to show the time series change tendency. The first column is the time series from data; the rest columns are the Maxwell, standard linear solids, Burgers and afterslip. The coordinate axis is in kilometre. In the left bottom subplot, the red line indicates the fault trace; the black bold line indicates the profile location in Figure 5.7 and 5.10.

### 5. 3. Modelling



Using our constructed high spatio-temporal geodetic observations (timespan of 12 years), we explore different proposed mechanisms. Only areas that extend up to 100km at both sides of the fault (region of significant observable deformation) are used in the modelling to minimise the influence of incoherent noise in the deformation signal. Coseismic slip parameters are taken from Funning *et al.* (2007). Misfit is calculated from cumulative LOS displacements for all considered pixels.

$$\chi = \sqrt{\frac{1}{n} (\sum_{i=1}^n [(d_i - m_i)^2])}, \quad (5.1)$$

where  $\chi$  is the misfit,  $n$  is the point number in a single image;  $d_i$  and  $m_i$  are the displacement from data and model prediction for the  $i^{\text{th}}$  pixel. After the misfit for each date is calculated, we evaluate the overall misfit by averaging the cumulative misfits over time.

### 5.3.1 Viscoelastic modelling

Here we assume that the stress impulse caused by the earthquake will be relaxed by viscous flow within the viscoelastic lower crust. The viscosity controls the stress relaxation time. In this study, we mainly consider three viscoelastic rheologies: the Maxwell, standard linear solid and Burgers body. A schematic configuration depicting different rheologies is shown in Table 5.2. The elastic spring responds to immediate stress loading, and the damper dominates the steady-state strain rate.

The Earth model is constructed using an elastic layer overlying a viscoelastic medium. The crustal thickness is  $65 \pm 5$  km beneath the central Tibet from Magnetotelluric data (Zhao *et al.*, 2001). Jiang *et al.* (2006) estimate the crustal thickness of Bayan Har terrane is on the order of 70 km. Therefore we chose the base of the crust at 70 km for this study. The upper crust thickness varies from 10 to 25km through the Tibet Plateau Zhao *et al.* (2001). In this study, the elastic layer is fixed to a depth of 15 km as most coseismic slip occurs above this depth (Ryder *et al.*, 2007). The rheology of the viscoelastic layer is changed according to different model

features. An open-source software package VISCO1D (Pollitz, 1997) was used to model viscoelastic deformation.

Before modelling the postseismic deformation, it is helpful to explore the sensitivity of different rheological model parameters on the surface deformation. We run forward calculations for the Maxwell, standard linear solid and Burgers body models while only varying one parameter at a time to examine the effect on the predicted surface deformation. We are most interested in the mean displacements in the observation area and the decay time of the transient phase. We show mean displacement as a function of time since the earthquake (Figure 5.5). For simplicity, we use the fault geometry of the Manyi earthquake (strike, dip, length etc. from Funning *et al.* 2007) in this parameter sensitivity test.

The Maxwell analogue is composed of a spring with shear modulus  $\mu_e$  and a viscous damper with viscosity  $\eta$  in series (see Table 5.2) and has a single relaxation time  $\tau = \frac{\eta}{\mu_e}$ . The Burgers body model is represented by a Kelvin element in series with a Maxwell element (see Table 5.2). This configuration has two relaxation times due to two viscous components. The standard linear solid model is an extreme case of the Burgers body model for which the Maxwell viscosity ( $\eta_m$ ) becomes infinite. When  $\eta_m$  increase to  $1 \times 10^{21}$  Pa s or larger, the Burger modelling result are nearly equal to the standard linear model in our test. The steady-state viscosity  $\eta_m$  controls the magnitude of displacement because the Burgers body model is more sensitive to Maxwell viscosity (Ryder *et al.*, 2011). Details of the parameter range explored for each viscoelastic model (shear modulus and viscosity) are given in Appendix B.

In our study, the elastic modulus  $\mu_e$  is assumed at  $3 \times 10^{10}$  Pa and the Maxwell viscosity ( $\eta_m$ ) is taken in the range of  $10^{18}$  -  $10^{20}$  Pa s for all viscoelastic models. In the Burger model, the ratio between optimal long-term  $\mu' = \mu_k \mu_e / (\mu_k + \mu_e)$  to the Maxwell shear modulus ( $\mu_e$ ) is close to 2:3 (Ryder *et al.*, 2011), thus  $\mu_k$  is fixed at  $6 \times 10^{10}$  Pa. In the standard linear model,  $\mu_k$  is fixed at  $2 \times 10^{10}$  Pa according to Ryder *et al.* (2007).

Among these viscoelastic models, the standard linear solid modelling yields the lowest misfit of 2.07cm with a viscosity of  $3 \times 10^{18}$ Pa s. The misfits of the Maxwell and Burgers body models are 2.23cm and 2.16cm respectively. The best fitting parameters for each model and corresponding misfits for the entire time-series are summarized in Table 2.

Table 5.2 Best-fitting viscosities and misfits for each model

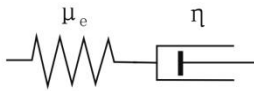
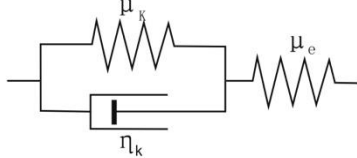
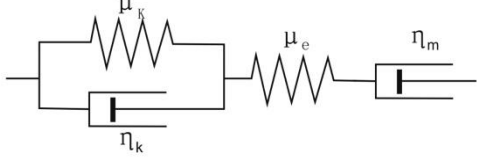
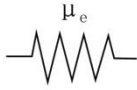
| Model name            | Model schematic   | Best fit parameters  | Misfit (cm) |
|-----------------------|---|--|-------------|
| Maxwell               |    | $\eta = 7 \times 10^{18}$ Pa s<br>$\mu_e = 3 \times 10^{10}$ Pa  | 2.23        |
| Standard linear solid |   | $\eta = 3 \times 10^{18}$ Pa s<br>$\mu_e = 3 \times 10^{10}$ Pa<br>$\mu_k = 2 \times 10^{10}$ Pa                                       | 2.07        |
| Burgers body          |  | $\eta_k = 2 \times 10^{18}$ Pa s<br>$\eta_m = 1 \times 10^{19}$ Pa s<br>$\mu_e = 3 \times 10^{10}$ Pa<br>$\mu_k = 6 \times 10^{10}$ Pa | 2.16        |
| Afterslip             |  | $\mu_e = 3 \times 10^{10}$ Pa  | 1.77        |

Figure 5.3 shows predicted interferograms for all models. The predicted interferograms of the three models indicate a similar pattern of deformation. The positive lobe widens to east on the southern side of the fault while the negative lobe widens to west on the northern side of the fault. They fit the observed measurement well during the early postseismic phase. However, the predicted interferograms indicate that the modeled deformation lobes diffuse farther away and have larger amplitudes at larger distances than the  $\mu_e$  data. This difference increases with time. The deformation lobes shown by InSAR observations are concentrated around the fault, while the model produces notable far-field deformation.

### 5.3.2 Afterslip modelling

Here we assume that the observed surface deformation is caused by afterslip on the fault plane and its extension. We utilize surface deformation to retrieve slip distribution along the fault plane. The inversion is processed independently at each successive time window such that they are consistent with the time series data. In our afterslip modelling, the Earth is supposed to be an elastic half-space with no rheological layering. The shear modulus for the half-space is taken as  $\mu = 3.0 \times 10^{10}$  Pa. The fault plane geometry is taken from coseismic interferograms produced by Funning *et al.* (2007). The slip depth is allowed to extend to 60 km during the inversion. The fault plane is discretized into an array of rectangular patches (4 km x 4 km) down-dip resulting in a total of 705 patches. The Green's function approach is employed.  $\mathbf{G}$  is a unit model slip, which is estimated by using the Okada formula (Okada, 1985). A least squares algorithm is used for every pixel at successive dates using the following equation (Jónsson *et al.*, 2002):

$$\begin{bmatrix} \mathbf{G} \\ \kappa^2 \nabla^2 \end{bmatrix} [\mathbf{m}] = \begin{bmatrix} \mathbf{d} \\ \mathbf{0} \end{bmatrix}, \quad (5.2)$$

where  $\mathbf{d}$  is the LOS displacement of data,  $\mathbf{m}$  is the model solution,  $\nabla^2$  is a second order Laplacian smoothing operator and  $\kappa^2$  is a smoothing factor. The smoothing factor  $\kappa^2$  is determined by looking at the 'knee' of the curve (misfit vs roughness) (Jónsson *et al.*, 2002). The knee of the curve represents the point of the optimal trade-off between roughness and misfit.

The time-dependent postseismic slip distributions are shown in Figure 5.4. The slip pattern is very stable through time even though the amount of slip is increasing over time. The high-slip patches ( $>0.5$  m) concentrate at a depth of 8–40 km, which we will call the creeping segment of the fault. The patches with the highest slip for both coseismic and postseismic deformation are located along the centre of Manyi fault. The afterslip is located deeper than the coseismic slip. After 12 years deformation, the

maximum afterslip is 1.23 m at a depth of 15~20 km and the moment release is  $\sim 5.96 \times 10^{19}$  N m (equivalent to a single event of  $M_w$  7.1), approximately 25 percent of the coseismic moment.

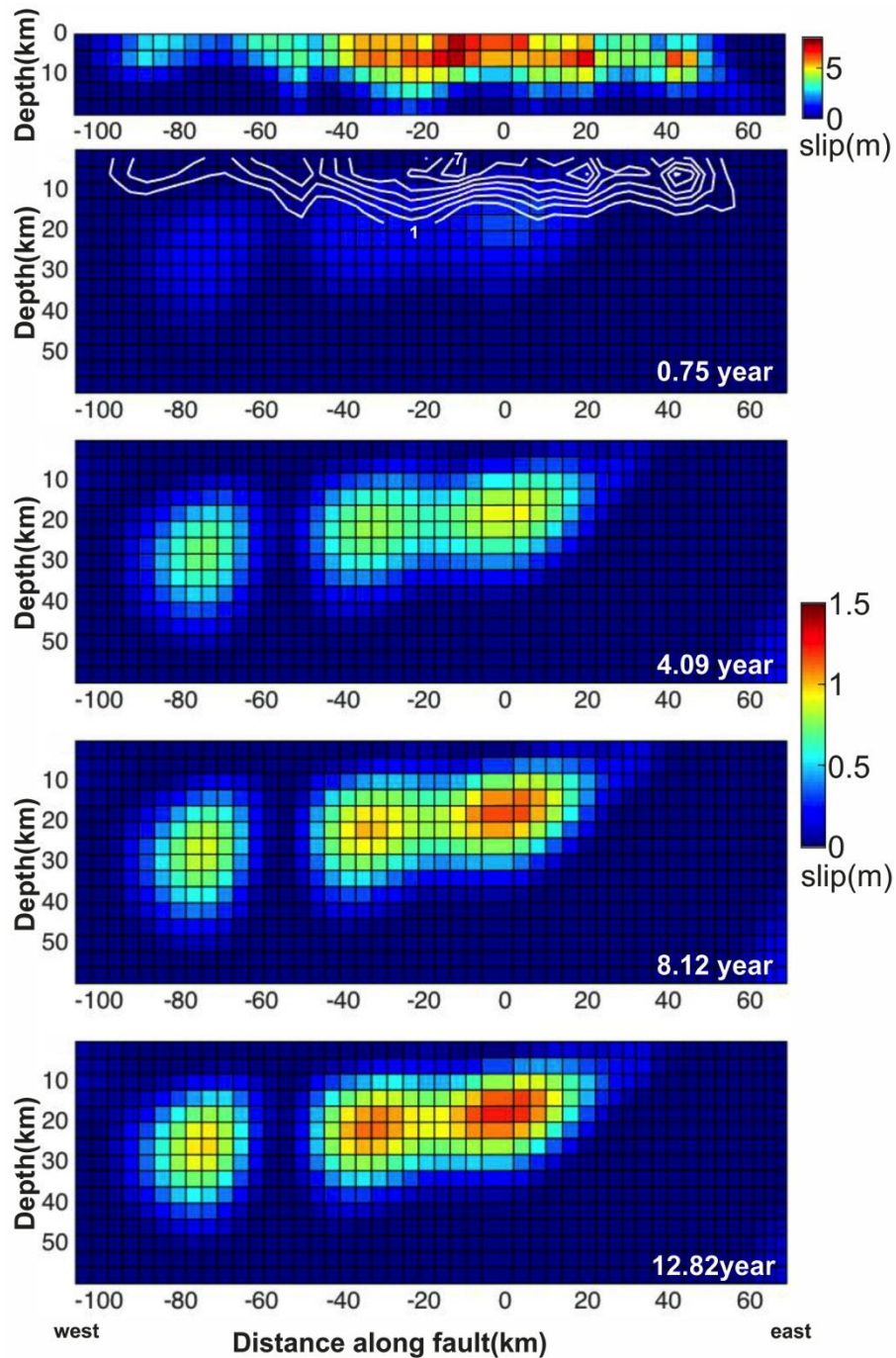


Figure 5.4 Postseismic slip distributions from afterslip inversions. Fault segments are shown as a single plane and view is from the south. The top is the coseismic slip distribution from Funning *et al.* (2007). Postseismic slip distributions are shown beneath. The contour line shows coseismic slip extraction. The gradient of slip contour is 1m.

Predicted interferograms of our afterslip model show a spatially localized deformation pattern, which is very similar to the measured interferograms (Figure 5.3). The misfit is  $\sim 1.77\text{cm}$ , 15% lower than the viscoelastic models. The residual distribution ranges are smaller relative to viscoelastic models and describe better the spatial deformation pattern farther away from the fault.

## **5.4. Discussion**

### **5.4.1 Limitations of viscoelastic modelling**

To demonstrate the temporal variations in the observed surface displacements, and how well the different models capture rapid decay, the data temporal decay curves are plotted by mean LOS displacements over all pixels on the ground (Figure 5.5). The Maxwell model underestimates the displacement takes place during early phase deformation and gives an overestimation in the later period thus it demonstrates a rather poor fit to the data curves. The Burgers body and standard linear solid capture the features of fast decay better than the Maxwell model. However, the Burgers body model matches the displacement merely in the first several years and standard linear solid model better captures the latter stage of the displacement evolution. It seems, therefore, that the standard linear model can match the temporal behavior of the overall surface deformation. The key point of the viscoelastic modelling results is that the observed deformation requires two relaxation times, a transient deformation period followed by a steady-state period.

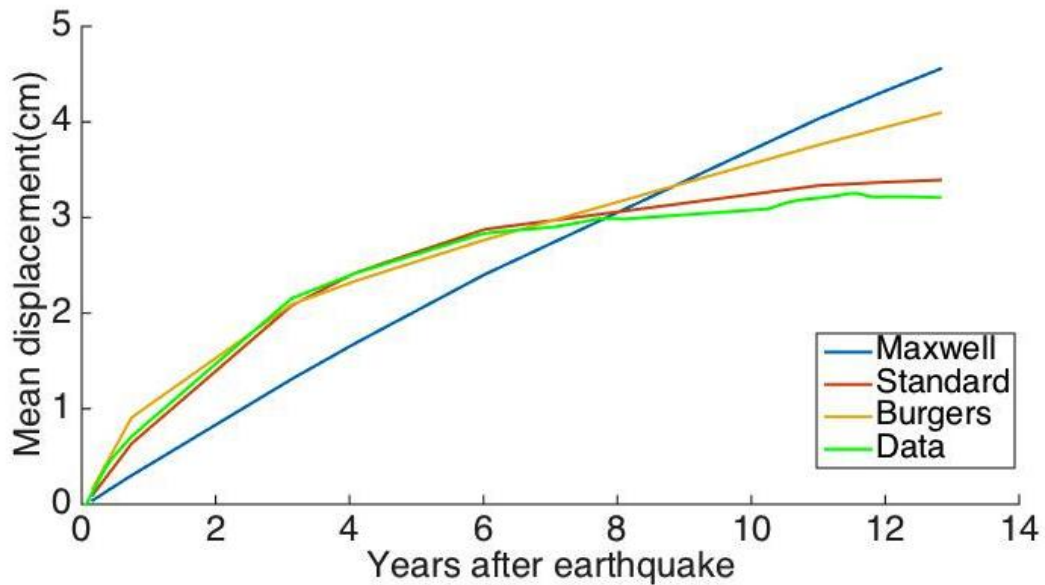


Figure 5.5 Mean displacements against time after the Manyi earthquake. The green line is obtained from the data. The rest curves are obtained from the overall best fitting parameters of each viscoelastic model. All pixels in the interferogram are taken into account.

When we look at the spatial pattern of the modelling, we find that viscoelastic modelling cannot reproduce a similar spatial pattern as can be seen in the data. The predicted interferograms of the viscoelastic modelling do not show a localized pattern (Figure 5.3). As the distributions diffuse into the far field, the residuals tend to increase (Figure S5.1). To better explore the temporal behavior of each model, we choose four patches to calculate the mean displacement separately (Figure 5.6). The locations of these patches are shown in Figure S5.1, where the residual is relatively small for each model (Figure S5.1). The Maxwell model still fits poorly to the data curves. In patch A and B, all viscoelastic models underestimate the deformation. In patch C, the standard linear solid model and Burgers body model are closer to the data but still give underestimations. In patch D, all viscoelastic models overestimate the data displacement. Figure 5.7 shows the displacements along an NW-SE profile that crosses the central part of the fault for the above modelling. Displacements are shown for average displacements of pixels within 5 km of the profile line. Viscoelastic models always underestimate displacement along the center of the fault and overestimate at the far field. They do not reproduce the abrupt transition from the crest to the trough of the data displacement profiles. In addition, their amplitudes are lower

and wavelengths are broader when compared to the data. Based on these results, single viscoelastic models are inconsistent with the observed postseismic deformation obtained from the InSAR data of the Manyi earthquake.

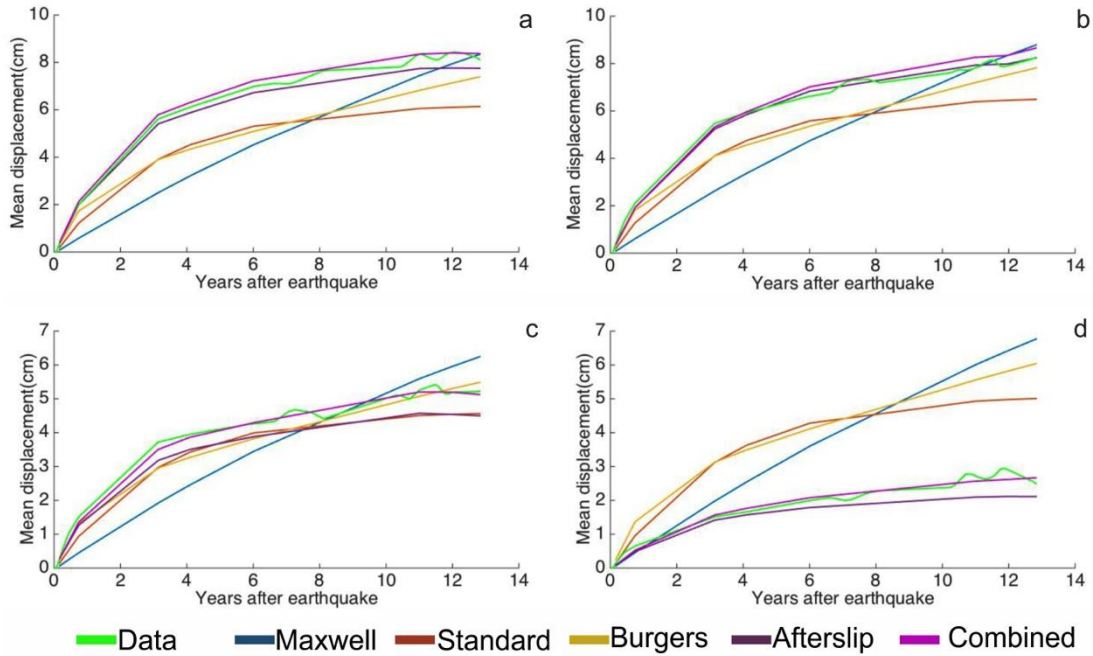


Figure 5.6 Evolution of the mean displacements of patches A, B, C and D, after the Manyi earthquake. The location of each patch is showed in Figure S5.1. Subplot a, b c and d represent patch A, B, C and D respectively. The green line is obtained from the data. The rest curves are derived from the overall best fitting parameters of each viscoelastic model. Combined model has 30km thick elastic lid over a half-space with viscosity  $5 \times 10^{19}$  Pa s.



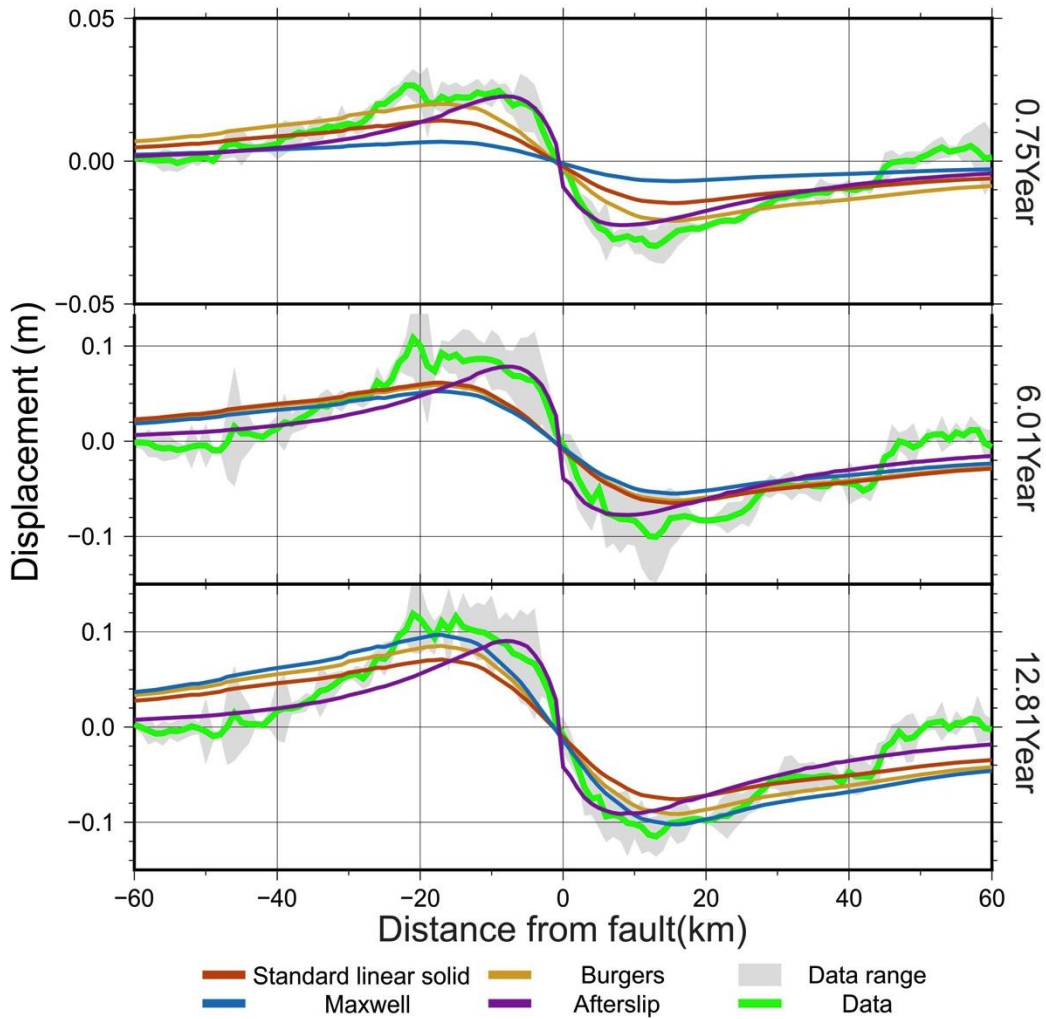


Figure 5.7 Swath profile across the fault for each model from early to late time. The width of the profile is 5 km. The profile location is shown in Figure 5.3. The grey bar is the range value of the data profile. The bold black line is the average value of the data profile. In the middle picture, the curves of the viscoelastic models almost overlap.

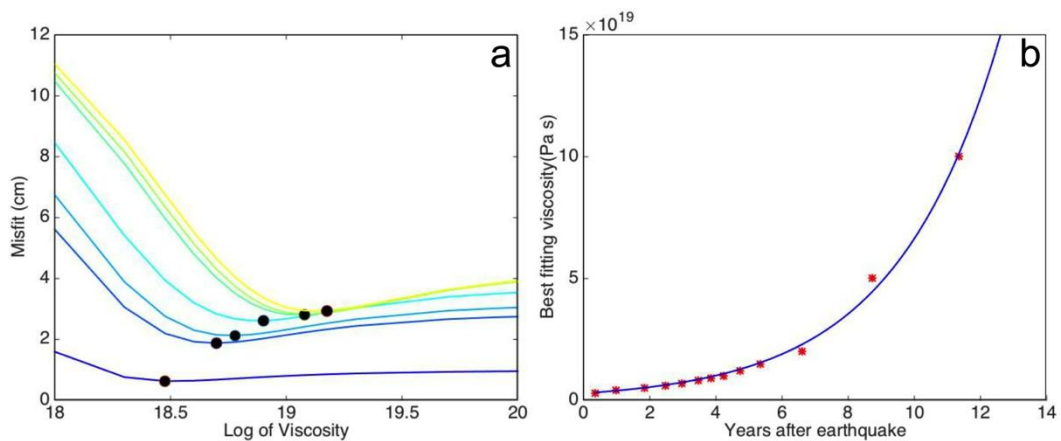


Figure 5.8 (a) Misfit as a function of viscosity. The color gradient from blue to yellow represents time from early to late. The black dots indicate the minimum misfit. (b) Best fitting viscosity for each time interval deformation. The red dot represents the viscosity required by the deformation between each time window. The deformation rate between each time interval becomes smaller and smaller over time, there needs larger viscosity to meet the micro change between each time interval.

The misfit of the Maxwell modelling is plotted as a function of viscosity (Figure 5.8a). This shows that low viscosities are required to explain transient early deformations, while higher viscosities are necessary to explain sustained slow motion. To be able to model the spatial-temporal change of postseismic deformation, we test a time-dependent viscosity. By assuming an exponential increase in viscosity we reduce the observed difference in each time interval (Figure 5.8b). After 20 years, the viscosity increases to  $5 \times 10^{21}$  Pa s, which reaches the upper bound of the observed range between  $10^{19}$  to  $10^{21}$  Pa s (Hilley *et al.*, 2005). We use the viscosities determined by the cumulative deformation (dots in Figure 5.8a) to calculate the possibility of time-dependent viscosity model. The misfit reduces from 2.23cm of uniform viscosity model to 2cm in the time-dependent viscosity model. Time-dependent viscosity could be a possible explanation for the postseismic deformation although the misfit reduction of such a time variable model is only 10%. Such a time dependent effective viscosity might be a proxy for a power-law rheology. However, the predict LOS displacement spatial pattern of the power-law mismatch with the data deformation (Figure S5.2), which indicates that the dominant physical mechanism is not likely to be nonlinear deformation. So we do not explore this possibility here.

#### **5.4.2 Applicability of afterslip modelling**

The afterslip model misfit is at least 15% lower than the viscoelastic models and is therefore also lower than the time variable rheology model. The predicted localized spatial pattern of the afterslip model gives more satisfactory reproduction of the data (Figure 5.3, Figure S5.1). The temporal shape of the afterslip model better agrees with the data than the viscoelastic models, both for our four patches (Figure 5.6) and with regard to the profiles (Figure 5.7). We therefore conclude that the afterslip model is consistent with the observed postseismic deformation.

Taking into account the degrees of freedom, it might not be surprising that the afterslip model performs better than the viscoelastic models as more model

parameters are available to describe the complex spatial and temporal behavior. As a result of this, we test a simplified afterslip model, which contains only the three major patches of the slip area (Figure S5.3a). Also this simplified model can reproduce the localized deformation pattern (Figure S5.3b). The amplitude of the predicted surface deformation is similar to the real data (Figure S5.3c). This test shows that the decrease in misfit of the afterslip model is not attributable to the increase in available model parameter but generally explains better the observed data.

Afterslip has been identified in the decades following an earthquake for several events (e.g. Copley, 2014, Copley and Reynolds, 2014, Hussain *et al.*, 2016). The observed afterslip can last a minimum of 40 years following the 1964 Alaska earthquake (Suito and Freymueller, 2009). Also, afterslip is still taking place from the 1999 Izmit earthquake at an average rate of  $\sim 6$  mm/year (Cakir *et al.*, 2017). These studies suggest that the timescale of afterslip for the Manyi earthquakes is not unique. Ingleby and Wright (2017) suggest that a rate-and-state frictional afterslip model can be consistent with decades of near-field observation results. Therefore, based on our modelling results, as well as residuals and profiles, we inferred that the afterslip model is the single dominant mechanism involved in postseismic displacements in the near field. However, we cannot rule out the possibility that the more complicated models, such as a combination of viscoelastic and afterslip or nonlinear models, can explain the data and will be explored in the following.

### **5.4.3 Combined afterslip and viscoelastic modelling**

Several studies have shown that combined mechanism models can explain postseismic displacement by combining afterslip and viscoelastic relaxation (e.g. Biggs *et al.*, 2009, Johnson *et al.*, 2009). Therefore, we construct a combined model that considers the effects of both afterslip and viscoelastic relaxation. A true joint model should consider the afterslip and viscoelastic relaxation simultaneously and might require less afterslip and more viscoelastic relaxation at deeper depth. Here, we explore the possibility of one end-member scenario, where after-slip dominates

postseismic deformation, and the residual surface deformation can be modelled with viscoelastic relaxation instead of the optimal parameters of these two processes. The elastic and viscoelastic domains have the same elastic properties.

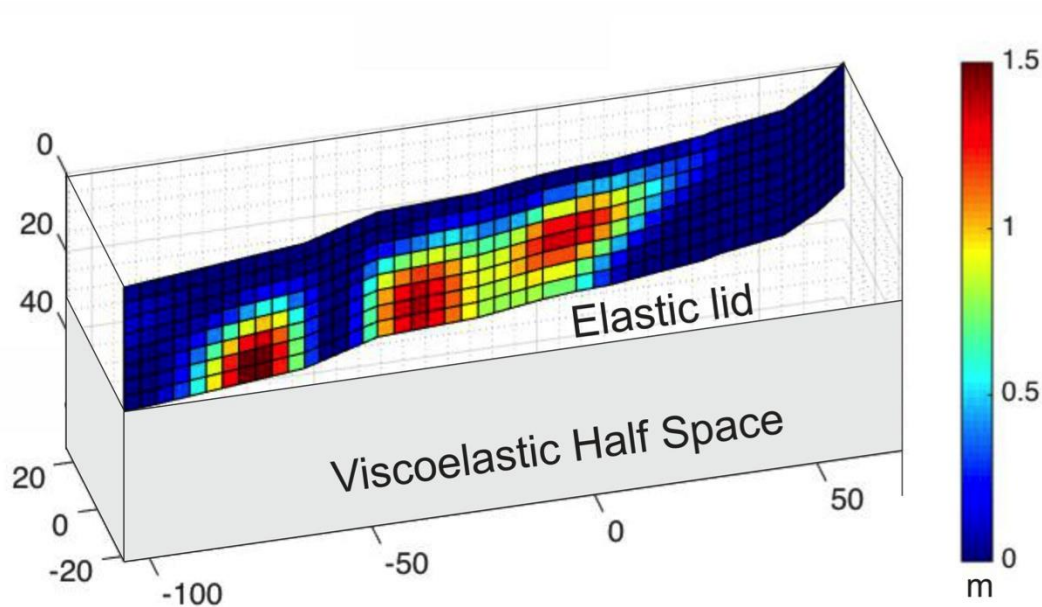


Figure 5.9 The sketch map of combined mechanism model. The viscoelastic relaxation has an elastic layer thickness of 30 km over a half-space with viscosity  $5 \times 10^{19}$  Pa s.

As the afterslip can interpret most surface deformation, we take afterslip as the main mechanism. The displacements caused by afterslip are, as in the previous inversion, removed from the LOS displacement. A linear forward viscoelastic modelling below an elastic lid is subsequently calculated using VISCO1D to find any additional viscoelastic relaxation in the crust and mantle (Figure 5.9). In these cases, any observed LOS displacements, which are not reproduced by the afterslip model, can be attributed to viscoelastic relaxation (hereafter referred to as residual viscosity). Four values of the thickness of the elastic lid including 15km (upper crust thickness), 30km, 45km (the middle crustal thickness) and 70 km (the lower crustal thickness) are used. The tradeoff curve between misfit and viscosity determines the best fitting residual viscosity (Figure S5.4). The lower misfits are found for higher viscosity in these cases and  $5 \times 10^{19}$  Pa s is the lower bound of the viscosity. For the residual viscosity of  $5 \times 10^{19}$  Pa s, the corresponding misfits are 1.85cm 1.72 cm, 1.77cm and

1.76cm respectively for the 4 different elastic lid thickness model. From the four patches of 30km elastic lid model (Figure 5.6), we can see that each mean displacement has a similar shape to the afterslip model while there is some improvement in fitting the data. The far-field patch D illustrates a great improvement. The viscoelastic mechanism reproduces some far-field deformation in the combined model, which is complementary to afterslip model.

The afterslip and combined mechanism model have similar misfits and reproduce very similar spatial patterns of surface displacement. In both mechanisms, the afterslip process reproduces the largest part of the surface deformation. The viscoelastic relaxation slightly improves the fit to the data especially at larger distances from the fault. Therefore a combination of afterslip and viscoelastic relaxation is also a feasible process.

#### **5.4.4 Rate of late postseismic deformation**

To further explore postseismic deformation, we stacked interferograms from 2008 to 2010. This method adds  $N$  independent interferograms together and averaging them to reduce the spatially uncorrelated noise by  $1/\sqrt{N}$  (Biggs *et al.*, 2007). This method has been used to calculate interseismic strain accumulation in many places, e.g. Turkey (Wright *et al.*, 2001), California (Lyons and Sandwell, 2003) and Tibet (Wright *et al.*, 2004). From the stack, we can see that the Manyi fault is still moving, at a maximum motion rate of  $\sim 5$ mm/yr near the fault zone. To illustrate the rate map more clearly, we extracted a swath profile across the central fault (Figure 5.10). Average LOS velocities inferred from the central profile of the stacked InSAR data give an initial impression of a change in velocity. The average LOS velocity close to the fault is  $\sim 4$ mm/yr, twice the far-field LOS velocity. The LOS velocity profile appears to approximate an arctangent sigmoid trend although the velocity does not increase with distance from the fault. The horizontal, fault-parallel velocities is approximately  $\sim 12$ mm/yr, taking into account the line of sight incidence angle  $\sim 23^\circ$

of the scene. The Bell *et al.* (2011) calculated the interseismic motion rate of the Manyi fault to be 1 mm/yr prior to the earthquake. Through the alluvial terrace that was formed after the Holocene, horizontal sinistral slip on the Manyi fault is at a rate of 4mm/yr (Xu, 2000). For our current InSAR dataset, these studies suggest that the postseismic deformation of the Manyi earthquake is still continuing.

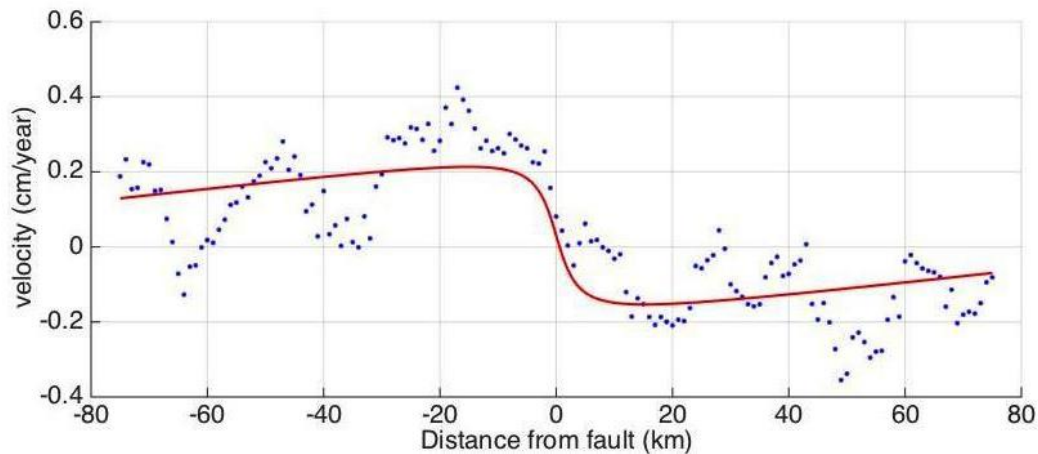


Figure 5.10 Profile across the InSAR LOS rate map. Averaged LOS rate (vertical axis) is plotted according against the distance (horizontal axis) from the fault. The profile location is the same as shown in Figure 5.3. Point measurements are taken within the 10-km-wide band along the profile. The red line represents the best fitting curve for the data.

## 5.5. Conclusion

Following the 1997  $M_w$  7.6 Manyi earthquake, InSAR analysis provides insight into the relatively long timescale of postseismic deformation. We have investigated four possible mechanisms: the Maxwell, standard linear solid, Burgers body viscoelastic models, and the afterslip model. All the viscoelastic models are constructed using an elastic layer overlying the uniform viscoelastic properties. The Maxwell model (misfit=2.23cm) does not fit the data and although the standard linear solid (misfit=2.07cm) and Burgers body (misfit=2.16cm) models have two relaxation times, they cannot match the observed temporal-spatial deformation patterns. For the mean deformation over all pixels they have good temporal reproduction, but for the spatial distribution they cannot fit the data. Additionally, a time-dependent viscosity model reduces the misfit to 2cm, which provides a possible explanation for the

deformation. The afterslip model has the smallest misfit of 1.77cm and can better match the spatio-temporal behaviour of the surface deformation. The maximum afterslip is 1.23 m twelve years after the earthquake. We also explored the possibility of combined mechanisms where both afterslip and viscoelastic relaxation contribute to the postseismic deformation. For this case the misfit (1.72cm) slightly decreases.

## Data

Time series data (data used in Equation 1) is available in supplementary material.

## Appendix A: Time series construction

A set of  $N$  interferograms are constructed using  $S$  independent SAR acquisitions. Let  $\mathbf{t}$  be the vector of SAR acquisitions ordered by date. For a given interferogram, the data range between the start time  $t_k$  and end time  $t_{k+1}$ :  $m_{ab}$  can be written as:

$$m_{ab} = \sum_{k=a}^{b-1} v_{k,k+1} (t_{k+1} - t_k), \quad (\text{A5.1})$$

where the index  $k$  is the serial number of the date in acquisition matrix  $\mathbf{t}$ , and  $v_{k,k+1}$  is the velocity between time  $t_k$  and  $t_{k+1}$ . The date immediately following the earthquake is taken as the reference time for all interferograms. This ensures that all deformation is measured relative to a common date. We calculate the range change by summing up the incremental range changes from preceding time steps. The entire dataset can be written as follows:

$$\mathbf{T}\mathbf{v} = \mathbf{r}, \quad (\text{A5.2})$$

where  $\mathbf{T}$  is a  $N \times (S-1)$  matrix of time reference interval,  $\mathbf{v}$  is a  $(S-1) \times 1$  vector of successive velocities between two adjacent acquisitions and  $\mathbf{r}$  is a vector containing displacement measurements. To avoid significant discontinuities we used velocity instead of displacement during the inversion (Berardino *et al.*, 2002).

A smoothing constraint was used to reduce the effect of atmospheric noise. It assumes that less deformation occurs over short time intervals. The smoothing constraint is written as:

$$\mathbf{T}^s \mathbf{v} = \mathbf{0}, \quad (\text{A5.3})$$

where  $\mathbf{0}$  is a  $(S - 2)$  column vector of zeros.  $\mathbf{T}^s$  is a  $(S - 2)$  by  $(S - 1)$  matrix which has the following form:

$$\begin{cases} \mathbf{T}_{jj}^s = -\mathbf{1} \\ \mathbf{T}_{j,j+1}^s = +\mathbf{1} \end{cases} \quad (\text{A5.4})$$

Temporal velocity evolution is obtained by solving the following equation:

$$\begin{bmatrix} \mathbf{T} \\ \gamma \mathbf{T}^s \end{bmatrix} [\mathbf{v}] = \begin{bmatrix} \mathbf{r} \\ \mathbf{0} \end{bmatrix} \quad (\text{A5.5})$$

If the smoothing factor  $\gamma$  is too large, the deformation signal will be over-damped. On the other hand, if the smoothing factor  $\gamma$  is too small, there will be significant fluctuation from time step to time step. We chose the optimal smoothing factor by considering the trade-off between model fit (misfit) and model roughness. Choosing a value at the ‘knee’ of the curve for the smoothing factor we obtain  $\gamma = 0.5$  (Figure A5.1). Adjacent values of the smoothing factor do not show significant differences in the constructed time series result.



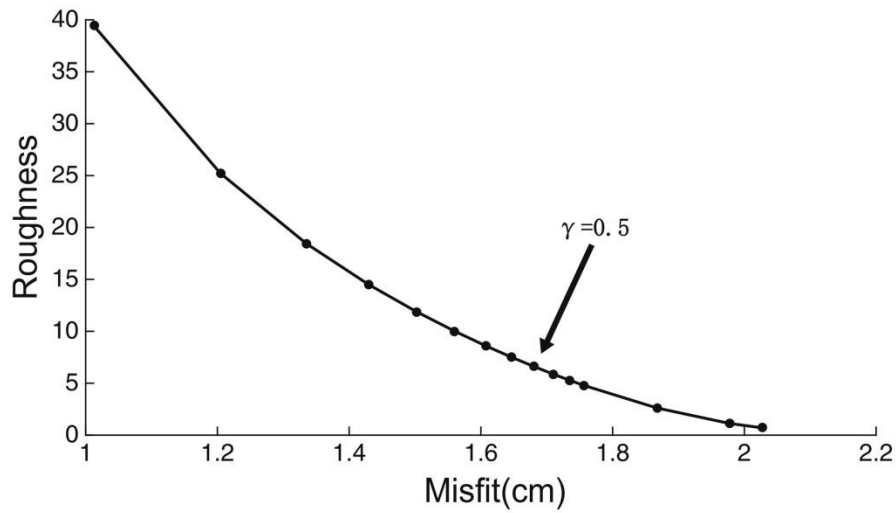


Figure A5.1 Roughness plotted against misfit for different smoothing factors in the time-series matrix. The point marks the smoothing factor ( $\gamma$ ) of 0.5, which is used in this study.

Once we have velocities from the least-square solution, the overall displacement was calculated from the successive velocities. For the very early phase, namely the first month, transient deformation is approximately linear (Ryder *et al.*, 2007), so the velocity can be extrapolated to the time of the earthquake itself.

## Appendix B. Model set-up

The Maxwell analogue is composed of a spring with shear modulus  $\mu_e$  and a viscous damper with viscosity  $\eta$  in series and has a single relaxation time  $\tau = \frac{\eta}{\mu_e}$ . If we keep the viscosity ( $\eta$ ) fixed and vary the shear modulus ( $\mu_e$ ), the relaxation time ( $\tau$ ) will decrease as shear modulus increase (Figure A5.2a). While increasing the half-space viscosity ( $\eta$ ) and keeping the shear modulus ( $\mu_e$ ) at constant, the relaxation time ( $\tau$ ) of the transient process will also increase (Figure A5.2b). In our study, the elastic modulus  $\mu_e$  is assumed at  $3 \times 10^{10}$  Pa (in line with previous studies) and the viscosity is taken in the range of  $10^{18}$  -  $10^{20}$  Pa s.

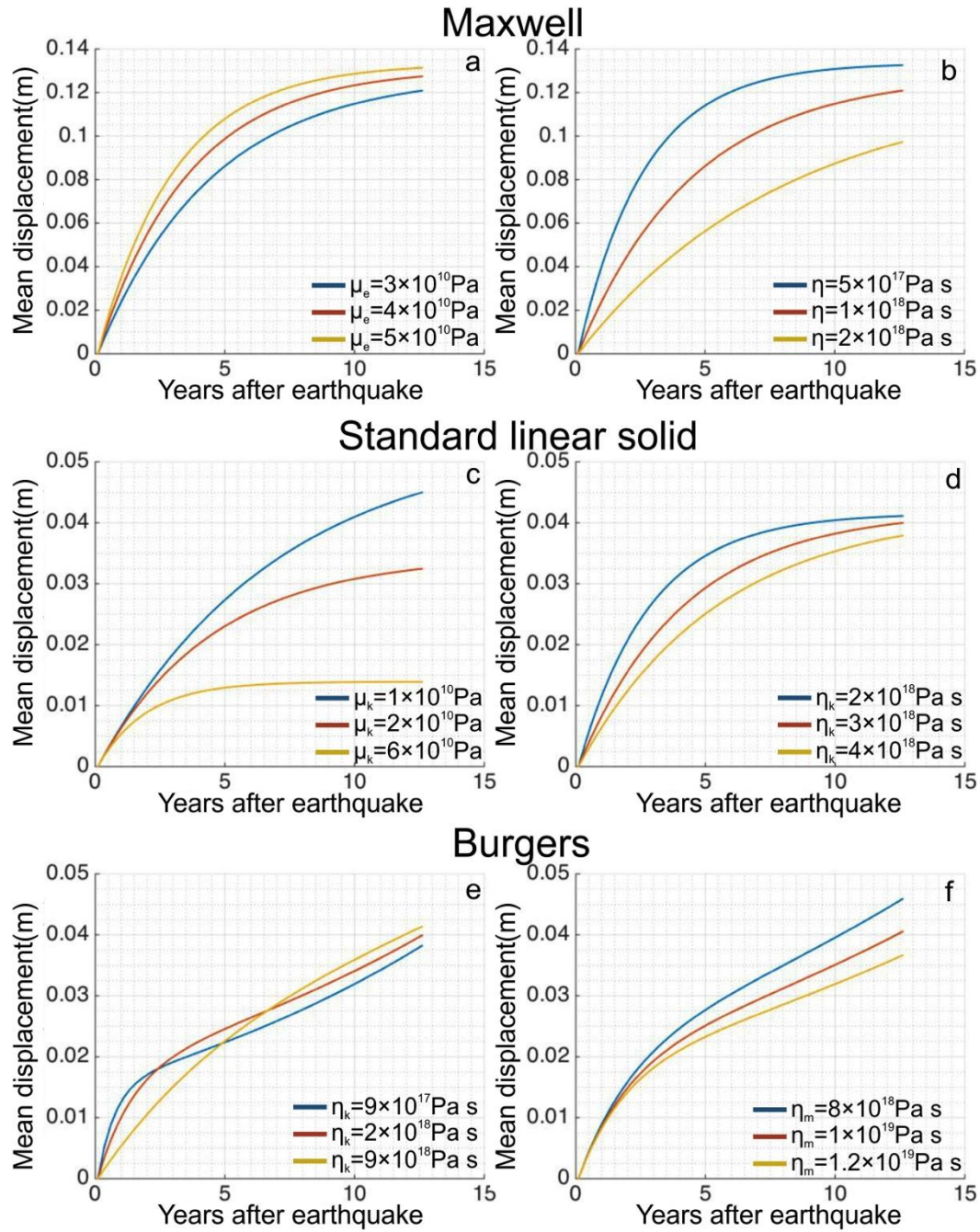


Figure A5.2 Mean displacements predicted by different viscoelastic models with various rheological model parameters. (a) Maxwell model,  $\eta=10^{18} \text{ Pa s}$ , varying  $\mu_e$ . (b) Maxwell model,  $\mu_e=3 \times 10^{10} \text{ Pa}$ , varying  $\eta$ . (c) Standard linear solid model,  $\mu_e=3 \times 10^{10} \text{ Pa}$ ,  $\eta_k=4 \times 10^{18} \text{ Pa s}$ , varying  $\mu_k$ . (d) Standard linear solid model,  $\mu_e=3 \times 10^{10} \text{ Pa}$ ,  $\mu_k=1.5 \times 10^{10} \text{ Pa}$ , varying  $\eta_k$ . (e) Burgers body model,  $\mu_e=3 \times 10^{10} \text{ Pa}$ ,  $\mu_k=6 \times 10^{10} \text{ Pa}$ ,  $\eta_m=1 \times 10^{19} \text{ Pa s}$ , varying  $\eta_k$ . (f) Burgers body model,  $\mu_e=3 \times 10^{10} \text{ Pa}$ ,  $\mu_k=6 \times 10^{10} \text{ Pa}$ ,  $\eta_k=3 \times 10^{18} \text{ Pa}$  varying  $\eta_m$ .

The standard linear solid model is conceptually composed of a Kelvin element in series with a spring with shear modulus  $\mu_e$ . The Kelvin element consists of an elastic

component with shear modulus  $\mu_k$  in parallel with a viscous component with viscosity  $\eta_k$ . It is the simplest element that can describe both delayed elasticity and stress relaxation. The system is initially governed by shear modulus  $\mu_e$ , and then falls to long-term shear modulus  $\mu' = \mu_k\mu_e/(\mu_k+\mu_e)$  as stress relax. Keeping the viscosity ( $\eta_k$ ) and shear modulus ( $\mu_e$ ) fixed, we find that both displacement magnitude and the time of the transient will increase with the decrease of shear modulus ( $\mu_k$ ) of Kelvin element (Figure A5.2c). At the end of relaxation, there is a single governing shear modulus  $\mu'$ . If we keep both shear modulus at constant and vary the viscosity, we can find that relaxation time will increase according to  $\tau = \frac{\eta}{\mu'}$  (Figure A5.2d). In the study we keep the shear modulus  $\mu_e$  constant at  $3 \times 10^{10}$  Pa, the same as the Maxwell model. The viscosity  $\eta_k$  is taken in the range of  $10^{18} - 10^{20}$  Pa s and shear modulus of Kelvin element  $\mu_k$  is varied between  $1 - 6 \times 10^{10}$  Pa.

The Burgers body model is represented by a Kelvin element in series with a Maxwell element. This configuration has two relaxation times due to two viscous components. The standard linear solid model is an extreme case of the Burgers body model when the Maxwell viscosity ( $\eta_m$ ) becomes infinite. Similarly, if the viscosity of the Kelvin element ( $\eta_k$ ) becomes infinite, then the material will behave as a Maxwell body. During the transient relaxation period, the shear modulus relaxes from  $\mu_e$  to long-term shear modulus  $\mu' = \mu_k\mu_e/(\mu_k+\mu_e)$ . We still fix the shear modulus  $\mu_e$  is at  $3 \times 10^{10}$  Pa for comparison purposes. Ryder *et al.* (2011) suggested the optimal ratio for long-term shear modulus to Maxwell shear modulus is 2:3, thus  $\mu_k$  will be fixed at  $6 \times 10^{10}$  Pa. If we keep the Maxwell viscosity ( $\eta_m$ ) constant, it follows that the weaker the Kelvin element is, the larger the difference between the two timescales will be. The two phases of postseismic relaxation differ significantly, which can be seen through curve gradient (Figure A5.2e). The steady-state viscosity  $\eta_m$  controls the magnitude of displacement because the Burgers body model is more sensitive to Maxwell viscosity (Ryder *et al.*, 2011). The fully relaxed displacements do not have much variation according to they have same  $\eta_m$ . However, if we keep  $\eta_k$  constant and increase  $\eta_m$ , the

behaviour of transient state process of those models are the same since they have same Kelvin viscosity (Figure A5.2f). In the following steady-state relaxation, the displacement magnitude decreases with the increasing Maxwell viscosity ( $\eta_m$ ). The larger the  $\eta_m$  is, the slower the displacement will increase with time. The  $\eta_m$  range will be taken between  $10^{18}$  and  $10^{20}$  Pas and  $\eta_k$  will be taken between  $10^{17}$  and  $10^{19}$  Pas in the modelling. When the steady viscosity increase to  $1 \times 10^{21}$  Pa s or larger, the Burger modelling result performs nearly equal to the standard linear result.

## **Acknowledgement**

Minxuan Feng was supported by the Chinese scholarship council (CSC). I would like to thank James Holt for helping me improve the language of the manuscript. All ERS and Envisat data were obtained from the European Space Agency. We thank two anonymous reviewers and the Editor Prof. Duncan Agnew for their valuable comments.

# Chapter 6

## Coseismic and postseismic activity associated with the 2017 Jiuzhaigou Earthquake

### 6.1 Introduction

The Bayan Har terrane has been the most active tectonic unit within the Tibet Plateau over the last twenty years (Deng *et al.*, 2014). Several strong earthquakes ( $M > 7.0$ ) have occurred on the faults along terrane boundary, including, the 1997  $M_w$  7.3 Manyi earthquakes, the 2001  $M_w$  7.8 Kokoxili, and the 2008  $M_w$  7.8 Wenchuan (e.g. Funning *et al.*, 2007, Ryder *et al.*, 2007, Xu *et al.*, 2009) (Figure 6.1a). The  $M_w$  6.5 Jiuzhaigou earthquake occurred on the eastern part of the Bayan Har terrane, which indicates that the terrane is still active. The focal mechanisms from different agencies indicate that this event is a left-lateral strike-slip mechanism with a NNW trending fault and a high-dip-angle fault plane (e.g. Fang *et al.*, 2018, Sun *et al.*, 2018), which is consistent with relocated aftershock sequences (Figure 6.1b).

Table 6.1 Focal mechanism from different institutions

| Institution | Magnitude | Location |         | Depth<br>(km) | Fault plane 1 |     |      | Fault plane 2 |     |      |
|-------------|-----------|----------|---------|---------------|---------------|-----|------|---------------|-----|------|
|             | $M_w$     | Lat      | Lon     |               | Strike        | Dip | Rake | Strike        | Dip | Rake |
| GCMT        | 6.5       | 33.21    | 103.89  | 16.2          | 151           | 79  | -8   | 243           | 82  | -168 |
| USGS        | 6.5       | 33.193   | 103.855 | 9             | 246           | 57  | -173 | 153           | 84  | -33  |
| CENC        | 6.5       | 33.20    | 103.82  | 20            | 326           | 62  | -15  | 64            | 77  | -151 |

Note: China Earthquake Networks Centre (CENC)

The seismogenic fault of the Jiuzhaigou earthquake was previously unidentified and no surface rupture was found after the earthquake. The epicentre located in an area where three tectonic faults interact: the Huya fault, the Tazang fault, and the Minjiang

fault (Figure 6.1a). Historical earthquake documents show that this area has suffered many moderate-strong earthquakes. The 1973  $M_w$  6.5 Huanglong earthquake happened on northern segment of the Huya fault (Zhu and Wen, 2009), which was 30 km southeast from the epicentre of the Jiuzhaigou earthquake and possessed a similar focal mechanism to the 2017 event (Figure 6.1b). The 1976 Songpan earthquake sequence was the latest strong earthquakes that occurred on the Huya Fault (Jones *et al.*, 1984), which three main shocks are located 60–80 km southeast from the epicentre of the Jiuzhaigou earthquake (Figure 6.1b). Determination of accurate fault parameters for the Jiuzhaigou earthquake is important for understanding local rheology and postseismic deformation.

Detailed analysis of a magnetotelluric survey by Bai *et al.* (2010), which concentrate on eastern Tibet, revealed zones of reduced resistivity in the middle to lower crust. The spatial correlation of the low velocity zones in middle and lower crust (e.g. Li *et al.*, 2009a, Xu *et al.*, 2007), the high Poisson ratio (Xu *et al.*, 2007), steep geothermal gradients (Hu *et al.*, 2000), and low electrical resistivity (Bai *et al.*, 2010) are interpreted as zones with elevated fluid content suggesting that the thick crust is locally mechanically weak. Rippe and Unsworth (2010) calculated the effective viscosities range of mid- to lower crust as  $1.7 \times 10^{17}$  to  $1.2 \times 10^{20}$  Pa s for the eastern part of Tibet. To obtain a constraint on the lower crustal viscosity will benefit the rheological research at this region.

Many strike-slip events have been examined geodetically to investigate the rheology of the lower crust and/or upper mantle (e.g. Bürgmann *et al.*, 2002, Pollitz, 2005). The viscosity beneath the coseismic slip area can be explored with measurements of postseismic deformation. We can run various forward viscoelastic calculations of different viscosity values to find the optimal value that best fits the data (e.g. Diao *et al.*, 2011, Gourmelen and Amelung, 2005). The present study uses InSAR data as a basis to investigate postseismic deformation during the eight months following the earthquake. The aim of the study is to determine the rheological structure of the

lithosphere and to compare results obtained with previous rheological studies of the Bayan Har terrane.

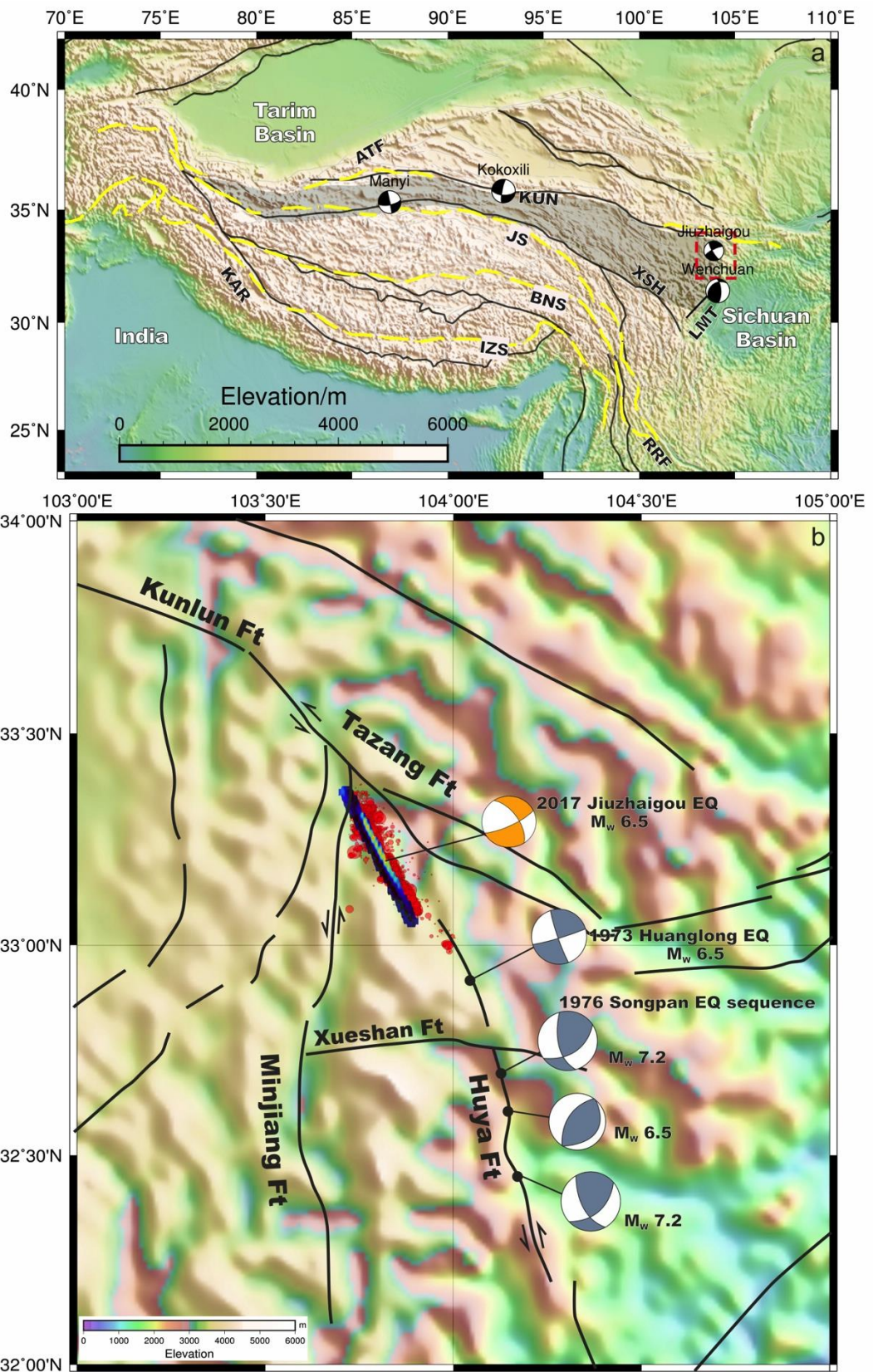


Figure 6.1 a. Sketch map of the Tibet Plateau. The shaded block shows the location of the Bayan Har terrane. The red rectangle indicates the research area of this chapter. Name abbreviations for major features as follows: AMS, Anyimaqen-Kunlun-Muztagh suture zone; ATF, Altyn Tagh fault; BNS, Bangong-Nujiang Suture; IZS, Indus-Zangbo Suture; JS, Jinsha Suture; KAR, Karakoram fault; KUN, Kunlun fault; LMT, Longmen Shan Thrust; MFT, Main Frontal Thrust; RRF, Red River fault; XSH, Xianshuihe fault. b. the tectonic setting of the Jiuzhaigou earthquake area. Faults surrounding the Jiuzhaigou earthquake are plotted with black curves (Fang *et al.*, 2018). Black arrows indicate relative motions along the faults. Major events of the 1976 Songpan earthquake sequence and 1973 Hualong earthquake are plotted with grey filled focal mechanisms. The aftershocks of the 2017 Jiuzhaigou earthquake are plotted with red dots (Fang *et al.*, 2018). The small blue rectangle is the coseismic slip distribution that inverts from data.

## 6.2 Data processing

### 6.2.1 Interferograms

We analysed multiple InSAR data covering the Jiuzhaigou region from the Sentinel-1A (C-band) of the ESA in Image Wide mode. Orbital contributions to the measured displacement are removed by precise orbital information that released by ESA. The Shuttle Radar Topography Mission (SRTM) DEM with 30 m (Farr *et al.*, 2007) resolution is used to remove the phase component contributed by the topography. Data was processed by the ISCE software (Rosen *et al.*, 2011). The ascending track (T128) is used in both coseismic and postseismic phase and the descending track (T62) is only used for the coseismic phase. 21 scenes of SAR data along the ascending track are used to compute postseismic interferograms (Figure 6.2). All interferograms are generated from SAR images with a perpendicular baseline not greater than 50m (Figure 6.2). Satellite imagery from August 2017 and April 2018 was used to construct time series in this study.

Table 6.2 Details of the Data used in the following analysis

|             | Geometry   | Track | Start Acquisition (yyyymmdd) | Last Acquisition (yyyymmdd) | Numbers of Dates |
|-------------|------------|-------|------------------------------|-----------------------------|------------------|
| Coseismic   | Ascending  | 128   | 20170730                     | 20170811                    | 2                |
| Coseismic   | Descending | 62    | 20170806                     | 20170818                    | 2                |
| Postseismic | Ascending  | 128   | 20170811                     | 20180420                    | 22               |
| Postseismic | Descending | 62    | 20170818                     | 20180310                    | 17               |



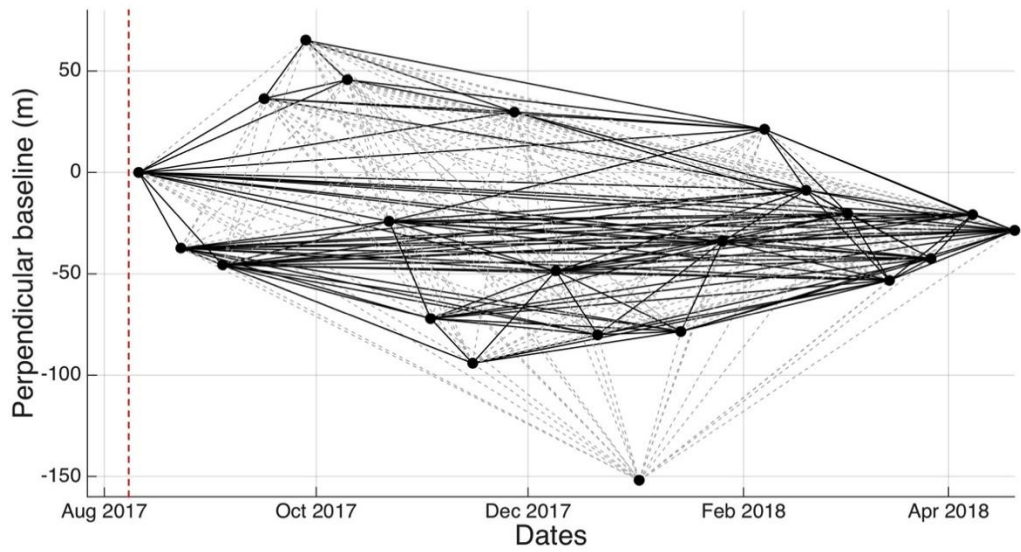


Figure 6.2 Baseline versus time plots for the ascending track 128. The black dots represent all available acquisitions. Solid black lines represent interferograms where perpendicular baselines are smaller than 50m. The grey dash lines represent interferograms where perpendicular baseline are greater than 50m. The red dash line represents the date when the earthquake happened.

## 6.2.2 Correction of atmospheric and orbital error

The residual orbital error represents one or two fringes at most (Lopez-Quiroz *et al.*, 2009). To remove the effect of residual orbital errors, we estimate the best fitting ‘twisted plane’ (Cavalié *et al.*, 2007) using a first-order approximation. The residual orbital error is represented by

$$\varphi_{orb} = ax + by + cxy + d \quad (6.1)$$

where  $x$  and  $y$  are the range and azimuth coordinates and  $a$ ,  $b$ ,  $c$  and  $d$  are constants and obtained using a least square minimization from the non-deformed area.

When the radiation signal travel through atmosphere, it will suffer both ionospheric and tropospheric delays. However, the ionospheric propagation delay is more obvious in larger wavelengths, such as for the P and L-band, and has comparatively less effect on the C-band data (Gray *et al.*, 2000). The Sentinel-1 satellite provides data in C-band. Therefore, we only consider the tropospheric delay. Tropospheric delays can

be calculated by empirical relationship between interferogram and elevation (e.g. Doin *et al.*, 2009, Lopez-Quiroz *et al.*, 2009) or by using external information from GPS measurements, weather models, multi-spectral observation and so on (e.g. Li *et al.*, 2006, Li *et al.*, 2009b, Wadge *et al.*, 2002, Bekaert *et al.*, 2015b).

Yu *et al.* (2017) proposed a new atmospheric model, the Iterative Tropospheric Decomposition (ITD) interpolation model, to correct tropospheric delay. The ITD interpolation model is based on HRES-ECMWF product in addition to GPS interpolation. This model generates high spatial resolution zenith total delay maps for correcting InSAR data. It is globally available and operated in a near real time mode, which can be obtained from Generic Atmospheric Correction Online Service (GACOS).

To test this new atmospheric correction model, we compare the result to that obtained from the traditional empirical altitude related method (Hanssen, 2001). The tropospheric delays  $\varphi_{tropo}$  and the orbital error  $\varphi_{orb}$  can be jointly estimated for each interferogram as  $\varphi_{tropo} + \varphi_{orb} = ax + by + cxy + kh + d$  (e.g. Doin *et al.*, 2009). With the deformed area masked out, the parameters a, b, c, d, k, can be calculated using a least square minimization. This method has been successfully applied in many previous studies, such as the Manyi earthquake (Feng *et al.*, 2018), and the Damxung earthquake (Bie *et al.*, 2014).

An example interferogram (170916-171010) applied with two correction methods is shown in Figure 6.3. One uses the empirical linear relationship (DEM) that is correlated with altitude and the other one use high-resolution ECMWF (GACOS) as external datasets. The LOS displacement change standard deviation across the entire interferogram was computed to assess the precision (e.g. Li *et al.*, 2006). The standard deviations of the residuals after correcting with these two methods are shown in Figure 6.4. The standard deviation of the corrected product is relatively stable for all interferograms. The correction result obtained through GACOS is slightly better than

that based on topography at the very early interferograms. From the reduction of standard deviation (Figure 6.5), we can see that corrections derived from GACOS produce increases of the standard deviation at the latter term interferograms. The empirical linear correction has a relative more stable performance than the GACOS method. Therefore, we still use the empirical linear relationship to calculate the propagation delay and then subtract this error from the interferogram. Corrected coseismic interferograms are used for exploring fault parameters and determining coseismic slip distribution, while corrected post-seismic interferograms are used for constructing time-series displacement.

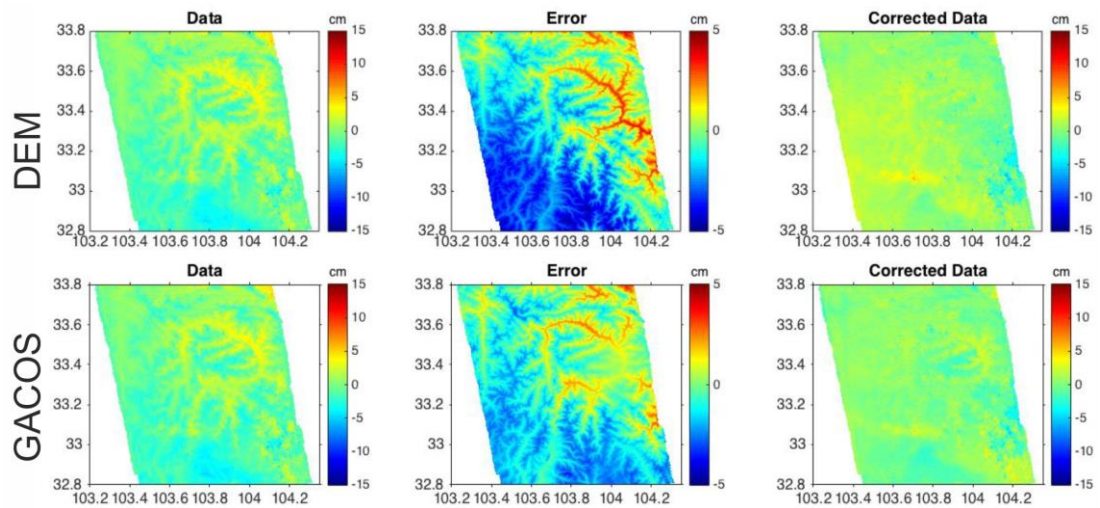


Figure 6.3 Comparison between the two correction methods. The error includes both residual orbital error and atmospheric error. The top set is based on signals correlated with altitude and the bottom ones are based on the ITD model. The interferogram is obtained between 20170916 to 20171010.

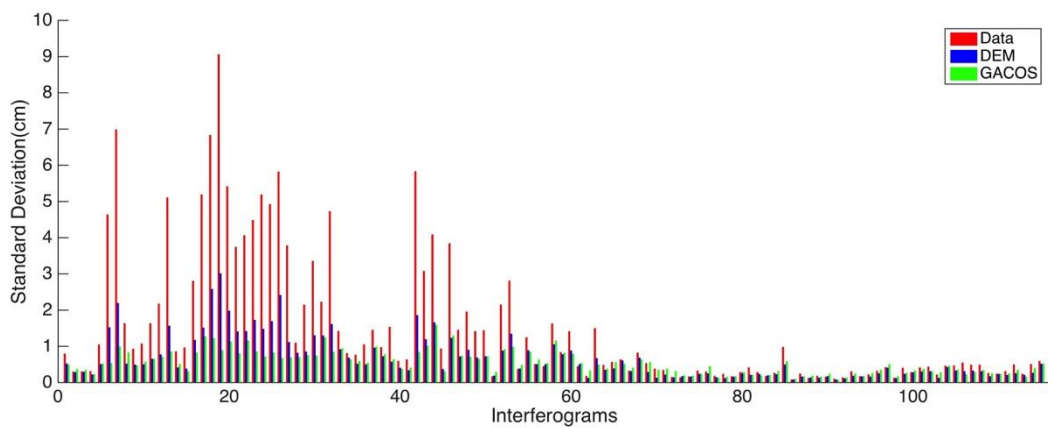


Figure 6.4 Comparison between different correction methods. The standard deviation of the original interferograms (red bars) compared to the residual standard deviation after correcting for the tropospheric delay derived from topography (blue bars) and GACOS (green bars).

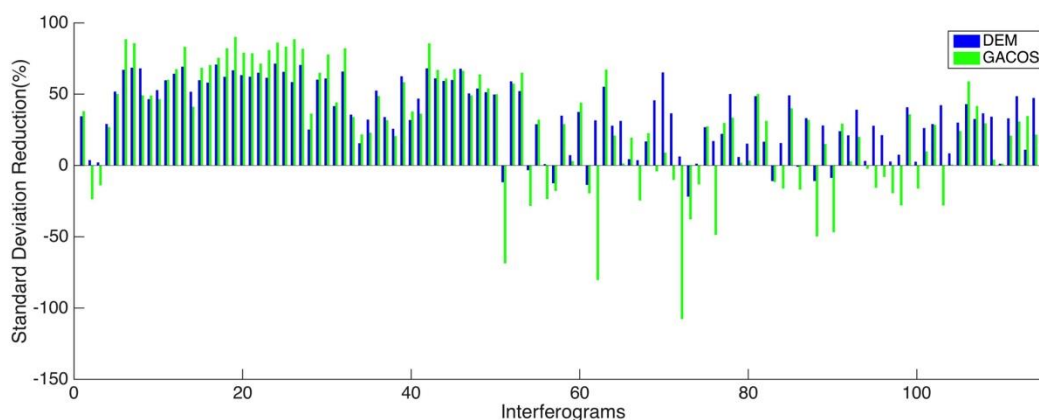


Figure 6.5 Reduction of standard deviation after correction of the interferograms. The percentage is equal (original data – corrected data)/original data. The x-axis is the interferogram number. Interferograms are ordered in terms of their respective acquisition and time span.

### 6.3 Aftershocks

We use the aftershock dataset obtained from the China Earthquake Data Centre (<http://data.earthquake.cn>) to carry out the temporal analysis of aftershock. The relationship between the number of aftershocks  $n(t)$  for the first 6 months (considering events until Jan 2018) and time  $t$  can be fitted by a curve (Figure 6.6) using an Omori-type law:

$$n(t) = k(t + c)^{-p} \quad (6.2)$$

where  $\mathbf{k}$ ,  $\mathbf{c}$  and  $\mathbf{p}$  are constants. The exponent  $\mathbf{p}$  is a measure of the decay rate of aftershocks (Shcherbakov *et al.*, 2004). For the Jiuzhaigou earthquake,  $\mathbf{p} = 1.127$ , which is consistent with the value published for other earthquakes (such as 1.22 for the Landers earthquake, 1.21 for the Hector Mine earthquake in Shcherbakov *et al.*, 2004). The magnitude of the largest aftershock is 4.8, which happened two days after the main shock. All the other aftershocks are at least two orders of magnitude smaller than the main shock (Fang *et al.*, 2018). The cumulative moment released by the

aftershocks during first six month is  $6.48 \times 10^{16}$  N m, which represents only 1 percent of the coseismic moment. Therefore, very little surface deformation related to the seismic process will occur that can be observed at the surface. As a result, aftershocks are not considered for the remainder of this study.

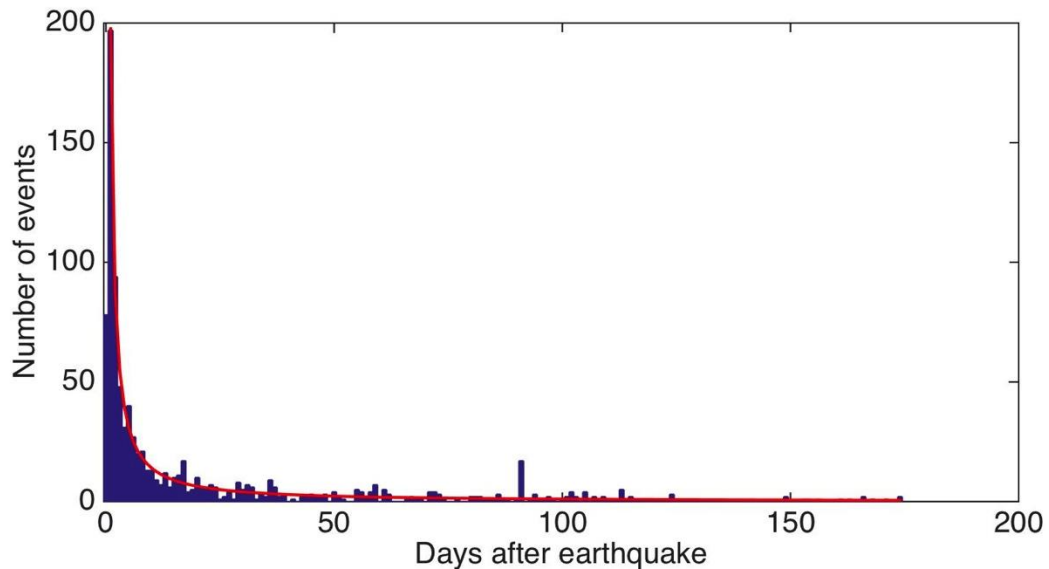


Figure 6.6 Number of aftershocks as a function of time after the Jiuzhaigou earthquake. Aftershock dates are taken from the China Earthquake Data Centre. A curve with the functional form of the Omori-type equation is fitted. The exponent  $p$  is 1.127.

## 6.4 Coseismic slip inversion

As the location of the seismogenic fault of Jiuzhaigou earthquake is previously unknown, we want to obtain the fault geometry for the Jiuzhaigou earthquake from the coseismic interferograms including fault location, strike, dip, rake, slip, fault length, upper and lower depth of the fault. A homogeneous elastic half-space model (Okada, 1985) is used for the inversion. A non-linear inversion is used to estimate all the fault parameters listed above. A linear inversion is then employed to calculate distributed slip, with other parameters fixed.

We use the open-source Geodetic Bayesian Inversion Software (GBIS) to estimate the model parameters from both ascending and descending LOS displacements. The inversion code uses a Markov-Chain Monte Carlo algorithm, incorporating the

Metropolis-Hasting algorithm (Gonzalez et al., 2015, Hooper et al., 2013, Mosegaard and Tarantola, 1995) to estimate the posterior probability distribution for all fault parameters. The Gaussian distribution of the model's parameters gives the optimal model solution and uncertainties. The priori values of the source model for the prior distribution is chosen either by arbitrarily or by simulated annealing method (Bagnardi and Hooper, 2018). The unwrapped interferogram is down-sampled using a quadtree resampling method to accelerate the calculation procedure. This resampling technique will reduce the number of data points with the highest density close to the area affected by the maximum displacement gradient (Figure S6.1).

During the inversion, all fault parameters will vary among the reasonable intervals that listed in Table 6.3. As this earthquake is dominated by a left-lateral fault motion with a small component of normal slip, both strike and normal slip mechanisms are investigated by allowing the slip along the strike and dip directions to vary.

Table 6.3 Fault parameter intervals and best-fit solution resulting from the nonlinear inversion

| Parameter   | Length (km) | Width (km) | Depth (km) | Dip (°) | Strike (°) | X-pos (km) | Y-pos (km) | Strike slip(m) | Dip slip(m) |
|-------------|-------------|------------|------------|---------|------------|------------|------------|----------------|-------------|
| Lower bound | 10          | 0          | 0          | 50      | 140        | -8         | -8         | -3             | -1          |
| Upper bound | 35          | 25         | 25         | 90      | 160        | 8          | 8          | 3              | 1           |
| Optimal     | 25.93       | 1.32       | 5.02       | 81.46   | 153.57     | -0.52      | 0.97       | -2.94          | 0.44        |

The starting value of X and Y position corresponds to Longitude=103.82° , and Latitude 33.2°

In Figure 6.7 and Figure 6.8, we show the comparison among observed displacements, model prediction, and residuals. The obtained optimal fault parameters reveal a northwest striking, southwest dipping strike-slip fault. Figure 6.9 shows the posteriori probability density of each fault parameter. The high-dip-angle fault plane is consistent with the relocated aftershocks (Figure 6.10). This fault geometry will be used to obtain slip distributions on multiple fault patches through a linear inversion approach.

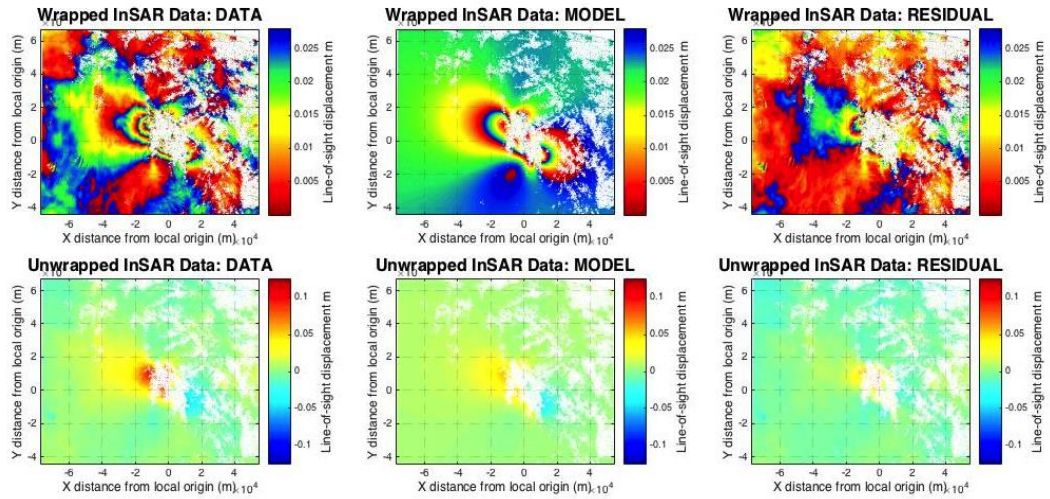


Figure 6.7 InSAR data of track 62 and corresponding elastic model. Left panels: wrapped and unwrapped coseismic interferogram of ascending track 62. Centre panels: wrapped and unwrapped best-fitting elastic dislocation model for uniform slip on a rectangular plane obtained from the inversion of InSAR data. Right panels: wrapped and unwrapped residuals between the data and the model. Coordinates refer to a local origin (Longitude =  $103.82^\circ$  and Latitude =  $33.2^\circ$  ).

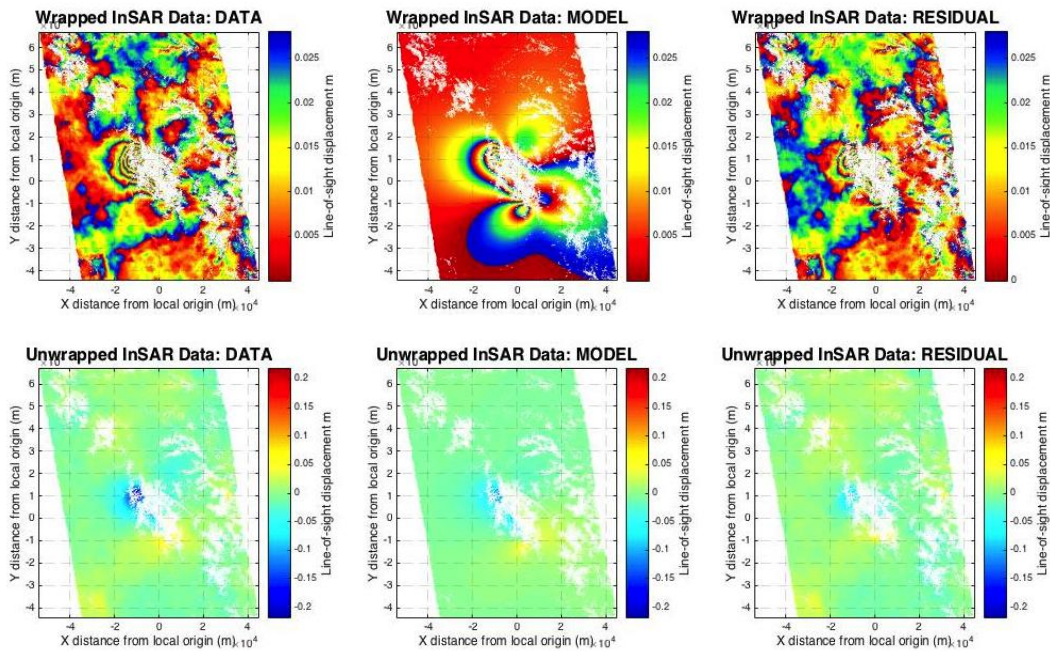


Figure 6.8 InSAR data of track 128 and corresponding elastic model. Left panels: wrapped and unwrapped coseismic interferogram of ascending track 128. Centre panels: wrapped and unwrapped best-fitting elastic dislocation model for uniform slip on a rectangular plane obtained from the inversion of InSAR data. Right panels: wrapped and unwrapped residuals between the data and the model. Coordinates refer to a local origin (Longitude =  $103.82^\circ$  and Latitude =  $33.2^\circ$  ).

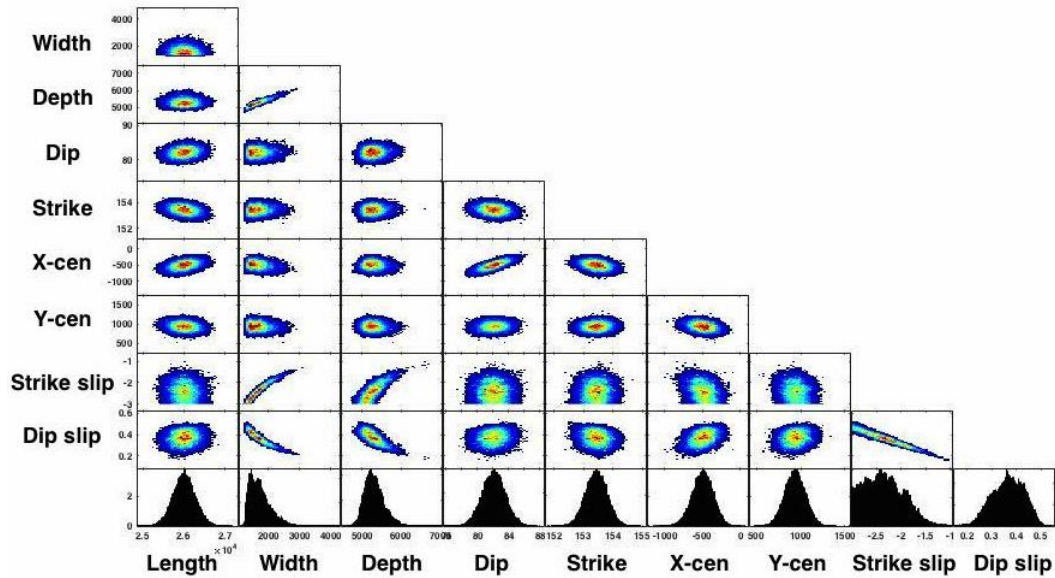


Figure 6.9 Fault parameter uncertainties distribution of the uniform slip InSAR model. Scatter plots are contoured according to frequency (cold colours for low frequency, warm colours for high frequency). The burning time of  $2 \times 10^4$  iterations is removed.

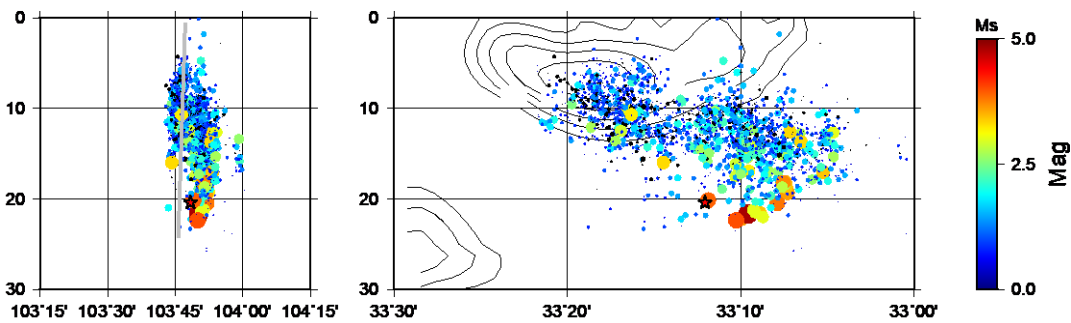


Figure 6.10 Aftershocks of the Jiuzhaigou earthquake. The cross section profiles demonstrate the distributions of relocated aftershocks along the A<sub>1</sub>A<sub>2</sub> and B<sub>1</sub>B<sub>2</sub> profiles, respectively. The contours lines show the slip distribution constrained by InSAR data in Figure 6.12.

We used SDM to implement the linear inversion process. This slip inversion code is written in FORTRAN by Wang *et al.* (2013b) and uses the Steepest Descend Method and Laplacian smoothing to solve slip distribution. The fault plane is discretized into  $1 \text{ km} \times 1 \text{ km}$  patches to account for the slip distribution. The down dip width of the fault is extended to 25 km depth and along the strike length is extended to 40 km. We initially fixed fault orientation parameters (strike, dip and location) that have been derived from the uniform slip model. The rake is allowed to vary between  $-45^\circ$  to  $45^\circ$ . The optimal smoothing factor (0.035) for the inversion was chosen from the knee of the L-curve between model roughness and misfit (Figure 6.11). The adjacent



values of the smoothing factor do not present obvious difference in recovered surface deformation (Figure S6.2). The slip uncertainty of the slip distribution cannot be directly got from a single SDM calculation. I prepared 100 groups of InSAR data plus random noise that generated by full variance-covariance matrix (e.g. Wright *et al.*, 2004, Parsons *et al.*, 2006). Then I run the SDM for 100 times with these noisy data sets to calculate the average and uncertainty of the slip distribution (Figure 6.12 and Figure 6.13).

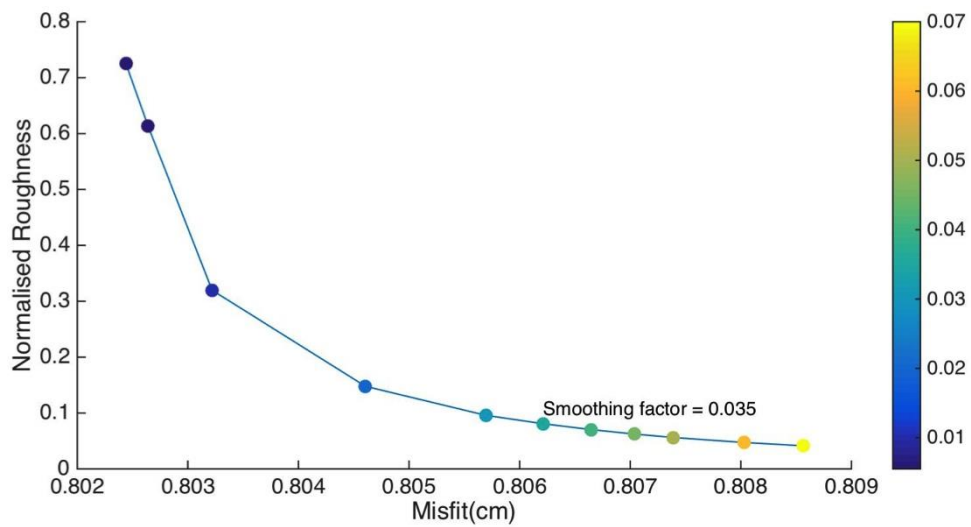


Figure 6.11 Trade-off curve between the misfit and model roughness. The text indicates the location of the optimal smoothing parameter where the balance between the model misfit and smoothness is achieved. The colour scale indicates the value of the smoothing factors.

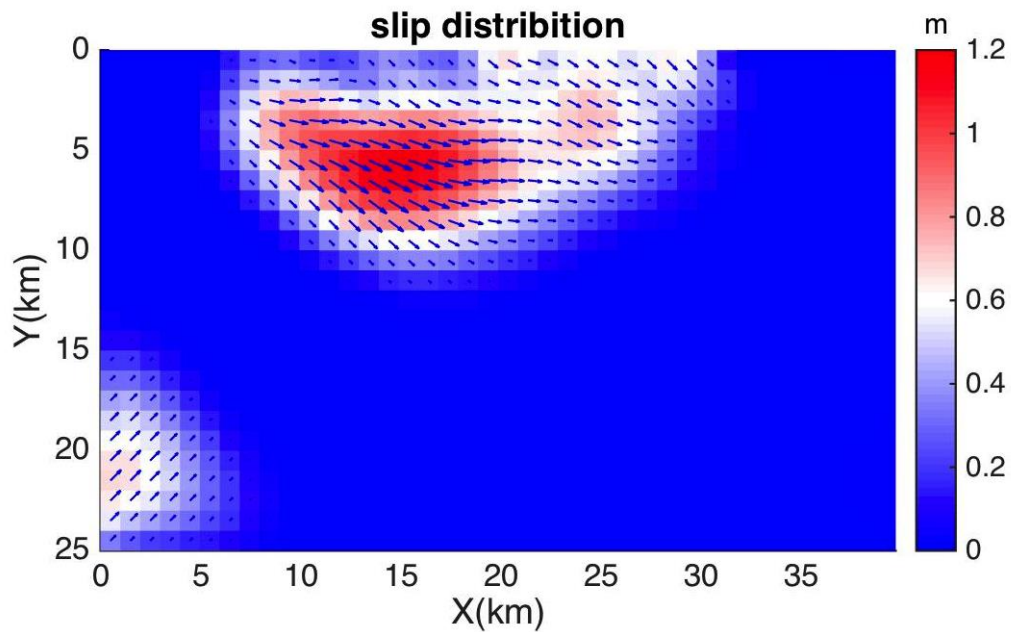


Figure 6.12 Slip distributions on the fault plane. The colour bar indicates the amount of fault-slip. Arrows denote the fault slip vectors. The maximal fault sliding is about 1.1628 m.

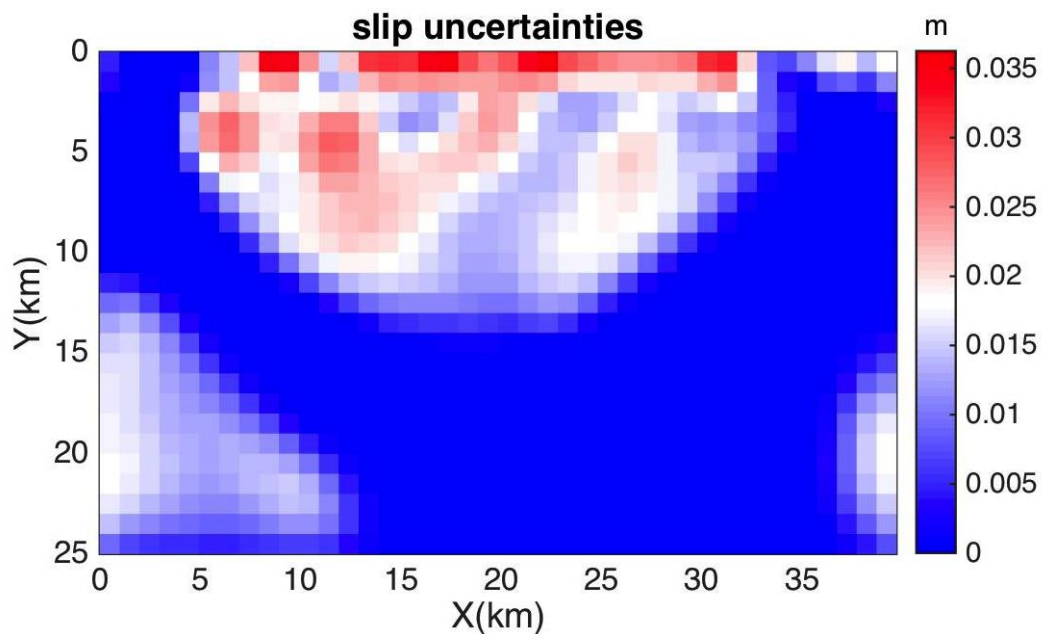


Figure 6.13 Uncertainty with the slip distributions. The maximal uncertainty of the fault sliding is about 3.63 cm.

Similar to the uniform slip model, we jointly modelled two interferograms for distributed slip model. Our preferred coseismic model has a maximum slip of 1.1628 m (Figure 6.12). Assuming the shear modulus is  $\mu=32\text{GPa}$ , the seismic moment of the earthquake is about  $5.31\times 10^{18}\text{ Nm}$  and the moment magnitude is equal to  $M_w$  6.41, which is comparable to the magnitudes determined by different agencies (Table 6.1).

The concentrated slip patch is located at a depth of 2–12 km and the peak slip occurs at a depth of ~5-10 km. The slip vector indicates predominate left-lateral strike-slip motion with negligible normal dip component. The mean rake angle is approximately  $-13.64^\circ$ . Aftershocks were generally distributed along the fault strike (Figure 6.14) and in a downdip direction (Figure 6.10).

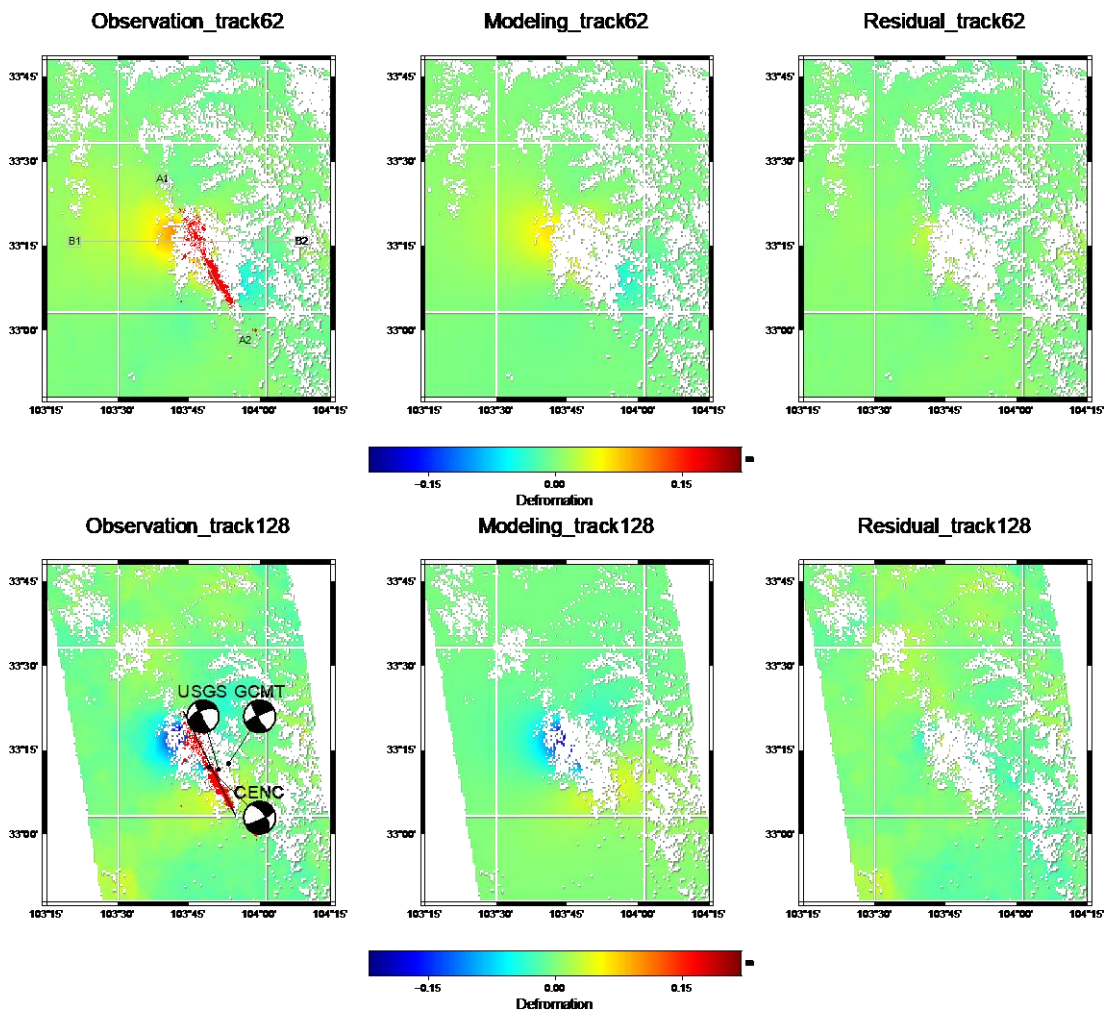


Figure 6.14 Coseismic interferograms inverted from the coseismic slip and modelled surface displacement of the Jiuzhaigou earthquake (the positive range change indicating motions away from the satellite). The red line represents the fault orientation that obtains from the uniform slip model. The red dots represent the relocate aftershocks within the first month after the main shock (Fang *et al.*, 2018). A<sub>1</sub>A<sub>2</sub> and B<sub>1</sub>B<sub>2</sub> are the profile's location as shown in Figure 6.10.

## 6.5 Postseismic deformation

### 6.5.1 Time-series

For postseismic deformation, the coherence of track 62 is generally very low, we only use track 128 to undertake the postseismic deformation analysis. Out of a total of 117 interferograms, we chose 23 interferograms to construct a time-series of post-seismic deformation using the Small Baseline Subset algorithm (Berardino *et al.*, 2002) and least squares inversion (Schmidt and Bürgmann, 2003). LOS displacements at successive dates with reference to the same acquisition were generated (Figure 6.15). Even though the interferograms used in the time series construction have already been corrected, the postseismic deformation time-series reveal no obvious deform signal that associate with the fault. The surface deformation that is generated by fault creeping is smaller than the noise in the InSAR measurements during the observation period.

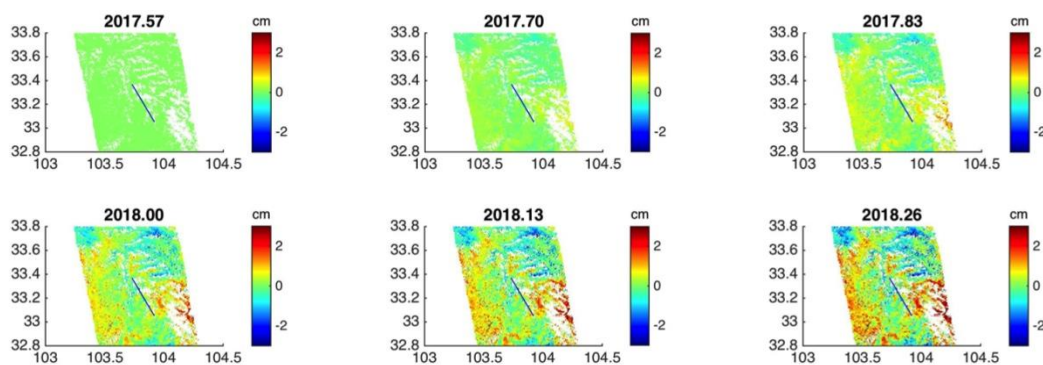


Figure 6.15 Postseismic deformation time-series. The black line represents the fault trace inferred in this study. Here, we only show 6 dates out of all acquisitions.

## 6.5.2 Modelling

The viscosity of the lower crust of Tibet has been estimated from InSAR studies of several earthquakes that have occurred in recent years (e.g. Ryder *et al.*, 2011, Ryder *et al.*, 2007, Wen *et al.*, 2012). The viscosity of the eastern Tibet is mainly obtained from the Wenchuan earthquake, which is happened on east margin of the Tibetan Plateau. We estimate viscosity for the Jiuzhaigou area by comparing observed InSAR deformations with modelling displacements. The mantle viscosity will be poorly constrained due to the thick crust (>60km). As a result, we only use a simple Earth

model that consists of an elastic layer overlying a homogenous viscous half-space in viscoelastic forward calculation.

I use the PSGRN/PSCMP program (Wang *et al.*, 2006) to model the postseismic deformation change. It includes two packages: PSGRN which calculates Green's functions for the given layered model and PSCMP which calculates postseismic displacements at a given time (Wang *et al.*, 2006). The multi-layered lithospheric model and relevant parameters (e.g. P and S-wave velocity, density) for the Jiuzhaigou region (see Table 6.4) are obtained from the combination of Crust1.0 model and Shao *et al.* (2011). The upper crust is set as a pure elastic layer whereas the middle crust, lower crust and mantle are set as viscoelastic layers.

Table 6.4 Structure model for Jiuzhaigou earthquake

| No. | Layer        | Bottom Depth (km) | Vp(km/s) | Vs(km/s) | Density (kg/m <sup>3</sup> ) | Viscosity (Pas) |
|-----|--------------|-------------------|----------|----------|------------------------------|-----------------|
| 1   | Upper crust  | h(15/20/25)       | 6.1      | 3.55     | 2740                         | $\infty$        |
| 2   | Middle crust | 45                | 6.3      | 3.65     | 2780                         | $\eta$          |
| 3   | Lower crust  | 60                | 7.0      | 3.99     | 2950                         |                 |
| 4   | Upper mantle | >60               | 8.05     | 4.47     | 3320                         |                 |

Note:  $\infty$  means this layer is set as pure elastic. h is the thickness of the elastic layer.  $\eta$  is the viscosity of the beneath half space.

In order to acquire a primary idea of the viscoelastic relaxation expression, we first run a forward model using an arbitrary viscosity ( $5 \times 10^{17}$  Pa s) of a Maxwell rheology under a 15 km elastic layer. The coseismic distributed slip model (Table 6.3) and multi-layered earth model (Table 6.4) are used in the forward calculation. The modelled pattern of the displacement has a wide distribution, with positive and negative lobes in each direction of the fault (Figure 6.16). In the postseismic deformation time-series, we discover no clear evidence of such deformation patterns over the fault. Therefore, it is impossible for us to estimate the optimal viscosity

directly. The method used by Wimpenny *et al.* (2017) is adopted to constrain local rheology beneath the elastic upper crust in eastern Tibet. A lower bound on the viscosity of the lower crust is estimated by running multiple viscoelastic models with different viscosities of the Maxwell half-space.

Surface displacement from each forward calculation is converted to LOS displacement and used to calculate the signal-to-noise ratio (SNR). The SNR is defined by the ratio between the maximum-modelled LOS displacement and standard deviation of pixel LOS variations of the interferograms (Wimpenny *et al.*, 2017). If  $SNR > 1$ , the viscoelastic relaxation related deformation can be detected in the interferograms.

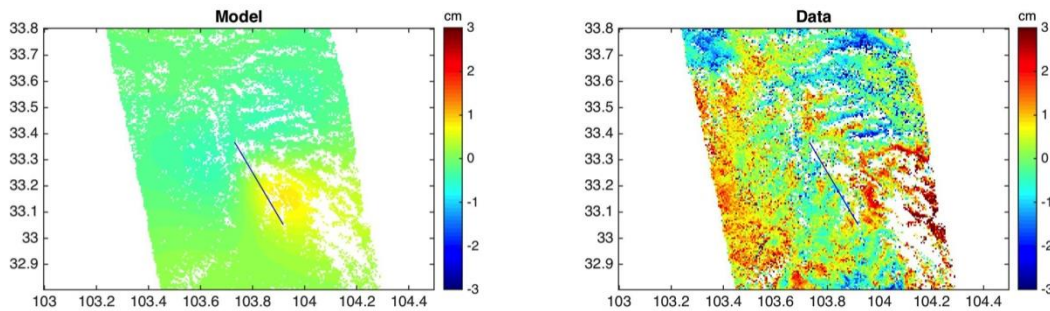


Figure 6.16 An example of one forward viscoelastic calculation. The black line represents the fault trace inferred in this study. The data here cover 183 days after the earthquake.

We vary the viscosity ( $\eta$ ) and elastic layer thickness ( $h$ ) in the forward calculation. The minimum possible viscosity of the viscoelastic layer ranges from  $\sim 6 \times 10^{17}$ - $1.58 \times 10^{18}$  Pas (Figure 6.17) for layer thickness of 15-25km, respectively. Based on a realistic estimate of the elastic layer thicknesses of 25 km, where most coseismic slip and aftershocks occur, we prefer the minimum possible viscosity of the underlying half-space to be  $\sim 6 \times 10^{17}$  Pa s. If the viscosity is lower than this lower bound value, the surface deformation result by viscoelastic relaxation should be observable, which is inconsistent with the observations made.

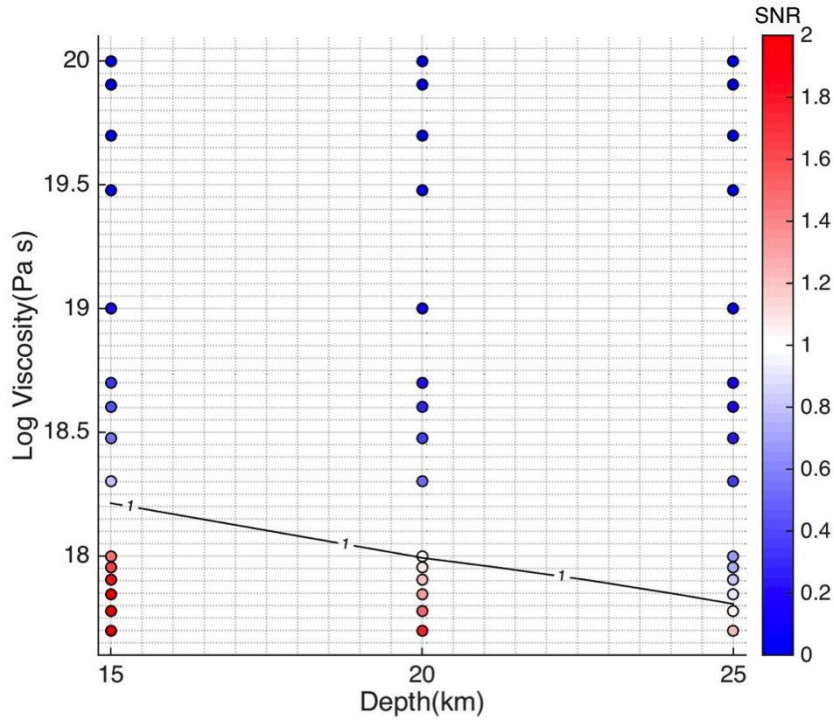


Figure 6.17 The signal-to-noise ratio of forwarding calculations with variable elastic layer thickness ( $h$ ) and viscosity ( $\eta$ ). The SNR=1 contour line marks the upper bound of the viscoelastic relaxation.

## 6.7 Discussion and Conclusions

A field investigation of the Jiuzhaigou earthquake indicates that there is no visible surface fracture (Xu *et al.*, 2017). Our coseismic slip inversion results show that the slips close to the surface of Jiuzhaigou earthquake are relatively small, and may not have been large enough to cause the surface rupture. This is consistent with the result of the field investigation. Jiuzhaigou earthquake happened on a buried fault that has not been identified before. Three tectonic faults (the Minjiang fault, the Tazang fault and the Huya fault) are present in the epicentre area (Figure 6.18), which fault cause this earthquake is not clear yet. The Minjiang Fault is unlikely to be the potential seismogenic fault due to the fact that epicentre of the Jiuzhaigou earthquake is away from the Minjiang Fault compared to the other two faults. Our preferred fault geometry is close to the Tazang fault at the northern end, and spreads to the northern Huya fault at the southern end (Figure 6.1a). Tazang Fault is the easternmost continuation of the Kunlun Fault and is active since the Holocene epoch (Ren *et al.*, 2013). The western segment of Tazang fault has a left-lateral movement, while the

eastern segment has a dominant reverse mechanism (Ren *et al.*, 2013, Jones *et al.*, 1984). The strike of the Tazang fault varies from 113° to 130° from west to east (Hu *et al.*, 2017). The dip angle of the nearest segment of the Tazang fault to the Jiuzhaigou earthquake is from 40° to 65°. The Xueshan fault divided the Huya Fault into northern and southern sections (Figure 6.18). The northern section of the Huya fault extends in southeast direction with a steep (>60°) westward dip (Kirby *et al.*, 2000). The 1973 Huanglong M6.5 earthquake along with 1976 Songpan earthquake sequence that happened on Huya fault all showed predominate left-lateral strike-slip motion (Jones *et al.*, 1984). Focal mechanisms of these historical earthquakes are similar to that of the Jiuzhaigou earthquake. Although the epicentre of the Jiuzhaigou earthquake is close to the south-eastern segment of the Tazang Fault, the focal mechanism demonstrates a significant difference from the geological features of Tazang fault. On the contrary, the focal mechanism is very consistent with the geometric characteristics of the northern section of the Huya Fault. Therefore, the Jiuzhaigou earthquake is possibly caused by the north-westwards activity of the Huya Fault along the northern section.

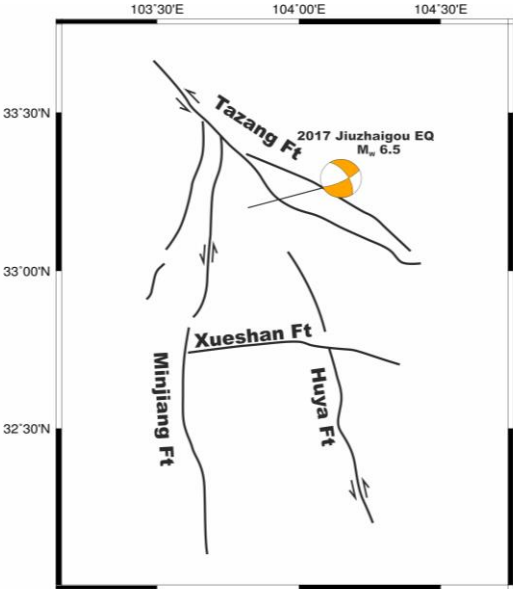


Figure 6.18 Simplified tectonic sketch map around the Jiuzhaigou earthquake area.

Most of the viscosity estimations of the eastern margin of the Tibetan lower crust from different types of constraints span a wide range, from  $3 \times 10^{17}$  to  $3 \times 10^{19}$



Pas across all time scales (Huang et al., 2014 and reference therein). A lower bound of  $4 \times 10^{17}$  Pa s is inferred for the mid/lower crust viscosity of this part from 14 days postseismic deformation of the Wenchuan earthquake (Shao *et al.*, 2011), which is about 150 km away from the Jiuzhaigou earthquake. The viscosity derived from 7 years of postseismic GPS data following the Wenchuan earthquake is  $\sim 2 \times 10^{18}$  Pa s (Diao *et al.*, 2018). The postseismic deformation is not easily observed in the Jiuzhaigou area. After removing the atmospheric noise and residual orbital error, it is still difficult to see obvious deformation from the corrected interferograms. The minimum possible viscosity of the underlying half-space by SNR from our study about this area is  $\sim 6 \times 10^{17}$  Pa s. Our result is larger than that obtained by Shao *et al.* (2011) but smaller than that calculated by Diao *et al.* (2018). The effective lower crustal viscosities generally increase with time during the postseismic deformation process, which has been observed in other earthquakes, such as the Manyi earthquake (Ryder *et al.*, 2007, Feng *et al.*, 2018). Therefore, our preferred minimum viscosity ( $6 \times 10^{17}$  Pa s) from eight month's postseismic deformation is within the viscosity range derived from the adjacent earthquake.

The Jiuzhaigou earthquake is very similar to the Bam earthquake ( $M_w=6.6$ ), which also happened on a blind strike-slip fault and did not exhibit major surface rupture. 7 years of postseismic data from the Bam earthquake reveal no evidence for a long-wavelength deformation signal that might be associated with afterslip or viscoelastic relaxation beneath the coseismic rupture (Wimpenny *et al.*, 2017). Only short-wavelength ground deformation that focused around the tips of the seismogenic fault is observed in the long-term ( $>3.5$  years) postseismic deformation (Fielding *et al.*, 2009). Therefore, it is possible that a longer time span of the postseismic deformation of the Jiuzhaigou earthquake may provide greater deformation signals in the future.



# Chapter 7

## Discussion

This chapter discusses several aspects that arise from the study of two strike-slip earthquakes. The rheology obtained from the two case studies is compared with previous rheologies estimated in the region (see Table 7.1), which can give us an overview of the variation in rheology across the Tibetan Plateau. We discuss the spatial and temporal characters of rheology. The postseismic deformation of different earthquakes can be explained by different mechanisms. The postseismic deformation of an individual earthquake can be explained by various mechanisms. We discuss the aspects that may affect postseismic modelling.

### 7.1 Rheology estimates from various studies and their spatial-temporal characteristics

#### 7.1.1 Summary of the various studies

In northern-central Tibet, most viscosities have been estimated from geodetic measurements of the Manyi earthquake and the Kokoxili earthquake (Figure 7.1). Inferred lower crustal viscosities across most studies in this area lie in the range of  $5 \times 10^{17} - 5 \times 10^{19}$  Pa s (Table 7.1). The lowest bound of the viscosity is  $5 \times 10^{17}$  Pa s given by Shen *et al.* (2003), based on 6 months postseismic deformation of the Kokoxili earthquake. Geological data indicate that the viscosity range from  $10^{19}$  Pa s to  $10^{21}$  Pa s, which is slightly larger than the range obtained from InSAR data. Yamasaki and Houseman (2012) used a depth-dependent viscosity model to fit the 4 years postseismic displacement of the Manyi earthquake, and it is noted that the viscosity decreases exponentially from  $1.2 \times 10^{21}$  Pa s at 10 km (top of the viscoelastic layer) to  $1.6 \times 10^{18}$  Pa s at 60 km (the Moho depth). The range estimated by

Yamasaki and Houseman (2012) almost encompasses viscosities range estimated from either geodetic or geological data. Feng *et al.* (2018) uses 12 years InSAR postseismic deformation time-series of Manyi earthquake, which is the longest time span in this area, to give the viscosity of  $5 \times 10^{19}$  Pa s (see chapter 5). The value reported in this thesis closely matches previous published viscosity results based on different models. However, due to the thickness of the crust, we cannot provide a robust constraint for the viscosity of the upper mantle.

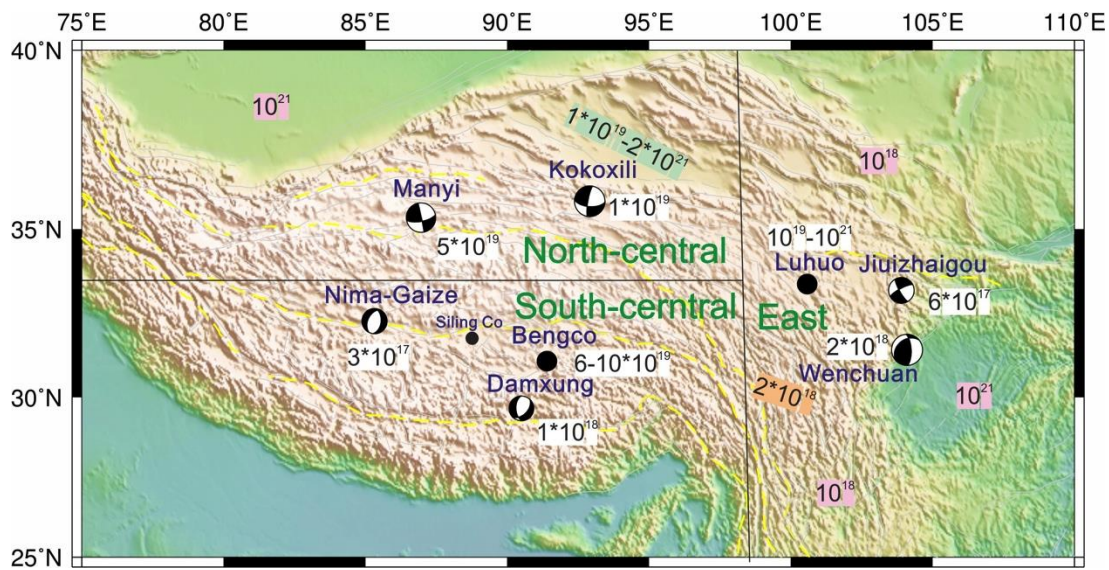


Figure 7.1 Location map of previous studies. Here, we only mark the viscosity obtained from the longest time span of postseismic deformation. The number filled with colour represent the viscosity obtains from topographic variation. The green colour represents the values obtained by Hilley *et al.* (2005). The orange colour represents the value obtained by Clark *et al.* (2005). The pink colour represents the value obtained by Clark and Royden (2000).

In the southern-central Tibet, the lower crustal viscosities are mainly constrained by postseismic deformation following two moderate normal faulting earthquakes (Nima-Gaize and Damxung earthquakes) and the geological observation from the Siling Co lake (e.g. Bie *et al.*, 2014, Ryder *et al.*, 2010, Doin *et al.*, 2015). The minimum lower viscosity is  $\sim 3 \times 10^{17}$  Pa s (Ryder *et al.*, 2010) with 9 month postseismic deformation. Ryder *et al.* (2014) investigate two 1950s earthquakes with a late postseismic InSAR observation, and find that the observations can be best explained by viscoelastic relaxation in the lower crust and/or upper mantle. The optimal viscosity is  $6 \times 10^{19}$  Pa s with a 60km thick viscoelastic layer. The shoreline

deflection around Siling Co over millennial timescales indicates that the average viscosity is  $\leq (1-2) \times 10^{19}$  Pa s (Shi *et al.*, 2015). On the time scale of decades, the lower crustal viscosity beneath southern-central Tibet is about  $(1-6) \times 10^{19}$  Pa s.

The postseismic deformation of the disastrous Wenchuan earthquake provides a unique opportunity for people to investigate viscosity in Eastern Tibet. Due to the lack of InSAR data, most postseismic research is based on GPS data. The obtained viscosities mainly concentrate around  $1 \times 10^{18}$  -  $3 \times 10^{18}$  Pa s. Only one study, which used the earliest 14 days postseismic deformation (Shao *et al.*, 2011), gave a viscosity of  $4 \times 10^{17}$  Pa s. A lower bound of  $6 \times 10^{17}$  Pa s is given by the Jiuzhaigou earthquake for 8 months postseismic deformation in the previous chapter. Derived from the geodetic data, the viscosity of the Eastern Tibet is about  $10^{17}$  -  $10^{18}$  Pa s.

Geodynamic modelling is also commonly used to estimate the viscosity of the Tibet Plateau. (e.g. Clark and Royden, 2000, Cook and Royden, 2008, Rippe and Unsworth, 2010). The range between crustal viscosities from the geodynamic models for the whole Tibetan Plateau is five orders of magnitude (Table 7.1). A lateral homogeneous Earth model is always considered in these studies. For example, the topographic variation of the eastern Tibetan Plateau has always been used to estimate lower crustal mechanical properties. Clark and Royden (2000) proposed an Earth model that had a weak channel within the crust to explain the topography variation of the Tibetan Plateau. The steep western margin of the Sichuan Basin fits with a much higher channel viscosity of  $10^{21}$  Pa s, while the gently topographic gradients at northwest and southwest of the Sichuan Basin show a good fit for a lower crustal viscosity of  $10^{18}$  Pa s. In the flat central Tibetan Plateau, an upper bound on viscosity of  $10^{16}$  Pa s is estimated based on the approximately linearly relationship between topographic slope and viscosity. However, the viscosity obtained from the Manyi earthquake ( $5 \times 10^{19}$  Pa s) is greater than value given by the channel model (see chapter 5). Moreover, this channel model is not favoured by other recent geodetic rheological studies of central Tibet (Doin *et al.*, 2015, Ryder *et al.*, 2014, Shen *et al.*, 2017). Magnetotelluric data

also show that deformation caused by channel flow in south-central Tibet is unlikely (Rippe and Unsworth, 2010). The viscosity estimations at the eastern margin based on topographic variations are more consistent, that most results between  $10^{18}$  and  $10^{21}$  Pa s (Table 7.1).

Table 7.1 Rheology estimations from various studies

| Year   | Magnitude | Location   | No. | Data          | Time       | Model        | Viscosity(Pa s)                         | Reference                    |
|--|-----------|------------|-----|---------------|------------|--------------|---|------------------------------|
| 1951   | 8.0       | Bengco     | 1   | InSAR         | 41–59 yr   | VR           | $>6-10 \times 10^{19}$                  | Ryder <i>et al.</i> (2014)   |
| 1973   | 7.6       | Luhuo      | 2   | Leveling      | 4–28 yr    | VR           | $10^{19}-10^{21}$                       | Zhang <i>et al.</i> (2009)   |
| 1997   | 7.6       | Manyi      | 3   | InSAR         | 0–4 yr     | AS/VR        | $4 \times 10^{18}$                      | Ryder <i>et al.</i> (2007)   |
|  |           |            | 4   | InSAR         | 0–4 yr     | VR           | $1.6 \times 10^{18}-1.2 \times 10^{21}$ | Yamasaki and Houseman (2012) |
|  |           |            | 5   | InSAR         | 0-12 yr    | AS/AS+VR     | $5 \times 10^{19}$                      | This thesis                  |
| 2001   | 7.8       | Kokoxili   | 6   | GPS           | 0–6 months | AS+VR        | $5 \times 10^{17}$                      | Shen <i>et al.</i> (2003)    |
|  |           |            | 7   | InSAR/GPS     | 0–5 yr     | VR           | $1 \times 10^{19}$                      | Ryder <i>et al.</i> (2011)   |
|  |           |            | 8   | InSAR         | 2–6 yr     | AS/VR/ AS+VR | $2 \times 10^{19}$                      | Wen <i>et al.</i> (2012)     |
|  |           |            | 9   | InSAR         | 2-9.2 yr   | VR           | $1 \times 10^{19}$                      | Zhao <i>et al.</i> (2018)    |
| 2008   | 6.4       | Nima-Gaize | 10  | InSAR         | 0–9 months | AS + VR      | $>3 \times 10^{17}$                     | Ryder <i>et al.</i> (2010)   |
| 2008   | 6.3       | Damxung    | 11  | InSAR         | ~1.6 yr    | VR           | $1 \times 10^{18}$                      | Bie <i>et al.</i> (2014)     |
| 2008   | 7.9       | Wenchuan   | 12  | GPS           | 0-14days   | AS + VR      | $4 \times 10^{17}$                      | Shao <i>et al.</i> (2011)    |
|  |           |            | 13  | InSAR/GPS     | 0–1.5 yr   | AS + VR      | $1 \times 10^{18}$                      | Huang <i>et al.</i> (2014)   |
|  |           |            | 14  | GPS           | 0-3 yr     | VR           | $>3 \times 10^{18}$                     | Xu <i>et al.</i> (2014)      |
|  |           |            | 15  | GPS           | 0–7 yr     | AS + VR      | $2 \times 10^{18}$                      | Diao <i>et al.</i> (2018)    |
| 2017   |           | Jiuzhaigou | 16  | InSAR         | 0–8 months | VR           | $>6 \times 10^{17}$                     | This thesis                  |
| Northern-central Tibet Plateau               |           |            |     | Fault slip    | Long term  |              | $10^{19}-2 \times 10^{21}$              | Hilley <i>et al.</i> (2005)  |
| Eastern Tibet Plateau                        |           |            |     | Topography    |            |              | $2 \times 10^{18}$                      | Clark <i>et al.</i> (2005)   |
| South-central Tibet Plateau (Siling Co Lake) |           |            |     | InSAR         | 19 yr      |              | $1-3 \times 10^{18}$                    | Doin <i>et al.</i> (2015)    |
|  |           |            |     | Shoreline     |            |              | $\leq (1-2) \times 10^{19}$             | Shi <i>et al.</i> (2015)     |
| Tibetan Plateau                              |           |            |     | Magnetotellur |            |              | $2.5 \times 10^{18}-3 \times 10^{20}$ , | Rippe and Unsworth (2010)    |

|  |  |                     |  |  |   |                               |
|--|--|---------------------|--|--|---|-------------------------------|
|  |  | ic data             |  |  | $1.7 \times 10^{17}$ - $1.2 \times 10^{20}$ |                               |
|  |  | Topography +<br>GPS |  |  | $>10^{19}$                                  | Cook and Royden (2008)        |
|  |  | Topography          |  |  | $10^{18}$ - $10^{19}$                       | Beaumont <i>et al.</i> (2001) |
|  |  | Topography          |  |  | $10^{18}$ , $10^{21}$ , $10^{16}$           | Clark and Royden (2000)       |
|  |  | Relief              |  |  | $10^{18}$ - $10^{21}$                       | Royden (1996)                 |



### 7.1.2 Spatial-temporal characteristics of the viscosities

The estimated lower crustal viscosities vary significantly across the Plateau. These estimations from the postseismic deformations show a spatially distributed pattern. In the flat central Plateau, on the time scale of years to decades, inferred lower crustal viscosities across most of the studies lie in the range of  $\sim 10^{19}$  Pa s. At the eastern margin of Tibet, the viscosity is more consistent at  $\sim 10^{18}$  Pa s. The regional heterogeneity indicates a relatively large spatial change in rheology of lower crust in Tibet. Recent earthquake tomography studies (Shen *et al.*, 2016, Zheng *et al.*, 2010) and magnetotelluric sounding (Bai *et al.*, 2010) indicate that a wide range of middle/lower crustal low-velocity layers may exist beneath the eastern margin of Tibet, where middle/lower crusts are hot and weak. This may explain why the viscosity of eastern Tibetan margin is slightly smaller than in other places of the Plateau.

If we plot all obtained effective lower crustal viscosity together, we can see that the estimated viscosity increases with time during the postseismic deformation process (Figure 7.2). The viscosities range obtained from various geodynamic models is generally wider than the range estimated from geodetic data (Table 7.1). Analysis of the postseismic response to the 1997 Manyi earthquake shows that lower viscosities are required to explain transient early deformations, while higher viscosities are necessary to explain sustained slow motion. After 20 years, the time-dependent viscosity of the Manyi earthquake may increase to  $\sim 10^{21}$  Pa s (see chapter 5). This value is at the same level of upper bound inferred by Hilley *et al.* (2005). For the Kokoxili earthquake and the Wenchuan earthquake, we can see that the viscosity estimated from a longer observation time span is generally larger than that obtained from a shorter period observation. The Burgers rheology, which transient viscosity is always smaller than steady-state viscosity, is also able to explain the postseismic observation in several case studies (e.g. Hearn *et al.*, 2009, Pollitz, 2005, Ryder *et al.*, 2011). This time-dependent behaviour of the viscosities may explain the difference

between the effective viscosities obtained from relatively short-term postseismic measurements and that from long-term geodynamic/geological models (e.g. Clark and Royden, 2000, Cook and Royden, 2008, Rippe and Unsworth, 2010).

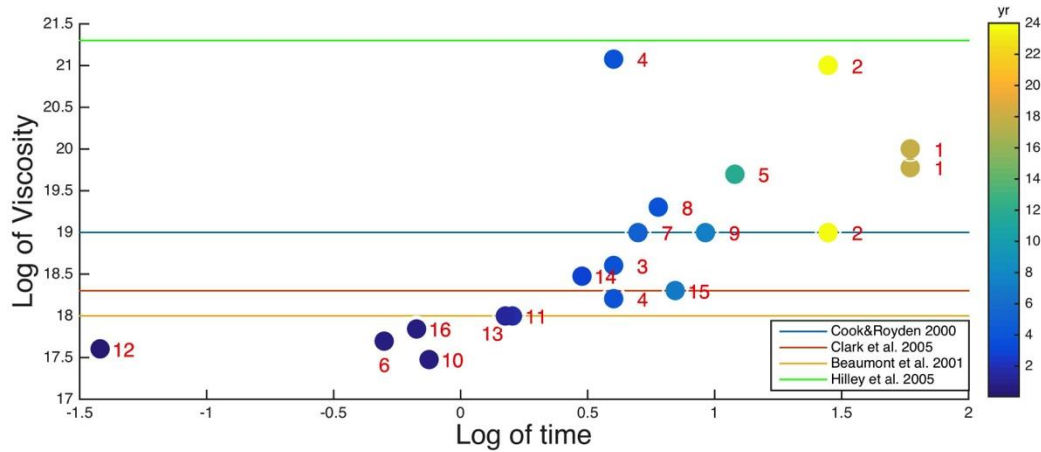


Figure 7.2 The circles with number represent the viscosities beneath the Tibet Plateau inferred by using postseismic geodetic data covering different time periods and for different earthquakes (list in Table 7.1). The colour lines represent the viscosities estimated from topography. The colour bar represents the length of the time window used for estimation.

## 7.2 Choosing mechanism(s) for postseismic deformation of strike-slip earthquakes

The postseismic deformation that is caused by large earthquakes can be explained by various mechanisms, such as poroelastic rebound, afterslip, viscoelastic relaxation, or nonlinear rheology (Table 7.2). Even for the same event, different researchers often favour a different explanation for postseismic deformation at different timescales. What is the factor that might affect our determination of the plausible postseismic deformation mechanism?

Table 7.2 Mechanisms of postseismic deformation for larger strike-slip earthquake

| Event       | Magnitude | Time span | Mechanism               | Reference                     |
|-------------|-----------|-----------|-------------------------|-------------------------------|
| Denali      | 7.9       | 19 months | VR                      | Pollitz (2005)                |
|             |           | 2 years   | VR/AS/Combination       | Freed <i>et al.</i> (2006)    |
|             |           | 2.5 years | VR/AS/Combination       | Biggs <i>et al.</i> (2009)    |
|             |           | 4.5 years | AS/Combination          | Johnson <i>et al.</i> (2009)  |
| Manyi       | 7.6       | 4 years   | VR/AS                   | Ryder <i>et al.</i> (2007)    |
|             |           | 4 years   | Depth-dependent VR      | Yamasaki and Houseman (2012)  |
|             |           | 12 years  | AS/Combination          | This thesis                   |
| KoKoxili    | 7.8       | 6 months  | Combination             | Shen <i>et al.</i> (2003)     |
|             |           | 5 years   | VR/AS                   | Ryder <i>et al.</i> (2011)    |
|             |           | 6 years   | VS/AS/Combination       | Wen <i>et al.</i> (2012)      |
|             |           | 7.2 years | VR                      | Zhao <i>et al.</i> (2018)     |
| Landers     | 7.3       | 4 years   | Poroelastic rebound     | Peltzer <i>et al.</i> (1998)  |
|             |           | 3 years   | VR                      | Pollitz <i>et al.</i> (2000)  |
|             |           | 7 years   | Poroelastic rebound +AS | Fialko (2004)                 |
| Hector Mine | 7.1       | 9 months  | VR                      | Pollitz <i>et al.</i> (2001)  |
|             |           | 3.2 years | VR                      | Freed and Bürgmann (2004)     |
|             |           | 9 years   | VR                      | Pollitz and Thatcher (2010)   |
| Izmit       | 7.5       | 87 days   | AS                      | Bürgmann <i>et al.</i> (2002) |
|             |           | 300 days  | AS                      | Hearn <i>et al.</i> (2002)    |
|             |           | 4 years   | AS and VR               | Hearn <i>et al.</i> (2009)    |
|             |           | 10 years  | AS                      | Cakir <i>et al.</i> (2012)    |
|             |           | 18 years  | AS                      | Cakir <i>et al.</i> (2017)    |
| Bengco      | 7.4       | 51 years  | VR                      | Ryder <i>et al.</i> (2014)    |
| Luhuo       | 7.5       | 28 year   | VR                      | Zhang <i>et al.</i> (2009)    |

Note: This table only lists earthquakes that magnitude is greater than 7.

Poroelastic rebound is restricted in both spatial and temporal aspects. For example, the largest poroelastic effect of the 1992 Landers earthquake was observed within 10km of the surface fracture and completed within several months after the earthquake (e.g. Peltzer *et al.*, 1996, Peltzer *et al.*, 1998). The deformation caused by poroelastic rebound occurs mainly in the vertical direction, within a few kilometres of the fault and in zones with abundant groundwater. As most postseismic deformation

of strike-slip earthquakes last much longer and cover a larger area, poroelastic rebound is unlikely to be a dominant effect in postseismic modelling.

Viscoelastic models are often proposed to explain long-term postseismic deformation. On the time scale of decades, viscoelastic relaxation can explain the postseismic deformation very well. For example, Ryder *et al.* (2014) used viscoelastic relaxation of the lower crust to explain the postseismic deformation of the two 1950's earthquakes. Since the uniform two-layer viscoelastic modelling produces a long wavelength signal, it can explain the widespread far-field deformation in many long-term postseismic observations. However, viscoelastic relaxation sometimes fails to describe the localized deformation pattern, especially for the transient short-term responses. For example, a single viscoelastic model is inadequate to explain the localized postseismic deformation of the Manyi earthquake (see chapter 5). Another example is the Izmit earthquake, for the first year, afterslip is the only mechanism that can explain the postseismic signal (Bürgmann *et al.*, 2002, Hearn *et al.*, 2002). Afterslip often occurs on the shallow parts of the faults within the sedimentary layer or down-dip of the coseismic rupture within the aseismic creep zone (Xu *et al.*, 2014). The surface deformation caused by afterslip has a localized pattern. Afterslip has not been often tested for the decadal timescale in previous studies. For the Manyi earthquake, the afterslip model can give more satisfactory reproduction of the 12 years observed data. Considering degrees of freedom for the viscoelastic models and afterslip model are entirely different, we tested a simplified afterslip model with fewer patches to reproduce the deformation in the Manyi earthquake. The result shows that the afterslip model can generally explain better the localized data not only due to the increase in the available model parameter (Figure S5.3). Therefore, afterslip is proposed to explain short-term postseismic deformation or localized deformation pattern and viscoelastic relaxation causes postseismic deformation with a longer time span.

Earthquake magnitude is another important factor that may affect the viscoelastic postseismic modelling. The viscoelastic postseismic deformations in moderate earthquakes sometimes are not visible, as such earthquake do not produce large enough stress to generate observable viscoelastic deformation. Therefore, the afterslip model is preferred in these moderate earthquakes. For the Bam earthquake ( $M=6.6$ ), 6 years of postseismic deformation does not show any viscoelastic-related signal (Wimpenny *et al.*, 2017). Another example is the Parkfield earthquake ( $M=6.0$ ), for which postseismic deformation is dominated by afterslip (e.g. Johnson *et al.*, 2006). Even 6 years after the earthquake, afterslip is still the dominant mechanism (Bruhat *et al.*, 2011). The optimal viscosity is not possible to be estimated directly due to the lack of long wavelength signal. But we can estimate a lower bound of viscosity instead to constrain the rheology. For example, there is no obvious postseismic signal in the Jiuzhaigou earthquake ( $M=6.5$ ), and as a consequence, we estimate a lower bound of viscosity by signal to noise ratio (see chapter 6).

Recently, an increasing number of researchers use a combined modelling approach to overcome the limitation of either mechanism (e.g. Biggs *et al.*, 2009, Feng *et al.*, 2018, Freed *et al.*, 2006, Wen *et al.*, 2012). In this combined model, the temporal evolution of the afterslip on the coseismic rupture or down-dip plane incorporates with viscoelastic relaxation in the lower crust. The afterslip plays a dominant role at the early stage of the postseismic, and the effect of the viscoelastic relaxation increases over time. In the Manyi earthquake, the combined model can slightly decrease the misfit of the overall data. The viscoelastic mechanism reproduces some far-field deformation and illustrates a great improvement at the far-field, which is complementary to the afterslip model (see chapter 5).



# Chapter 8

## Conclusion and outlook

This thesis utilizes available data sets to construct a long time series of surface deformation, which provides unique an opportunity to study the transition from the postseismic to the interseismic portion of the earthquake cycle in detail. The long time series is able to distinguish between afterslip and postseismic viscoelastic relaxation. In this thesis, afterslip has been tested for the decadal timescale postseismic deformation and explains the observed data with satisfactory result. The viscosities obtained from the case studies together with previous geodetic studies indicate the rheology has a relatively large spatial heterogeneity across the Tibetan Plateau. Here, I review the conclusions drawn in the two case studies presented in this thesis and give suggestions for future work.

### 8.1 Manyi earthquake

Chapter 5 was an investigation of postseismic deformation following the 1997 Manyi (Tibet) earthquake. Due to the arid climate and stable surface conditions of north-central Tibet, it is an ideal environment for us to use interferograms to investigate deformation. Our data cover the 12 years following the earthquake, much longer than the timespan of any previous studies. Nearly eighty interferograms of excellent coherence are selected for time series construction. Various models were tested against this time series. Nonlinear model (power-law) does not provide a good fit to the observations, therefore this model is not further discussed here. The tested models only concentrate on viscoelastic mechanisms (Maxwell, Standard linear solid and Burgers body) and afterslip. The Maxwell rheology (overall misfit = 2.23 cm) requires a larger increase in viscosity with time and is not able to explain the observed long time-series. Although the standard linear solid (overall misfit = 2.07 cm) and

Burgers body models (overall misfit = 2.16 cm) have two relaxation times, they cannot sufficiently reproduce localized deformation patterns. The distributions of viscoelastic modelling diffuse into the far field and the residuals tend to increase. The afterslip model (overall misfit = 1.77 cm) has the lowest misfit and explains well the temporal and spatial pattern of the observed deformation. The slip pattern is very stable through time even though the amount of slip is increasing over time. The patches with the highest slip for both coseismic and post-seismic deformation are located along the centre of the Manyi fault. This correlation suggests that afterslip is a physically plausible mechanism. We also test a simplified afterslip model with fewer patches which can reproduce the localized deformation pattern. This test shows that the decrease in misfit of the afterslip model is not only attributable to the increase in available model parameters but that it generally explains better the observed data. We also construct a combined model that considers the effects of both, afterslip and viscoelastic relaxation. The afterslip happens in the crust and viscoelastic relaxation in the underlying half-space during the postseismic period. The viscoelastic relaxation that occurs considering a model with an elastic layer thickness of 30 km over a viscoelastic half-space has a lower bound of viscosity of  $5 \times 10^{19}$  Pa s. In summary, the “pure” afterslip and the “combined” model are currently the most plausible models for the decadal years following the Manyi earthquake.

## 8.2 Jiuzhaigou earthquake

In Chapter 6, I investigated both the coseismic and postseismic phases of the 2017 Jiuzhaigou earthquake. The seismogenic fault of the Jiuzhaigou earthquake is previously unidentified and no surface rupture was found after the earthquake. I use the Markov-Chain Monte Carlo algorithm, incorporating the Metropolis-Hasting algorithm (Bagnardi and Hooper, 2018 and references therein), to obtain a uniform slip model from two tracks of Jiuzhaigou coseismic InSAR data. Subsequently, the steepest descend method (Wang *et al.*, 2013a) and Laplacian smoothing are used to solve slip distribution. The preferred coseismic model has a maximum slip of 1.1628



m at a depth of  $\sim 5$  km, and the total generated moment equals to  $M_w 6.41$ . This result is comparable to the magnitudes determined by different agencies. Most slip patches are located at a depth of 2–12 km with a little slip occurring on the top of the fault's surface. The focal mechanism of the Jiuzhaigou earthquake is similar to nearby historical earthquakes, which happened on the Huya fault. The Jiuzhaigou earthquake is probably the result of the north-westwards activity of the Huya Fault along the northern section. We also construct an 8 months' time-series of post-seismic deformation to explore the rheology. The constructed time-series reveals no obvious surface deformation associated with the fault, which means the surface deformation generated by fault creeping is smaller than the noise produced during the observation period. Therefore, we use a simple Maxwell model and signal-to-noise ratio (SNR) to seek a lower bound of the viscosity. Our preferred minimum possible viscosity of the underlying half-space is  $\sim 6 \times 10^{17}$  Pa s.

### 8.3 Outlook

This research has improved our understanding of two strike-slip events and the rheological structure of the Tibetan Plateau. The two earthquakes investigated in this thesis are only a very small sample. Due to the limitations of this study, a list of future investigations according to the case studies is suggested to improve our knowledge of the rheological structure and earthquake cycles.

Although several viscoelastic models have been tested for the 1997 Manyi earthquake sequence, they are all based on the uniform viscoelastic half-space beneath the elastic layer. However, other complex mechanisms, which have not yet been tested, may also be able to provide a good fit to the temporal characteristics of the time series. A more realistic (e.g. depth-based, lateral variation) model might be tested in the future. In the study of the Manyi earthquake, the detected deformation was obtained using only one InSAR track. The adjacent tracks can be considered in the future to check our preferred afterslip model and the combined model.

For the Jiuzhaigou earthquake, only limited data is available due to the short time span and low coherence of the data itself. A longer time series is needed to distinguish between different mechanisms. Also combining different mechanisms in the modelling is required but will only lead to results with better data sets. GPS data and a geological survey could be included to help us distinguish weak deformation signals.

In summary, discriminating the spatial distribution and temporal evolution of the postseismic deformation is a long-term work. As several satellites have launched during the past twenty years, we are able to have very long-time InSAR time series. A longer timespan of postseismic observation might enable us to isolate a specific rheology. I have studied one example as a pilot, but to generalise we need many more of these studies. In addition, modelling approaches with different physical processes other than those discussed in previous chapters are necessary. This inversion schemes will help us to investigate the difference between each underlying process, and shed a general light on viscosity of the lower crust and mantle.

# Supplementary

## Tables and figure in Chapter 4:

Table S4.1 The synthetic crust structure information used in the section 4.1.3.

|         | Vp (km/s) | Vs(km/s) | rho(g/cm3) | Thickness(km) |
|---------|-----------|----------|------------|---------------|
| crust 1 | 6.00      | 3.52     | 2.72       | 15            |
| crust 2 | 6.30      | 3.68     | 2.79       | $\infty$      |

Note: Vp is the velocity of P wave, Vs is the velocity of S wave and rho is the rock density.

Table S4.2 The crust structure information used in the layered elastic model.(section 4.2.1.2)

|                  | Vp (km/s) | Vs(km/s) | rho(g/cm3) | Thickness(km) |
|------------------|-----------|----------|------------|---------------|
| crust 1          | 6.00      | 3.52     | 2.72       | 29            |
| crust 2          | 6.30      | 3.68     | 2.79       | 46            |
| crust 3          | 6.60      | 3.82     | 2.85       | 64            |
| uppermost mantle | 8.21      | 4.55     | 3.38       |               |

Note: Vp is the velocity of P wave, Vs is the velocity of S wave and rho is the rock density. The four layers of crust is obtained at point (Latitude 33, Longitude 88) in the database of Crust1.0.



## Figures in Chapter 5:

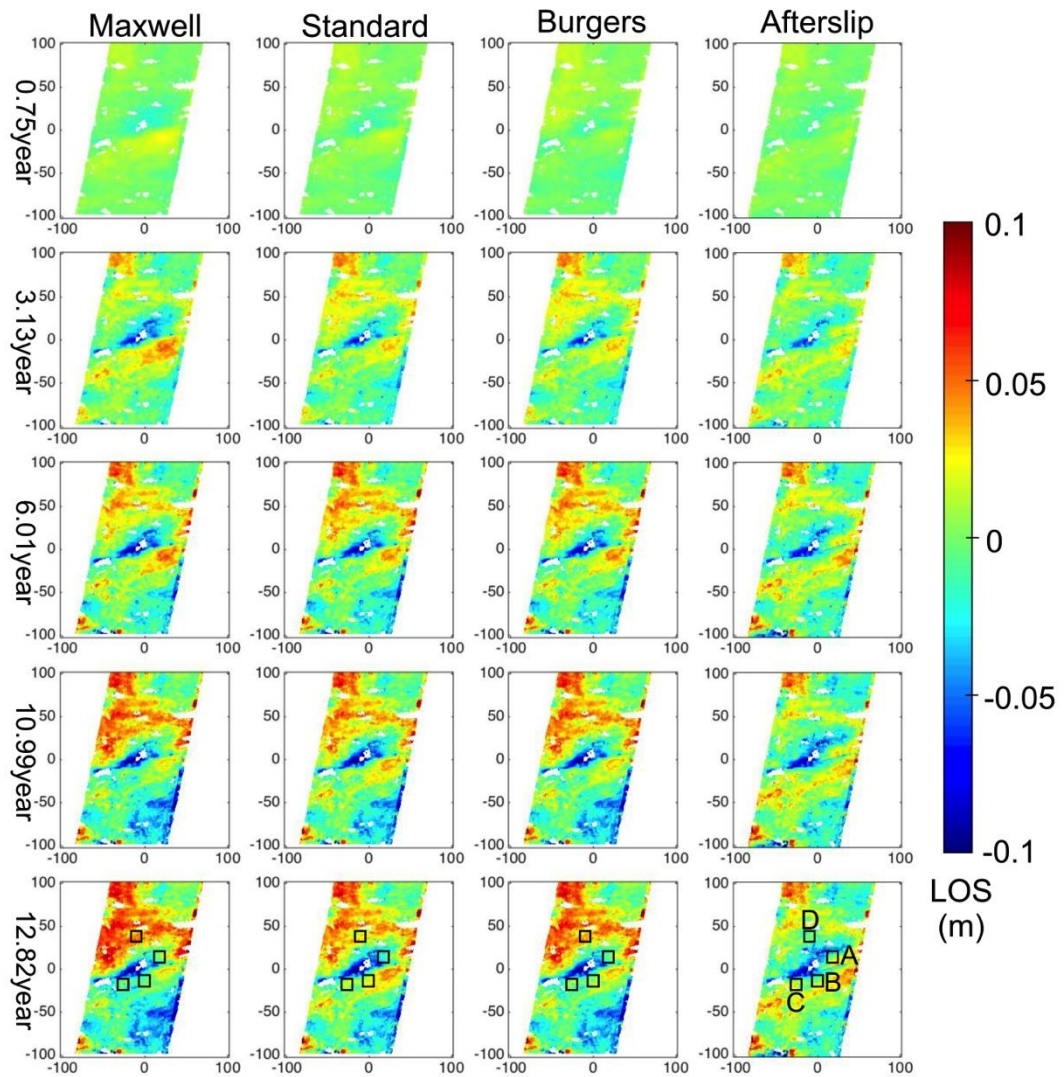


Figure S5.1 Residuals for each model from early to late time period (calculated as the model minus data). Here, only 4 dates are presented to show the residual change tendency. The black squares show the location of Patch A, B, C and D. The mean displacements of these patches are used in the discussion to explore the temporal behaviour of each model.

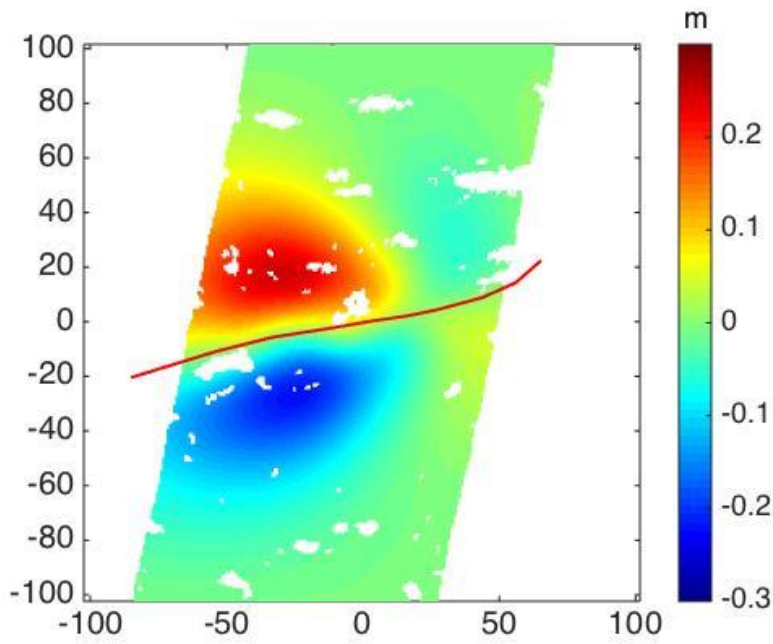


Figure S5.2 Range change predicted by non-linear model at 11<sup>th</sup> year after the earthquake. The spatial deformation pattern bears little similarity to that of the time-series (Figure 3). Red line marks position of fault.

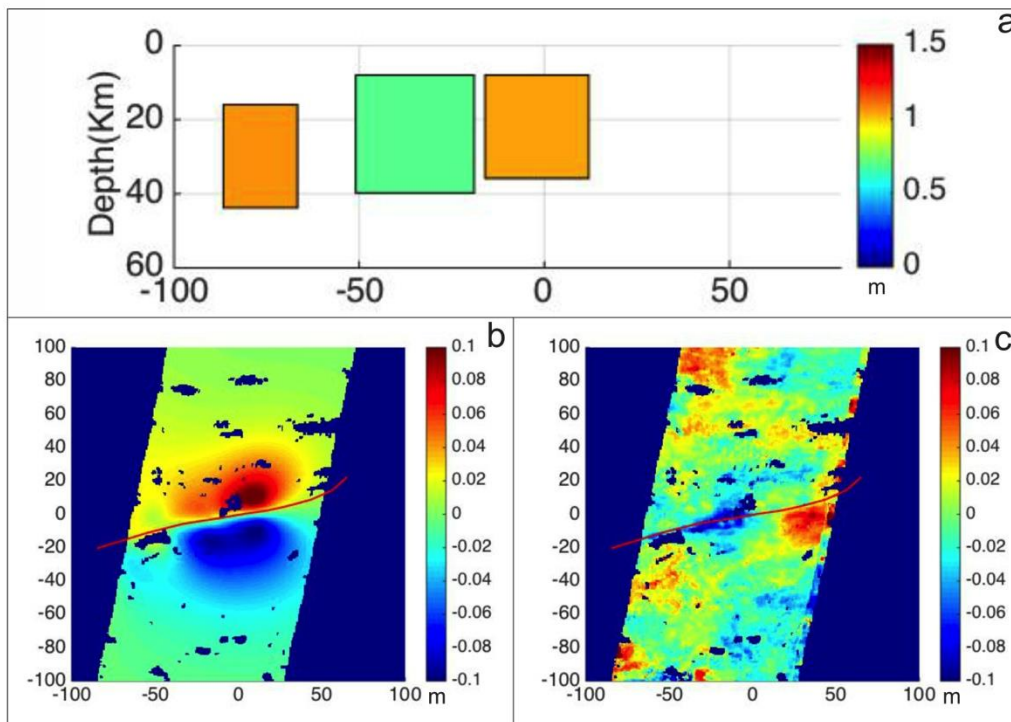


Figure S5.3 The three patches afterslip model inversion results. (a) The slip distributions from three patch afterslip inversions after 12 years of earthquake. (b) Predicted surface deformation by this simplify model. (c)Corresponding residual.

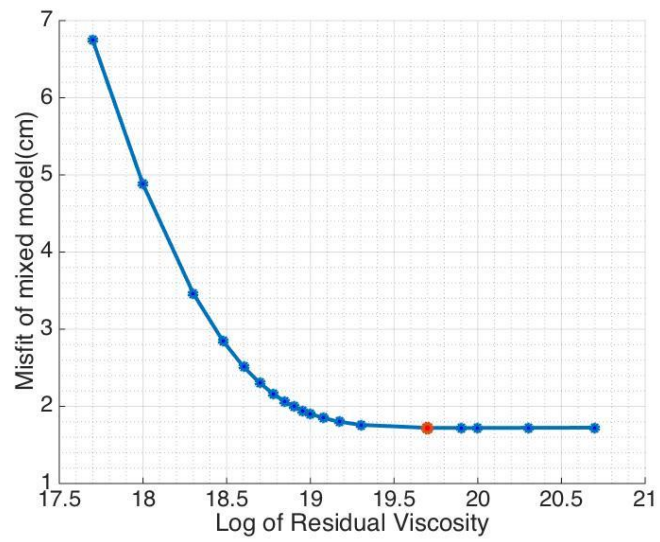


Figure S5.4 Trade off curve between residual viscosity of viscoelastic model and misfit of the combined model. The thickness of elastic lid is 30km. The viscosity is  $5 \times 10^{19}$  Pa s of the red point, which model sketch map and displacement shows in Figure 5.9 and Figure 5.6.





## Figures in Chapter 6:

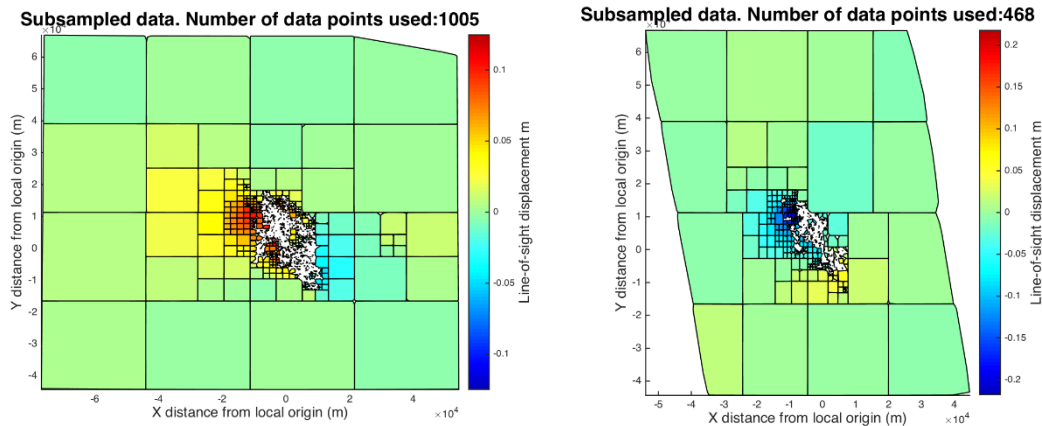


Figure S6.1 Down-sampled interferogram data of the earthquake area using the quadtree decomposition algorithm. Left panels: track 62, right panels: track 128.

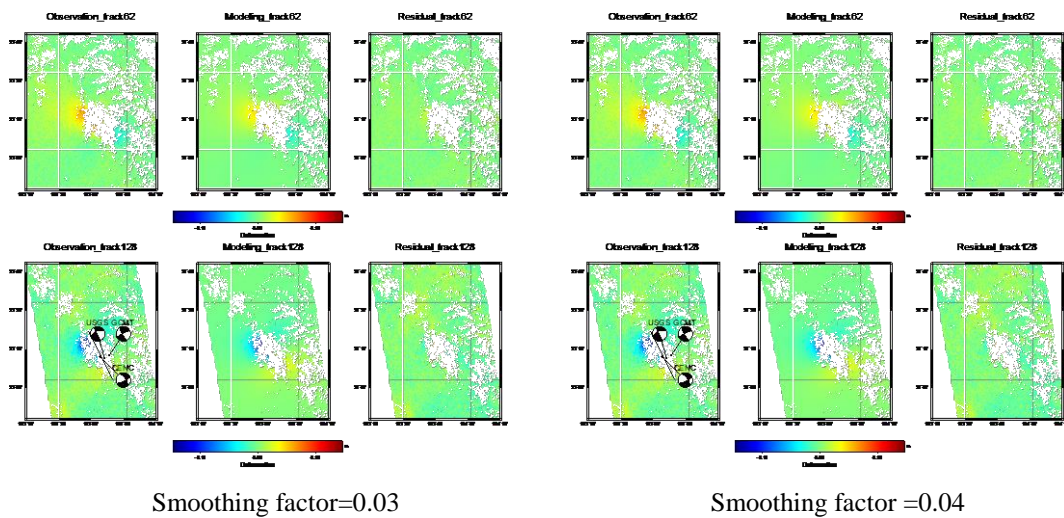


Figure S6.2 Recovered surface deformation by adjacent smoothing factor value.

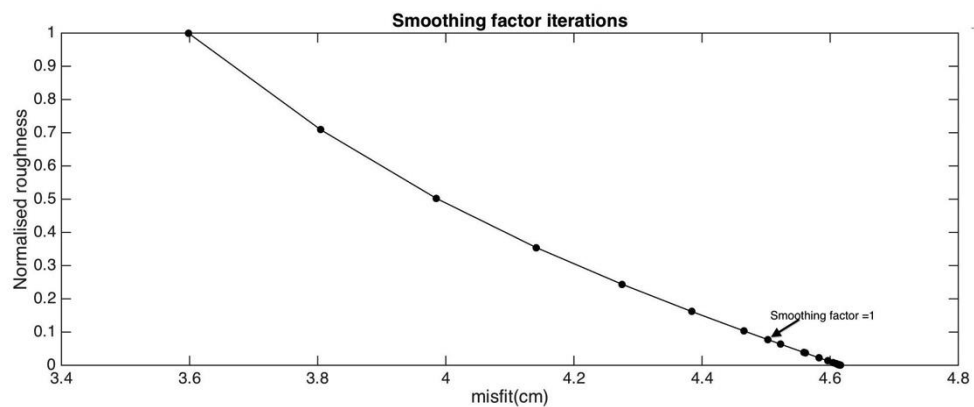


Figure S6.3 Normalised roughness plotted against misfit for different smoothing factors in time-series matrix. The point marks the smoothing factor of 1, which is used in time-series construction.

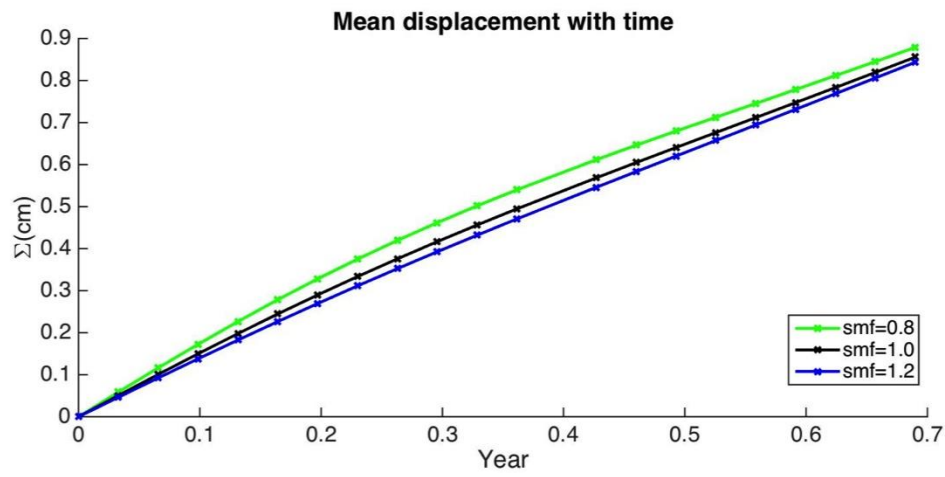


Figure S6.4 Mean displacement with time for different smoothing factor. smf is the abbreviation for the smoothing factor.

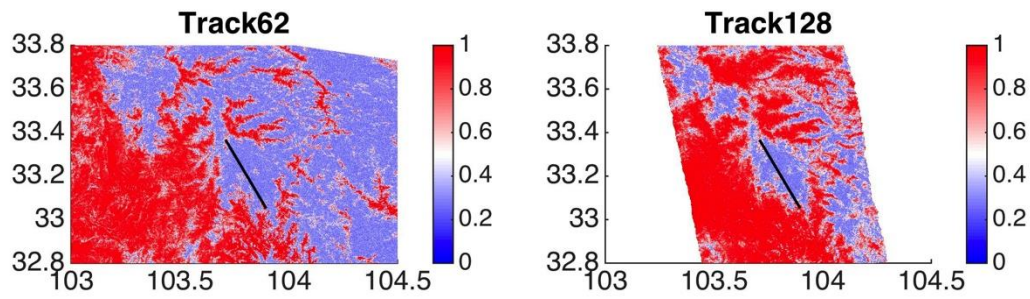


Figure S6.5 The coherence figure of the Jiuzhaigou coseismic interferograms. The red colour indicates high coherence and the blue colour represents are considered, resulting in reduced pixel density.

# Bibliography

- Agram, P., Jolivet, R., Riel, B., Lin, Y., Simons, M., Hetland, E., Doin, M.P. & Lasserre, C., 2013. New radar interferometric time series analysis toolbox released, *Eos, Transactions American Geophysical Union*, 94, 69-70.
- Avouac, J.P. & Tapponnier, P., 1993. Kinematic Model of Active Deformation in Central-Asia, *Geophys. Res. Lett.*, 20, 895-898.
- Bagnardi, M. & Hooper, A., 2018. Inversion of surface deformation data for rapid estimates of source parameters and uncertainties: a Bayesian approach, *Geochem. Geophys. Geosyst.*
- Bai, D.H., Unsworth, M.J., Meju, M.A., Ma, X.B., Teng, J.W., Kong, X.R., Sun, Y., Sun, J., Wang, L.F., Jiang, C.S., Zhao, C.P., Xiao, P.F. & Liu, M., 2010. Crustal deformation of the eastern Tibetan plateau revealed by magnetotelluric imaging, *Nat. Geosci.*, 3, 358-362.
- Barbot, S. & Fialko, Y., 2010. A unified continuum representation of post-seismic relaxation mechanisms: semi-analytic models of afterslip, poroelastic rebound and viscoelastic flow, *Geophys. J. Int.*, 182, 1124-1140.
- Barbot, S., Fialko, Y. & Bock, Y., 2009. Postseismic deformation due to the M-w 6.0 2004 Parkfield earthquake: Stress-driven creep on a fault with spatially variable rate-and-state friction parameters, *J Geophys Res-Sol Ea*, 114.
- Beaumont, C., Jamieson, R.A., Nguyen, M.H. & Lee, B., 2001. Himalayan tectonics explained by extrusion of a low-viscosity crustal channel coupled to focused surface denudation, *Nature*, 414, 738-742.
- Beaumont, C., Jamieson, R.A., Nguyen, M.H. & Medvedev, S., 2004. Crustal channel flows: 1. Numerical models with applications to the tectonics of the Himalayan-Tibetan orogen, *J Geophys Res-Sol Ea*, 109.
- Bekaert, D.P.S., Hooper, A. & Wright, T.J., 2015a. A spatially variable power law tropospheric correction technique for InSAR data, *J Geophys Res-Sol Ea*, 120, 1345-1356.
- Bekaert, D.P.S., Walters, R.J., Wright, T.J., Hooper, A.J. & Parker, D.J., 2015b. Statistical comparison of InSAR tropospheric correction techniques, *Remote Sens Environ*, 170, 40-47.
- Bell, M.A., Elliott, J.R. & Parsons, B.E., 2011. Interseismic strain accumulation across the Manyi fault (Tibet) prior to the 1997 M-w 7.6 earthquake, *Geophys. Res. Lett.*, 38.
- Bennartz, R. & Fischer, J., 2001. Retrieval of columnar water vapour over land from backscattered solar radiation using the Medium Resolution Imaging Spectrometer, *Remote Sens Environ*, 78, 274-283.
- Berardino, P., Fornaro, G., Lanari, R. & Sansosti, E., 2002. A new algorithm for surface deformation monitoring based on small baseline differential SAR interferograms, *Ieee T Geosci Remote*, 40, 2375-2383.

- Berrisford, P., Dee, D., Poli, P., Brugge, R., Fielding, K., Fuentes, M., Kallberg, P., Kobayashi, S., Uppala, S. & Simmons, A., 2011a. The ERA-Interim archive, version 2.0.
- Berrisford, P., Kallberg, P., Kobayashi, S., Dee, D., Uppala, S., Simmons, A.J., Poli, P. & Sato, H., 2011b. Atmospheric conservation properties in ERA-Interim, *Q. J. Roy. Meteorol. Soc.*, 137, 1381-1399.
- Bevis, M., Businger, S., Chiswell, S., Herring, T.A., Anthes, R.A., Rocken, C. & Ware, R.H., 1994. Gps Meteorology - Mapping Zenith Wet Delays onto Precipitable Water, *J. Appl. Meteorol.*, 33, 379-386.
- Bevis, M., Businger, S., Herring, T.A., Rocken, C., Anthes, R.A. & Ware, R.H., 1992. Gps Meteorology - Remote-Sensing of Atmospheric Water-Vapor Using the Global Positioning System, *J Geophys Res-Atmos*, 97, 15787-15801.
- Bezy, J.L., Delwart, S. & Rast, M., 2000. MERIS - A new generation of ocean-colour sensor onboard Envisat, *Esa Bull-Eur Space*, 48-56.
- Bie, L.D., Ryder, I., Nippres, S.E.J. & Burgmann, R., 2014. Coseismic and post-seismic activity associated with the 2008 M-w 6.3 Damxung earthquake, Tibet, constrained by InSAR, *Geophys. J. Int.*, 196, 788-803.
- Biggs, J., Burgmann, R., Freymueller, J.T., Lu, Z., Parsons, B., Ryder, I., Schmalzle, G. & Wright, T., 2009. The postseismic response to the 2002 M 7.9 Denali Fault earthquake: constraints from InSAR 2003-2005, *Geophys. J. Int.*, 176, 353-367.
- Biggs, J., Wright, T., Lu, Z. & Parsons, B., 2007. Multi-interferogram method for measuring interseismic deformation: Denali fault, Alaska, *Geophys. J. Int.*, 170, 1165-1179.
- Blanpied, M., Lockner, D. & Byerlee, J., 1991. Fault stability inferred from granite sliding experiments at hydrothermal conditions, *Geophys. Res. Lett.*, 18, 609-612.
- Bourg, L. & Delwart, S., 2006. MERIS instrument calibration. in *Second MERIS and AATSR Calibration and Geophysical Validation Workshop, Frascati, Italy*, pp. 20-24.
- Brace, W.F. & Byerlee, J.D., 1966. Stick-Slip as a Mechanism for Earthquakes, *Science*, 153, 990-&.
- Bruhat, L., Barbot, S. & Avouac, J.P., 2011. Evidence for postseismic deformation of the lower crust following the 2004 Mw6.0 Parkfield earthquake, *J Geophys Res-Sol Ea*, 116.
- Bürgmann, R. & Dresen, G., 2008. Rheology of the lower crust and upper mantle: Evidence from rock mechanics, geodesy, and field observations, *Annu Rev Earth Pl Sc*, 36, 531-567.
- Bürgmann, R., Ergintav, S., Segall, P., Hearn, E.H., McClusky, S., Reilinger, R.E., Woith, H. & Zschau, J., 2002. Time-dependent distributed afterslip on and deep below the Izmit earthquake rupture, *Bull. Seismol. Soc. Am.*, 92, 126-137.
- Byerlee, J., 1978. Friction of Rocks, *Pure Appl Geophys*, 116, 615-626.
- Cakir, Z., Aslan, G., Cetin, S., Dogan, U., Ergintav, S., Lasserre, C., Renard, F. &

- Reilinger, R., 2017. Postseismic deformation of the 1999 Izmit Earthquake (Turkey)-the longest recorded afterslip on a major continental fault. *in AGU Fall Meeting Abstracts*.
- Cakir, Z., Ergintav, S., Ozener, H., Dogan, U., Akoglu, A.M., Meghraoui, M. & Reilinger, R., 2012. Onset of aseismic creep on major strike-slip faults, *Geology*, 40, 1115-1118.
- Carter, N.L. & Avelalle.Hg, 1970. High Temperature Flow of Dunite and Peridotite, *Geol. Soc. Am. Bull.*, 81, 2181-&.
- Cavalié, O., Doin, M.P., Lasserre, C. & Briole, P., 2007. Ground motion measurement in the Lake Mead area, Nevada, by differential synthetic aperture radar interferometry time series analysis: Probing the lithosphere rheological structure, *J Geophys Res-Sol Ea*, 112.
- Clark, M.K., Bush, J.W.M. & Royden, L.H., 2005. Dynamic topography produced by lower crustal flow against rheological strength heterogeneities bordering the Tibetan Plateau, *Geophys. J. Int.*, 162, 575-590.
- Clark, M.K. & Royden, L.H., 2000. Topographic ooze: Building the eastern margin of Tibet by lower crustal flow, *Geology*, 28, 703-706.
- Cook, K.L. & Royden, L.H., 2008. The role of crustal strength variations in shaping orogenic plateaus, with application to Tibet, *J Geophys Res-Sol Ea*, 113.
- Copley, A., 2014. Postseismic afterslip 30 years after the 1978 Tabas-e-Golshan (Iran) earthquake: observations and implications for the geological evolution of thrust belts, *Geophys. J. Int.*, 197, 665-679.
- Copley, A. & Reynolds, K., 2014. Imaging topographic growth by long - lived postseismic afterslip at Sefidabeh, east Iran, *Tectonics*, 33, 330-345.
- Davis, J.L., Herring, T.A., Shapiro, I.I., Rogers, A.E.E. & Elgered, G., 1985. Geodesy by Radio Interferometry - Effects of Atmospheric Modeling Errors on Estimates of Baseline Length, *Radio Sci*, 20, 1593-1607.
- Dee, D.P., Uppala, S.M., Simmons, A.J., Berrisford, P., Poli, P., Kobayashi, S., Andrae, U., Balmaseda, M.A., Balsamo, G., Bauer, P., Bechtold, P., Beljaars, A.C.M., van de Berg, L., Bidlot, J., Bormann, N., Delsol, C., Dragani, R., Fuentes, M., Geer, A.J., Haimberger, L., Healy, S.B., Hersbach, H., Holm, E.V., Isaksen, L., Kallberg, P., Kohler, M., Matricardi, M., McNally, A.P., Monge-Sanz, B.M., Morcrette, J.J., Park, B.K., Peubey, C., de Rosnay, P., Tavolato, C., Thepaut, J.N. & Vitart, F., 2011. The ERA-Interim reanalysis: configuration and performance of the data assimilation system, *Q. J. Roy. Meteorol. Soc.*, 137, 553-597.
- Deng, J.S., Gurnis, M., Kanamori, H. & Hauksson, E., 1998. Viscoelastic flow in the lower crust after the 1992 Landers, Californial earthquake, *Science*, 282, 1689-1692.
- Deng, Q.D., Cheng, S.P., Ma, J. & Du, P., 2014. Seismic activities and earthquake potential in the Tibetan Plateau, *Chinese J Geophys-Ch*, 57, 2025-2042.
- Diao, F., Wang, R., Wang, Y., Xiong, X. & Walter, T.R., 2018. Fault behavior and lower crustal rheology inferred from the first seven years of postseismic

- GPS data after the 2008 Wenchuan earthquake, *Earth Planet. Sci. Lett.*, 495, 202-212.
- Diao, F.Q., Xiong, X. & Wang, R.J., 2011. Mechanisms of Transient Postseismic Deformation Following the 2001 Mw 7.8 Kunlun (China) Earthquake, *Pure Appl Geophys*, 168, 767-779.
- Dieterich, J.H., 1978. Time-Dependent Friction and Mechanics of Stick-Slip, *Pure Appl Geophys*, 116, 790-806.
- Ding, X.L., Li, Z.W., Zhu, J.J., Feng, G.C. & Long, J.P., 2008. Atmospheric effects on InSAR measurements and their mitigation, *Sensors-Basel*, 8, 5426-U5421.
- Doin, M.P., Lasserre, C., Peltzer, G., Cavalie, O. & Doubre, C., 2009. Corrections of stratified tropospheric delays in SAR interferometry: Validation with global atmospheric models, *J Appl Geophys*, 69, 35-50.
- Doin, M.P., Twardzik, C., Ducret, G., Lasserre, C., Guillaso, S. & Sun, J.B., 2015. InSAR measurement of the deformation around Siling Co Lake: Inferences on the lower crust viscosity in central Tibet, *J Geophys Res-Sol Ea*, 120, 5290-5310.
- Dziewonski, A., Chou, T.A. & Woodhouse, J., 1981. Determination of earthquake source parameters from waveform data for studies of global and regional seismicity, *J. Geophys. Res.*, 86, 2825-2852.
- Ekström, G., Nettles, M. & Dziewoński, A., 2012. The global CMT project 2004–2010: Centroid-moment tensors for 13,017 earthquakes, *Phys. Earth Planet. Inter.*, 200, 1-9.
- Elliott, J.R., Biggs, J., Parsons, B. & Wright, T.J., 2008. InSAR slip rate determination on the Altyn Tagh Fault, northern Tibet, in the presence of topographically correlated atmospheric delays, *Geophys. Res. Lett.*, 35.
- England, P. & Mckenzie, D., 1982. A Thin Viscous Sheet Model for Continental Deformation, *Geophys. J. Roy. Astron. Soc.*, 70, 295-321.
- England, P. & Molnar, P., 1997. Active deformation of Asia: From kinematics to dynamics, *Science*, 278, 647-650.
- Fang, L., Wu, J., Su, J., Wang, M., Jiang, C., Fan, L., Wang, W., Wang, C. & Tan, X., 2018. Relocation of mainshock and aftershock sequence of the M s 7.0 Sichuan Jiuzhaigou earthquake, *Chin. Sci. Bull.*, 63, 649-662.
- Farr, T.G., Rosen, P.A., Caro, E., Crippen, R., Duren, R., Hensley, S., Kobrick, M., Paller, M., Rodriguez, E., Roth, L., Seal, D., Shaffer, S., Shimada, J., Umland, J., Werner, M., Oskin, M., Burbank, D. & Alsdorf, D., 2007. The shuttle radar topography mission, *Reviews of Geophysics*, 45.
- Feng, M., Bie, L. & Rietbrock, A., 2018. Probing the rheology of continental faults: decade of post-seismic InSAR time-series following the 1997 Manyi (Tibet) earthquake, *Geophys. J. Int.*, 215, 600-613.
- Ferretti, A., Monti Guarnieri, A., Prati, C., Rocca, F. & Massonnet, D., 2007. *INSAR Principles A*, edn, Vol., pp. Pages, ESA publications.
- Ferretti, A., Prati, C. & Rocca, F., 2001. Permanent scatterers in SAR interferometry, *Ieee T Geosci Remote*, 39, 8-20.

- Fialko, Y., 2004. Evidence of fluid - filled upper crust from observations of postseismic deformation due to the 1992 Mw7.3 Landers earthquake, *J. Geophys. Res.*, 109.
- Fielding, E.J., Lundgren, P.R., Burgmann, R. & Funning, G.J., 2009. Shallow fault-zone dilatancy recovery after the 2003 Bam earthquake in Iran, *Nature*, 458, 64-68.
- Flesch, L.M., Haines, A.J. & Holt, W.E., 2001. Dynamics of the India-Eurasia collision zone, *J Geophys Res-Sol Ea*, 106, 16435-16460.
- Freed, A.M., 2007. Afterslip (and only afterslip) following the 2004 Parkfield, California, earthquake, *Geophys. Res. Lett.*, 34.
- Freed, A.M. & Bürgmann, R., 2004. Evidence of power-law flow in the Mojave desert mantle, *Nature*, 430, 548-551.
- Freed, A.M., Burgmann, R., Calais, E., Freymueller, J. & Hreinsdottir, S., 2006. Implications of deformation following the 2002 Denali, Alaska, earthquake for postseismic relaxation processes and lithospheric rheology, *J Geophys Res-Sol Ea*, 111.
- Funning, G.J., Parsons, B. & Wright, T.J., 2007. Fault slip in the 1997 Manyi, Tibet earthquake from linear elastic modelling of InSAR displacements, *Geophys. J. Int.*, 169, 988-1008.
- Gan, W.J., Zhang, P.Z., Shen, Z.K., Niu, Z.J., Wang, M., Wan, Y.G., Zhou, D.M. & Cheng, J., 2007. Present-day crustal motion within the Tibetan Plateau inferred from GPS measurements, *J Geophys Res-Sol Ea*, 112.
- Gonzalez, P.J., Bagnardi, M., Hooper, A.J., Larsen, Y., Marinkovic, P., Samsonov, S.V. & Wright, T.J., 2015. The 2014-2015 eruption of Fogo volcano: Geodetic modeling of Sentinel-1 TOPS interferometry, *Geophys. Res. Lett.*, 42, 9239-9246.
- Gourmelen, N. & Amelung, F., 2005. Postseismic mantle relaxation in the Central Nevada Seismic Belt, *Science*, 310, 1473-1476.
- Gray, A.L., Mattar, K.E. & Sofko, G., 2000. Influence of ionospheric electron density fluctuations on satellite radar interferometry, *Geophys. Res. Lett.*, 27, 1451-1454.
- Hanssen, R.F., 2001. *Radar interferometry: data interpretation and error analysis*, edn, Vol. 2, pp. Pages, Springer Science & Business Media.
- Hearn, E.H., Burgmann, R. & Reilinger, R.E., 2002. Dynamics of Izmit earthquake postseismic deformation and loading of the Duzce earthquake hypocenter, *Bull. Seismol. Soc. Am.*, 92, 172-193.
- Hearn, E.H., McClusky, S., Ergintav, S. & Reilinger, R.E., 2009. Izmit earthquake postseismic deformation and dynamics of the North Anatolian Fault Zone, *J Geophys Res-Sol Ea*, 114.
- Hetland, E.A. & Hager, B.H., 2006. The effects of rheological layering on post-seismic deformation, *Geophys. J. Int.*, 166, 277-292.
- Hetland, E.A. & Zhang, G., 2014. Effect of shear zones on post-seismic deformation with application to the 1997 M-w 7.6 Manyi earthquake, *Geophys. J. Int.*, 198, 259-269.

- Hilley, G.E., Bürgmann, R., Zhang, P.Z. & Molnar, P., 2005. Bayesian inference of plastosphere viscosities near the Kunlun Fault, northern Tibet, *Geophys. Res. Lett.*, 32.
- Hooper, A., Pietrzak, J., Simons, W., Cui, H., Riva, R., Naeije, M., van Scheltinga, A.T., Schrama, E., Stelling, G. & Socquet, A., 2013. Importance of horizontal seafloor motion on tsunami height for the 2011 M-w=9.0 Tohoku-Oki earthquake, *Earth Planet. Sci. Lett.*, 361, 469-479.
- Hu, C., Ren, J. & Yang, P., 2017. Discussion on the compression-shear activity of the Tazang fault in East Kunlun and uplift of plateau, *Acta Geol. Sin.*, 91, 1401-1415.
- Hu, S.B., He, L.J. & Wang, J.Y., 2000. Heat flow in the continental area of China: a new data set, *Earth Planet. Sci. Lett.*, 179, 407-419.
- Huang, M.H., Burgmann, R. & Freed, A.M., 2014. Probing the lithospheric rheology across the eastern margin of the Tibetan Plateau, *Earth Planet. Sci. Lett.*, 396, 88-96.
- Hughes, K.L.H., Masterlark, T. & Mooney, W.D., 2010. Poroelastic stress-triggering of the 2005 M8.7 Nias earthquake by the 2004 M9.2 Sumatra-Andaman earthquake, *Earth Planet. Sci. Lett.*, 293, 289-299.
- Hussain, E., Wright, T.J., Walters, R.J., Bekaert, D., Hooper, A. & Houseman, G.A., 2016. Geodetic observations of postseismic creep in the decade after the 1999 Izmit earthquake, Turkey: Implications for a shallow slip deficit, *J. Geophys. Res.*, 121, 2980-3001.
- Ingleby, T. & Wright, T., 2017. Omori - like decay of postseismic velocities following continental earthquakes, *Geophys. Res. Lett.*, 44, 3119-3130.
- Jiang, M., Galvé, A., Hirn, A., De Voogd, B., Laigle, M., Su, H., Diaz, J., Lépine, J.-C. & Wang, Y., 2006. Crustal thickening and variations in architecture from the Qaidam basin to the Qang Tang (North-Central Tibetan Plateau) from wide-angle reflection seismology, *Tectonophysics*, 412, 121-140.
- Johnson, K.M., Bürgmann, R. & Freymueller, J.T., 2009. Coupled afterslip and viscoelastic flow following the 2002 Denali Fault, Alaska earthquake, *Geophys. J. Int.*, 176, 670-682.
- Johnson, K.M., Burgmann, R. & Larson, K., 2006. Frictional properties on the San Andreas fault near Parkfield, California, inferred from models of afterslip following the 2004 earthquake, *Bull. Seismol. Soc. Am.*, 96, S321-S338.
- Jolivet, R., Grandin, R., Lasserre, C., Doin, M.P. & Peltzer, G., 2011. Systematic InSAR tropospheric phase delay corrections from global meteorological reanalysis data, *Geophys. Res. Lett.*, 38.
- Jones, L.M., Han, W.B., Hauksson, E., Jin, A.S., Zhang, Y.G. & Luo, Z.L., 1984. Focal Mechanisms and Aftershock Locations of the Songpan Earthquakes of August 1976 in Sichuan, China, *J. Geophys. Res.*, 89, 7697-7707.
- Jónsson, S., Segall, P., Pedersen, R. & Björnsson, G., 2003. Post-earthquake ground movements correlated to pore-pressure transients, *Nature*, 424, 179-183.
- Jónsson, S., Zebker, H., Segall, P. & Amelung, F., 2002. Fault slip distribution of



- the 1999 M-w 7.1 Hector Mine, California, earthquake, estimated from satellite radar and GPS measurements, *Bull. Seismol. Soc. Am.*, 92, 1377-1389.
- Katagi, T., Yoshioka, S. & Hashimoto, M., 2008. Influence of temperature- and depth-dependent viscosity structures on postseismic deformation predictions for the large 1946 Nankai subduction zone earthquake, *Tectonophysics*, 454, 1-13.
- Kirby, E., Whipple, K.X., Burchfiel, B.C., Tang, W.Q., Berger, G., Sun, Z.M. & Chen, Z.L., 2000. Neotectonics of the Min Shan, China: Implications for mechanisms driving Quaternary deformation along the eastern margin of the Tibetan Plateau, *Geol. Soc. Am. Bull.*, 112, 375-393.
- Laske, G., Masters, G., Ma, Z. & Pasyanos, M., 2013. Update on CRUST1. 0—A 1-degree global model of Earth's crust. in *Geophys. Res. Abstr.*, pp. 2658EGU General Assembly Vienna, Austria.
- Li, H.Y., Su, W., Wang, C.Y. & Huang, Z.X., 2009a. Ambient noise Rayleigh wave tomography in western Sichuan and eastern Tibet, *Earth Planet. Sci. Lett.*, 282, 201-211.
- Li, Z.H., Fielding, E.J., Cross, P. & Muller, J.P., 2006. Interferometric synthetic aperture radar atmospheric correction: GPS topography-dependent turbulence model, *J Geophys Res-Sol Ea*, 111.
- Li, Z.H., Fielding, E.J., Cross, P. & Preusker, R., 2009b. Advanced InSAR atmospheric correction: MERIS/MODIS combination and stacked water vapour models, *Int J Remote Sens*, 30, 3343-3363.
- Li, Z.H., Muller, J.P., Cross, P. & Fielding, E.J., 2005. Interferometric synthetic aperture radar (InSAR) atmospheric correction: GPS, moderate resolution Imaging spectroradiometer (MODIS), and InSAR integration, *J Geophys Res-Sol Ea*, 110.
- Lopez-Quiroz, P., Doin, M.P., Tupin, F., Briole, P. & Nicolas, J.M., 2009. Time series analysis of Mexico City subsidence constrained by radar interferometry, *J Appl Geophys*, 69, 1-15.
- Lyons, S. & Sandwell, D., 2003. Fault creep along the southern San Andreas from interferometric synthetic aperture radar, permanent scatterers, and stacking, *J. Geophys. Res.*, 108.
- Marone, C.J., Scholtz, C.H. & Bilham, R., 1991. On the Mechanics of Earthquake Afterslip, *J Geophys Res-Solid*, 96, 8441-8452.
- Massonnet, D., Feigl, K., Rossi, M. & Adragna, F., 1994. Radar Interferometric Mapping of Deformation in the Year after the Landers Earthquake, *Nature*, 369, 227-230.
- Massonnet, D. & Feigl, K.L., 1995. Discrimination of Geophysical Phenomena in Satellite Radar Interferograms, *Geophys. Res. Lett.*, 22, 1537-1540.
- Massonnet, D. & Feigl, K.L., 1998. Radar interferometry and its application to changes in the earth's surface, *Reviews of Geophysics*, 36, 441-500.
- Massonnet, D., Rossi, M., Carmona, C., Adragna, F., Peltzer, G., Feigl, K. & Rabaut, T., 1993. The Displacement Field of the Landers Earthquake Mapped by

- Radar Interferometry, *Nature*, 364, 138-142.
- Masterlark, T. & Wang, H.F., 2002. Transient stress-coupling between the 1992 Landers and 1999 Hector Mine, California, earthquakes, *Bull. Seismol. Soc. Am.*, 92, 1470-1486.
- McClusky, S., Balassanian, S., Barka, A., Demir, C., Ergintav, S., Georgiev, I., Gurkan, O., Hamburger, M., Hurst, K., Kahle, H., Kastens, K., Kekelidze, G., King, R., Kotzev, V., Lenk, O., Mahmoud, S., Mishin, A., Nadariya, M., Ouzounis, A., Paradissis, D., Peter, Y., Prilepin, M., Reilinger, R., Sanli, I., Seeger, H., Tealeb, A., Toksoz, M.N. & Veis, G., 2000. Global Positioning System constraints on plate kinematics and dynamics in the eastern Mediterranean and Caucasus, *J Geophys Res-Sol Ea*, 105, 5695-5719.
- Meyer, B., Tapponnier, P., Gaudemer, Y., Peltzer, G., Guo, S.M. & Chen, Z.T., 1996. Rate of left-lateral movement along the easternmost segment of the Altyn Tagh fault, east of 96 degrees E (China), *Geophys. J. Int.*, 124, 29-44.
- Molnar, P. & Tapponnier, P., 1975. Cenozoic Tectonics of Asia - Effects of a Continental Collision, *Science*, 189, 419-426.
- Moore, J.D.P. & Parsons, B., 2015. Scaling of viscous shear zones with depth-dependent viscosity and power-law stress-strain-rate dependence, *Geophys. J. Int.*, 202, 242-260.
- Mosegaard, K. & Tarantola, A., 1995. Monte-Carlo Sampling of Solutions to Inverse Problems, *J Geophys Res-Sol Ea*, 100, 12431-12447.
- Nishimura, T. & Thatcher, W., 2003. Rheology of the lithosphere inferred from postseismic uplift following the 1959 Hebgen Lake earthquake, *J. Geophys. Res.*, 108.
- Okada, Y., 1985. Surface deformation due to shear and tensile faults in a half-space, *Bull. Seismol. Soc. Am.*, 75, 1135-1154.
- Okada, Y., 1992. Internal Deformation Due to Shear and Tensile Faults in a Half-Space, *Bull. Seismol. Soc. Am.*, 82, 1018-1040.
- Owens, T.J. & Zandt, G., 1997. Implications of crustal property variations for models of Tibetan plateau evolution, *Nature*, 387, 37-43.
- Parsons, B., Wright, T., Rowe, P., Andrews, J., Jackson, J., Walker, R., Khatib, M., Talebian, M., Bergman, E. & Engdahl, E.R., 2006. The 1994 Sefidabeh (eastern Iran) earthquakes revisited: new evidence from satellite radar interferometry and carbonate dating about the growth of an active fold above a blind thrust fault, *Geophys. J. Int.*, 164, 202-217.
- Peltzer, G., Crampe, F. & King, G., 1999. Evidence of nonlinear elasticity of the crust from the Mw7.6 Manyi (Tibet) earthquake, *Science*, 286, 272-276.
- Peltzer, G., Rosen, P., Rogez, F. & Hudnut, K., 1996. Postseismic rebound in fault step-overs caused by pore fluid flow, *Science*, 273, 1202-1204.
- Peltzer, G., Rosen, P., Rogez, F. & Hudnut, K., 1998. Poroelastic rebound along the Landers 1992 earthquake surface rupture, *J Geophys Res-Sol Ea*, 103, 30131-30145.
- Pollitz, F.F., 1992. Postseismic Relaxation Theory on the Spherical Earth, *Bull. Seismol. Soc. Am.*, 82, 422-453.

- Pollitz, F.F., 1997. Gravitational viscoelastic postseismic relaxation on a layered spherical Earth, *J Geophys Res-Sol Ea*, 102, 17921-17941.
- Pollitz, F.F., 2005. Transient rheology of the upper mantle beneath central Alaska inferred from the crustal velocity field following the 2002 Denali earthquake, *J Geophys Res-Sol Ea*, 110.
- Pollitz, F.F., 2015. Postearthquake relaxation evidence for laterally variable viscoelastic structure and water content in the Southern California mantle, *J Geophys Res-Sol Ea*, 120, 2672-2696.
- Pollitz, F.F., Peltzer, G. & Burgmann, R., 2000. Mobility of continental mantle: Evidence from postseismic geodetic observations following the 1992 Landers earthquake, *J Geophys Res-Sol Ea*, 105, 8035-8054.
- Pollitz, F.F. & Thatcher, W., 2010. On the resolution of shallow mantle viscosity structure using postearthquake relaxation data: Application to the 1999 Hector Mine, California, earthquake, *J Geophys Res-Sol Ea*, 115.
- Pollitz, F.F., Wicks, C. & Thatcher, W., 2001. Mantle flow beneath a continental strike-slip fault: Postseismic deformation after the 1999 Hector Mine earthquake, *Science*, 293, 1814-1818.
- Qidong, D., Xiang, G. & Guihua, C., 2010. Recent tectonic activity of Bayankala fault-block and the Kunlun-Wenchuan earthquake series of the Tibetan Plateau, *Earth Sci. Front.*, 17, 163-178.
- Ramon, D., Cazier, L. & Santer, R., 2003. The surface pressure retrieval in the MERIS O-2 absorption: validation and potential improvements, *Igarss 2003: Ieee International Geoscience and Remote Sensing Symposium, Vols I - Vii, Proceedings*, 3126-3128.
- Reid, H., 1910. The California Earthquake of April 16 1906//Vol. 2. The Mechanics of the Earthquakes. The Carnegie InstWashington.
- Reilinger, R.E., Ergintav, S., Burgmann, R., McClusky, S., Lenk, O., Barka, A., Gurkan, O., Hearn, L., Feigl, K.L., Cakmak, R., Aktug, B., Ozener, H. & Toksoz, M.N., 2000. Coseismic and postseismic fault slip for the 17 August 1999, M=7.5, Izmit, Turkey earthquake, *Science*, 289, 1519-+.
- Ren, J.J., Xu, X.W., Yeats, R.S. & Zhang, S.M., 2013. Millennial slip rates of the Tazang fault, the eastern termination of Kunlun fault: Implications for strain partitioning in eastern Tibet, *Tectonophysics*, 608, 1180-1200.
- Replumaz, A. & Tapponnier, P., 2003. Reconstruction of the deformed collision zone between India and Asia by backward motion of lithospheric blocks, *J Geophys Res-Sol Ea*, 108.
- Rippe, D. & Unsworth, M., 2010. Quantifying crustal flow in Tibet with magnetotelluric data, *Phys. Earth Planet. Inter.*, 179, 107-121.
- Rosen, P., Gurrola, E., Sacco, G. & Zebker, H., 2011. InSAR Scientific Computing Environment-The Home Stretch. in *AGU Fall Meeting Abstracts*.
- Rosen, P.A., Hensley, S., Peltzer, G. & Simons, M., 2004. Updated repeat orbit interferometry package released, *Eos, Transactions American Geophysical Union*, 85, 47-47.
- Rosen, P.A., Hensley, S., Zebker, H.A., Webb, F.H. & Fielding, E.J., 1996. Surface

- deformation and coherence measurements of Kilauea volcano, Hawaii, from SIR-C radar interferometry, *J Geophys Res-Planet*, 101, 23109-23125.
- Royden, L., 1996. Coupling and decoupling of crust and mantle in convergent orogens: Implications for strain partitioning in the crust, *J Geophys Res-Sol Ea*, 101, 17679-17705.
- Royden, L.H., Burchfiel, B.C., King, R.W., Wang, E., Chen, Z.L., Shen, F. & Liu, Y.P., 1997. Surface deformation and lower crustal flow in eastern Tibet, *Science*, 276, 788-790.
- Rundle, J.B., 1981. Vertical displacements from a rectangular fault in layered elastic-gravitational media, *J. Phys. Earth*, 29, 173-186.
- Rundle, J.B., 1982. Viscoelastic-Gravitational Deformation by a Rectangular Thrust-Fault in a Layered Earth, *J. Geophys. Res.*, 87, 7787-7796.
- Ryder, I., Burgmann, R. & Pollitz, F., 2011. Lower crustal relaxation beneath the Tibetan Plateau and Qaidam Basin following the 2001 Kokoxili earthquake, *Geophys. J. Int.*, 187, 613-630.
- Ryder, I., Burgmann, R. & Sun, J., 2010. Tandem afterslip on connected fault planes following the 2008 Nima-Gaize (Tibet) earthquake, *J Geophys Res-Sol Ea*, 115.
- Ryder, I., Parsons, B., Wright, T.J. & Funning, G.J., 2007. Post-seismic motion following the 1997 Manyi (Tibet) earthquake: InSAR observations and modelling, *Geophys. J. Int.*, 169, 1009-1027.
- Ryder, I., Wang, H., Bie, L.D. & Rietbrock, A., 2014. Geodetic imaging of late postseismic lower crustal flow in Tibet, *Earth Planet. Sci. Lett.*, 404, 136-143.
- Sandwell, D., Mellors, R., Tong, X., Wei, M. & Wessel, P., 2011. Open radar interferometry software for mapping surface deformation, *Eos, Transactions American Geophysical Union*, 92, 234-234.
- Savage, J.C., 1998. Displacement field for an edge dislocation in a layered half-space, *J Geophys Res-Sol Ea*, 103, 2439-2446.
- Schmidt, D.A. & Bürgmann, R., 2003. Time - dependent land uplift and subsidence in the Santa Clara valley, California, from a large interferometric synthetic aperture radar data set, *J. Geophys. Res.*, 108.
- Scholz, C.H., 1998. Earthquakes and friction laws, *Nature*, 391, 37-42.
- Scholz, C.H., 2002. *The mechanics of earthquakes and faulting*, edn, Vol., pp. Pages, Cambridge university press.
- Shan, X.J., Qu, C.Y., Gong, W.Y., Zhao, D.Z., Zhang, Y.F., Zhang, G.H., Song, X.G., Liu, Y.H. & Zhang, G.F., 2017. Coseismic deformation field of the Jiuzhaigou M(s)7.0 earthquake from Sentinel-1A InSAR data and fault slip inversion, *Chinese J Geophys-Ch*, 60, 4527-4536.
- Shao, Z., Wang, R., Wu, Y. & Zhang, L., 2011. Rapid afterslip and short-term viscoelastic relaxation following the 2008 M W 7.9 Wenchuan earthquake, *Earthquake Science*, 24, 163-175.
- Shcherbakov, R., Turcotte, D.L. & Rundle, J.B., 2004. A generalized Omori's law

- for earthquake aftershock decay, *Geophys. Res. Lett.*, 31.
- Shen, F., Royden, L.H. & Burchfiel, B.C., 2001. Large-scale crustal deformation of the Tibetan Plateau, *J Geophys Res-Sol Ea*, 106, 6793-6816.
- Shen, W., Ritzwoller, M.H., Kang, D., Kim, Y., Lin, F.-C., Ning, J., Wang, W., Zheng, Y. & Zhou, L., 2016. A seismic reference model for the crust and uppermost mantle beneath China from surface wave dispersion, *Geophys. J. Int.*, 206, 954-979.
- Shen, Z., Wang, M. & He, P., 2017. Rheological Structure of Northern Tibet Lithosphere Inferred from Postseismic Deformation Modeling of 2001 Mw7.8 Kokoxili Earthquake. in *AGU Fall Meeting Abstracts*.
- Shen, Z.K., Jackson, D.D., Feng, Y.J., Cline, M., Kim, M., Fang, P. & Bock, Y., 1994. Postseismic Deformation Following the Landers Earthquake, California, 28 June 1992, *Bull. Seismol. Soc. Am.*, 84, 780-791.
- Shen, Z.K., Wan, Y.G., Gan, W.J., Zeng, Y.H. & Ren, Q., 2003. Viscoelastic triggering among large earthquakes along the East Kunlun fault system, *Chinese J Geophys-Ch*, 46, 786-795.
- Shi, X.H., Kirby, E., Furlong, K.P., Meng, K., Robinson, R. & Wang, E., 2015. Crustal strength in central Tibet determined from Holocene shoreline deflection around Siling Co, *Earth Planet. Sci. Lett.*, 423, 145-154.
- Simons, M., Fialko, Y. & Rivera, L., 2002. Coseismic deformation from the 1999 M-w 7.1 Hector Mine, California, earthquake as inferred from InSAR and GPS observations, *Bull. Seismol. Soc. Am.*, 92, 1390-1402.
- Simpson, R., Lienkaemper, J. & Galehouse, J., 2001. Variations in creep rate along the Hayward Fault, California, interpreted as changes in depth of creep, *Geophys. Res. Lett.*, 28, 2269-2272.
- Smith, S.W. & Wyss, M., 1968. Displacement on San Andreas Fault Subsequent to 1966 Parkfield Earthquake, *Bull. Seismol. Soc. Am.*, 58, 1955-&.
- Suito, H. & Freymueller, J.T., 2009. A viscoelastic and afterslip postseismic deformation model for the 1964 Alaska earthquake, *J. Geophys. Res.*, 114.
- Sun, J.B., Yue, H., Shen, Z.K., Fang, L.H., Zhan, Y. & Sun, X.Y., 2018. The 2017 Jiuzhaigou Earthquake: A Complicated Event Occurred in a Young Fault System, *Geophys. Res. Lett.*, 45, 2230-2240.
- Sylvester, A.G., 1988. Strike-Slip Faults, *Geol. Soc. Am. Bull.*, 100, 1666-1703.
- Tapponnier, P. & Molnar, P., 1976. Slip-Line Field-Theory and Large-Scale Continental Tectonics, *Nature*, 264, 319-324.
- Tapponnier, P., Peltzer, G., Le Dain, A., Armijo, R. & Cobbold, P., 1982. Propagating extrusion tectonics in Asia: New insights from simple experiments with plasticine, *Geology*, 10, 611-616.
- Tapponnier, P., Xu, Z.Q., Roger, F., Meyer, B., Arnaud, N., Wittlinger, G. & Yang, J.S., 2001. Geology - Oblique stepwise rise and growth of the Tibet plateau, *Science*, 294, 1671-1677.
- Taylor, M. & Yin, A., 2009. Active structures of the Himalayan-Tibetan orogen and their relationships to earthquake distribution, contemporary strain field, and Cenozoic volcanism, *Geosphere*, 5, 199-214.

- Thatcher, W., 2007. Microplate model for the present-day deformation of Tibet, *J Geophys Res-Sol Ea*, 112.
- Tse, S.T. & Rice, J.R., 1986. Crustal Earthquake Instability in Relation to the Depth Variation of Frictional Slip Properties, *J Geophys Res-Solid*, 91, 9452-9472.
- Unsworth, M., Wei, W.B., Jones, A.G., Li, S.H., Bedrosian, P., Booker, J., Sheng, J., Deng, M. & Tan, H.D., 2004. Crustal and upper mantle structure of northern Tibet imaged with magnetotelluric data, *J Geophys Res-Sol Ea*, 109.
- Wadge, G., Webley, P.W., James, I.N., Bingley, R., Dodson, A., Waugh, S., Veneboer, T., Puglisi, G., Mattia, M., Baker, D., Edwards, S.C., Edwards, S.J. & Clarke, P.J., 2002. Atmospheric models, GPS and InSAR measurements of the tropospheric water vapour field over Mount Etna, *Geophys. Res. Lett.*, 29.
- Walters, R.J., England, P.C. & Houseman, G.A., 2017. Constraints from GPS measurements on the dynamics of the zone of convergence between Arabia and Eurasia, *J Geophys Res-Sol Ea*, 122, 1470-1495.
- Wang, H., Xu, C.J. & Ge, L.L., 2007. Coseismic deformation and slip distribution of the 1997 M-w 7.5 Manyi, Tibet, earthquake from InSAR measurements, *J Geodyn*, 44, 200-212.
- Wang, R., Diao, F. & Hoechner, A., 2013a. SDM-A geodetic inversion code incorporating with layered crust structure and curved fault geometry. *in EGU General Assembly Conference Abstracts*.
- Wang, R.J., 1999. A simple orthonormalization method for stable and efficient computation of Green's functions, *Bull. Seismol. Soc. Am.*, 89, 733-741.
- Wang, R.J., Lorenzo-Martin, F. & Roth, F., 2006. PSGRN/PSCMP - a new code for calculating co- and post-seismic deformation, geoid and gravity changes based on the viscoelastic-gravitational dislocation theory, *Comput Geosci-Uk*, 32, 527-541.
- Wang, R.J., Martin, F.L. & Roth, F., 2003. Computation of deformation induced by earthquakes in a multi-layered elastic crust - FORTRAN programs EDGRN/EDCMP, *Comput Geosci-Uk*, 29, 195-207.
- Wang, R.J., Parolai, S., Ge, M.R., Jin, M.P., Walter, T.R. & Zschau, J., 2013b. The 2011 M-w 9.0 Tohoku Earthquake: Comparison of GPS and Strong-Motion Data, *Bull. Seismol. Soc. Am.*, 103, 1336-1347.
- Wei, W.B., Unsworth, M., Jones, A., Booker, J., Tan, H.D., Nelson, D., Chen, L.S., Li, S.H., Solon, K., Bedrosian, P., Jin, S., Deng, M., Ledo, J., Ray, D. & Roberts, B., 2001. Detection of widespread fluids in the Tibetan crust by magnetotelluric studies, *Science*, 292, 716-718.
- Wen, Y., Li, Z., Xu, C., Ryder, I. & Bürgmann, R., 2012. Postseismic motion after the 2001 Mw 7.8 Kokoxili earthquake in Tibet observed by InSAR time series, *J. Geophys. Res.*, 117.
- Wessel, P. & Smith, W.H., 1998. New, improved version of Generic Mapping Tools released, *Eos, Transactions American Geophysical Union*, 79, 579-579.
- Wimpenny, S., Copley, A. & Ingleby, T., 2017. Fault mechanics and post-seismic

- deformation at Bam, SE Iran, *Geophys. J. Int.*, 209, 1018-1035.
- Wright, T., Parsons, B. & Fielding, E., 2001. Measurement of interseismic strain accumulation across the North Anatolian Fault by satellite radar interferometry, *Geophys. Res. Lett.*, 28, 2117-2120.
- Wright, T.J., Elliott, J.R., Wang, H. & Ryder, I., 2013. Earthquake cycle deformation and the Moho: Implications for the rheology of continental lithosphere, *Tectonophysics*, 609, 504-523.
- Wright, T.J., Lu, Z. & Wicks, C., 2003. Source model for the M-w 6.7, 23 October 2002, Nenana Mountain Earthquake (Alaska) from InSAR, *Geophys. Res. Lett.*, 30.
- Wright, T.J., Parsons, B., England, P.C. & Fielding, E.J., 2004. InSAR observations of low slip rates on the major faults of western Tibet, *Science*, 305, 236-239.
- Xu, C., Fan, Q., Wang, Q., Yang, S. & Jiang, G., 2014. Postseismic deformation after 2008 wenchuan earthquake, *Surv Rev*, 46, 432-436.
- Xu, L.L., Rondenay, S. & van der Hilst, R.D., 2007. Structure of the crust beneath the southeastern Tibetan Plateau from teleseismic receiver functions, *Phys. Earth Planet. Inter.*, 165, 176-193.
- Xu, X., 2000. Scientific survey for the Manyi earthquake, *China Earthquake Yearbook, Seismological Press, Beijing*, 327-329.
- Xu, X.W., Chen, G.H., Wang, Q.X., Chen, L.C., Ren, Z.K., Xu, C., Wei, Z.Y., Lu, R.Q., Tan, X.B., Dong, S.P. & Shi, F., 2017. Discussion on seismogenic structure of Jiuzhaigou earthquake and its implication for current strain state in the southeastern Qinghai-Tibet Plateau, *Chinese J Geophys-Ch*, 60, 4018-4026.
- Xu, X.W., Wen, X.Z., Yu, G.H., Chen, G.H., Klinger, Y., Hubbard, J. & Shaw, J., 2009. Coseismic reverse- and oblique-slip surface faulting generated by the 2008 Mw 7.9 Wenchuan earthquake, China, *Geology*, 37, 515-518.
- Yamasaki, T. & Houseman, G.A., 2012. The crustal viscosity gradient measured from post-seismic deformation: A case study of the 1997 Manyi (Tibet) earthquake, *Earth Planet. Sci. Lett.*, 351, 105-114.
- Yamasaki, T., Wright, T.J. & Houseman, G.A., 2014. Weak ductile shear zone beneath a major strike-slip fault: Inferences from earthquake cycle model constrained by geodetic observations of the western North Anatolian Fault Zone, *J Geophys Res-Sol Ea*, 119, 3678-3699.
- Yin, A. & Harrison, T.M., 2000. Geologic evolution of the Himalayan-Tibetan orogen, *Annu Rev Earth Pl Sc*, 28, 211-280.
- Yu, C., Penna, N.T. & Li, Z.H., 2017. Generation of real-time mode high-resolution water vapor fields from GPS observations, *J Geophys Res-Atmos*, 122, 2008-2025.
- Zebker, H.A., Rosen, P.A. & Hensley, S., 1997. Atmospheric effects in interferometric synthetic aperture radar surface deformation and topographic maps, *J Geophys Res-Sol Ea*, 102, 7547-7563.
- Zebker, H.A. & Villasenor, J., 1992. Decorrelation in Interferometric Radar

- Echoes, *Ieee T Geosci Remote*, 30, 950-959.
- Zhang, C.J., Cao, J.L. & Shi, Y.L., 2009. Studying the viscosity of lower crust of Qinghai-Tibet Plateau according to post-seismic deformation, *Sci China Ser D*, 52, 411-419.
- Zhang, P.Z., Deng, Q.D., Zhang, G.M., Ma, J., Gan, W.J., Min, W., Mao, F.Y. & Wang, Q., 2003. Active tectonic blocks and strong earthquakes in the continent of China, *Sci China Ser D*, 46, 13-24.
- Zhang, P.Z., Molnar, P. & Xu, X.W., 2007. Late Quaternary and present-day rates of slip along the Altyn Tagh Fault, northern margin of the Tibetan Plateau, *Tectonics*, 26.
- Zhao, D.Z., Qu, C.Y., Shan, X.J., Zuo, R.H., Liu, Y.H., Gong, W.Y. & Zhang, G.H., 2018. Broadscale postseismic deformation and lower crustal relaxation in the central Bayankala Block (central Tibetan Plateau) observed using InSAR data, *J. Asian Earth Sci.*, 154, 26-41.
- Zhao, W., Mechie, J., Brown, L.D., Guo, J., Haines, S., Hearn, T., Klemperer, S.L., Ma, Y.S., Meissner, R., Nelson, K.D., Ni, J.F., Pananont, P., Rapine, R., Ross, A. & Saul, J., 2001. Crustal structure of central Tibet as derived from project INDEPTH wide-angle seismic data, *Geophys. J. Int.*, 145, 486-498.
- Zheng, W.J., Zhang, P.Z., He, W.G., Yuan, D.Y., Shao, Y.X., Zheng, D.W., Ge, W.P. & Min, W., 2013. Transformation of displacement between strike-slip and crustal shortening in the northern margin of the Tibetan Plateau: Evidence from decadal GPS measurements and late Quaternary slip rates on faults, *Tectonophysics*, 584, 267-280.
- Zheng, Y., Yang, Y., Ritzwoller, M.H., Zheng, X., Xiong, X. & Li, Z., 2010. Crustal structure of the northeastern Tibetan plateau, the Ordos block and the Sichuan basin from ambient noise tomography, *Earthquake Science*, 23, 465-476.
- Zhu, H. & Wen, X.Z., 2009. Stress triggering process of the 1973 to 1976 Songpan, Sichuan, sequence of strong earthquakes, *Chinese J Geophys-Ch*, 52, 994-1003.
- Zhu, L.P. & Rivera, L.A., 2002. A note on the dynamic and static displacements from a point source in multilayered media, *Geophys. J. Int.*, 148, 619-627.